

# 3D non-LTE abundance analyses of late-type stars

Karin Lind<sup>1</sup> and Anish M. Amarsi<sup>2</sup>

<sup>1</sup>Department of Astronomy, Stockholm University, AlbaNova Research Centre, SE-106 91, Stockholm, Sweden; email: karin.lind@astro.su.se

<sup>2</sup>Theoretical Astrophysics, Department of Physics and Astronomy, Uppsala University, Box 516, SE-751 20, Uppsala, Sweden; email: anish.amarsi@physics.uu.se

Annu. Rev. Astron. Astrophys 2024.  
AA:1–66

[https://doi.org/10.1146/\(\(please add article doi\)\)](https://doi.org/10.1146/((please add article doi)))

Copyright © 2024 by the author(s).  
All rights reserved

## Keywords

Atomic processes, Line: formation, Sun: abundances, Stars: abundances, Stars: atmospheres, Stars: late-type

## Abstract

The chemical compositions of stars encode the history of the universe and are thus fundamental for advancing our knowledge of astrophysics and cosmology. However, measurements of elemental abundances ratios, and our interpretations of them, strongly depend on the physical assumptions that dictate the generation of synthetic stellar spectra. Three-dimensional radiation-hydrodynamic (3D RHD) “box-in-a-star” simulations of stellar atmospheres offer a more realistic representation of surface convection occurring in late-type stars compared to traditional one-dimensional (1D) hydrostatic models. As evident from a multitude of observational tests, the coupling of 3D RHD models with line-formation in non-local thermodynamic equilibrium (non-LTE) today provides a solid foundation for abundance analysis for many elements. This review describes the ongoing and transformational work to advance the state-of-the-art and replace 1D LTE spectrum synthesis with its 3D non-LTE counterpart. In summary:

- 3D and non-LTE effects are intricately coupled and consistent modelling thereof is necessary for high-precision abundances, which is currently feasible for individual elements in large surveys. Mean 3D ( $\langle 3D \rangle$ ) models are not adequate as substitutes.
- The solar abundance debate is presently dominated by choices and systematic uncertainties that are not specific to 3D non-LTE modelling.
- 3D non-LTE abundance corrections have a profound impact on our understanding of FGK-type stars, exoplanets, and the nucleosynthetic origins of the elements.

## Contents

1. INTRODUCTION .....	2
2. THEORY AND METHODS .....	4
2.1. Model atmospheres .....	4
2.2. Model atoms .....	8
2.3. Spectrum synthesis .....	16
2.4. Astrophysical validation .....	21
2.5. 3D non-LTE effects on abundances .....	22
3. RESULTS .....	26
3.1. Solar modelling problem .....	26
3.2. Stellar parameters .....	33
3.3. Origin of the elements .....	37
3.4. Planet-host stars .....	46
4. DISCUSSION AND OUTLOOK .....	48
4.1. The transition from 1D LTE to 3D non-LTE .....	48
4.2. Future methodological developments .....	51
4.3. Concluding remarks .....	52

## 1. INTRODUCTION

In 1925, the ground-breaking work of Cecilia Payne-Gaposchkin revealed that stars are primarily composed of hydrogen and helium, with traces of heavier elements. Half a century later saw the dawn of quantitative spectroscopy using grids of model atmospheres for FGK-type dwarfs and giants of varying composition. Synthetic spectra based on one-dimensional (1D) hydrostatic models have become more extensive and sophisticated over time, by inclusion of a more accurate equation of state (EOS) and opacities, and monochromatic radiative transfer, and are still heavily used today. However, their applicability and physical realism are intrinsically limited by the unavoidably simplified treatment of convection, as well as by the commonly-employed assumption of local thermodynamic equilibrium (LTE).

A fundamental improvement to the modelling of spectra of FGK-type stars was introduced by lifting the assumption that all atomic level populations abide strictly to LTE. Pioneering 1D non-LTE studies targetted spectral lines of e.g., Li, O, and Fe (Athay & Lites 1972, Steenbock & Holweger 1984, Kiselman 1991). Equipped with model atoms with approximately a dozen energy levels, the statistical equilibrium equations could be solved with the computational power available at the time, and sometimes yielded significant deviations from LTE. Importantly, spectral lines were found to react differently to non-LTE modelling depending on atomic properties, abundance, and atmospheric conditions, a conclusion that has been reinforced many times since. Because the necessary atomic data were often lacking, astrophysical calibration of model atoms to minimize abundance discrepancies between lines was common and the custom still prevails, but to a much lesser extent today.

This century has seen a dramatic improvement in the availability and quality of atomic and molecular data for neutrals and singly ionized species, such as energy levels, transition rates or oscillator strengths, photoionisation cross-sections and collisional cross-sections. In particular, the development of ab initio quantum chemistry calculations and asymptotic model approximations of inelastic hydrogen collisions has removed a crucial free parameter

in the modelling of late-type stars (Barklem 2016a). Such data now exist for more than twenty metals of astrophysical importance.

Largely in parallel with the development of 1D non-LTE abundance analysis, three-dimensional radiation-hydrodynamic (RHD) simulations of stellar surface convection were introduced, allowing us to predict the inhomogeneous and dynamic state of the atmosphere from first principles (Nordlund 1982, Nordlund & Dravins 1990, Nordlund & Stein 1990, Stein & Nordlund 1998). Observational validation of such models have revealed, for example, that they can adequately reproduce spectral line asymmetries and blueshifts, the statistical properties of granulation, and the observed centre-to-limb (CLV) variation of solar continuum light (e.g. Dravins et al. 1981, Asplund et al. 2000a, Wedemeyer-Böhm & Rouppe van der Voort 2009, Uitenbroek & Criscuoli 2011, Pereira et al. 2013).

Despite the many successes of 3D RHD models, it soon became apparent that their use for abundance analyses must proceed with great care. The temperature and density fluctuations associated with granulation can lead to significant strengthening of lines under LTE, but the steeper temperature stratification of metal-poor stars also often lead to enhanced non-LTE effects in the opposite direction (Asplund 2005). At the turn of the century, 3D non-LTE modelling that simultaneously accounted for departures from LTE and homogeneity was still in its infancy, with trailblazing studies for a handful of stars using simple atoms for elements with great astrophysical significance (Kiselman & Nordlund 1995, Asplund et al. 2003, Barklem et al. 2003, Shchukina et al. 2005, Cayrel et al. 2007). In contrast, leading 3D non-LTE studies are now performed with model atoms including hundreds of energy levels (Amarsi et al. 2016b, Nordlander et al. 2017, Lind et al. 2017, Bergemann et al. 2019), and for tens or hundreds of model atmospheres (e.g. Amarsi et al. 2022). This progress owes much to the exponential growth in computational power and the development of frequency- and domain-decomposed MPI-parallelised codes that solve the restricted non-LTE problem in 3D (Leenaarts & Carlsson 2009, Amarsi et al. 2018b).

Alongside advances on the theory and modelling side, spectroscopic stellar surveys have become a cornerstone of modern astrophysics, now routinely collecting medium and high-resolution data for hundreds of thousands of stars (Jofré et al. 2019). Accurate determination of chemical abundances and fundamental stellar parameters such as effective temperature, surface gravity, mass and age, is a primary goal of current and upcoming surveys and instrumental to the diverse endeavours of Galactic archaeology. Recently, the GALAH survey presented the largest existing 1D non-LTE abundance data set for 13 elements in 650,000 stars (Amarsi et al. 2020b, Buder et al. 2021), removing any lingering doubt of the feasibility of such analysis for million-star spectroscopic surveys. In fact, 3D non-LTE analysis is also possible for individual elements, such as Li (Wang et al. 2024) and O (Amarsi 2016), but, as discussed here, more work is needed on the grids of 3D RHD simulations, grids of 3D non-LTE calculations, and spectrum interpolation techniques, before 3D analysis will be truly competitive with 1D analysis in this respect.

In this review, we describe the methodology behind 3D non-LTE spectral line formation, its observational validation and practical implementation in spectroscopic analyses, and the impact seen for the Sun and other stars. We review the abundances of elements for which high-quality model atoms can be constructed and include a description of common data sources. We compare 3D non-LTE abundances with 1D LTE, 1D non-LTE and 3D LTE ones and discuss the usefulness of alternative approaches, such as horizontally- and temporally-averaged 3D models, so called <3D> models.

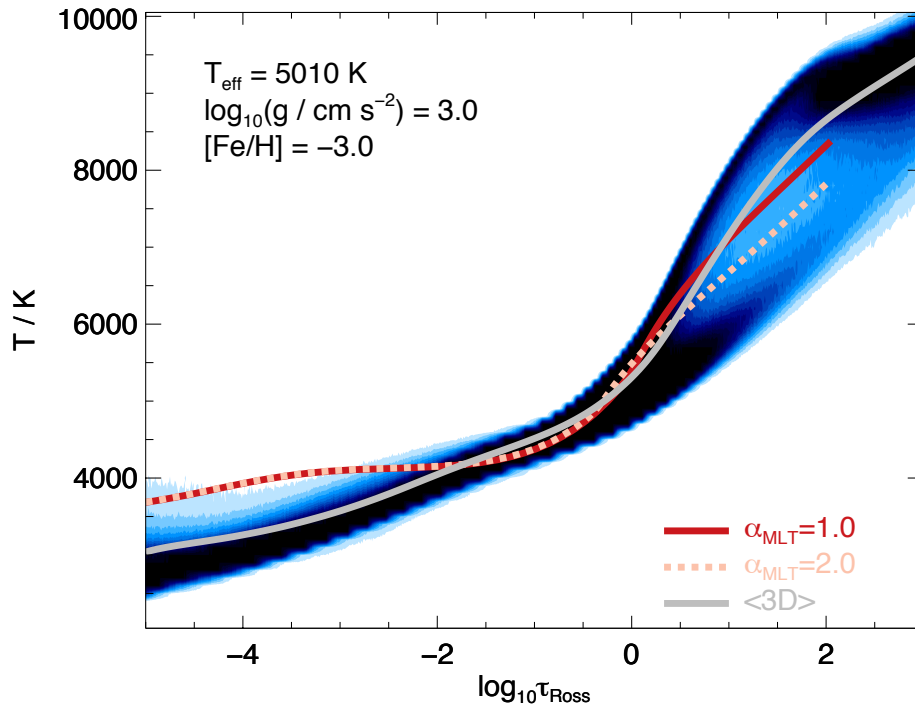


**Figure 1:** Distribution of gas temperature with logarithmic vertical optical depth in a 3D RHD model atmosphere from the *Stagger*-grid. Also shown are theoretical 1D models computed with different mixing lengths, and a <3D> model. From [Amarsi et al. \(2018b\)](#).

## 2. THEORY AND METHODS

In this section we summarise the theory and methods relevant to deriving 3D non-LTE abundances in late-type stars. Sect. 2.1 gives an overview of the construction of three-dimensional RHDs model atmospheres, and Sect. 2.2 describes the construction of model atoms, as well as how their complexities are reduced. Sect. 2.3 outlines the generation of 3D non-LTE stellar spectra given these key inputs. This section closes with a synopsis of the validation of the 3D model atmospheres and the 3D non-LTE stellar spectra, in Sect. 2.4.

### 2.1. Model atmospheres

The first key input to 3D non-LTE spectrum synthesis codes is the model atmosphere. In the context of “3D non-LTE abundance analyses of late-type stars”, we usually refer to 3D RHD “box-in-a-star” large-eddy simulations of stellar surface convection. In general, simulations including magnetic fields (3D radiation magnetohydrodynamics; 3D RMHD) are beyond the scope of this paper, although some results are briefly discussed in Sect. 2.5.4. The 3D RHD simulations aim to provide a realistic ab initio description of the continuum- and line-forming regions of the stellar photosphere via a fundamental treatment of the mass, momentum, and energy transfer due to convection, combined with a non-grey treatment of

radiative transfer. In contrast, 1D models must employ some simplified picture of turbulent convection that involves adjustable parameters, such as the Mixing Length Theory (Heneyey et al. 1965, Gough 1977, Balmforth & Gough 1990). Although one can attempt to calibrate mixing length parameters to reproduce the mean structures of the deeper layers of 3D RHD models (e.g. Trampedach et al. 2014, Sonoi et al. 2019), it fails to properly describe the temperature stratification close to the optical surface and in the convectively-stable line-forming regions above it (Fig. 1); and there can be particularly large discrepancies for metal-poor stars (Collet et al. 2007). The 1D hydrostatic models also cannot make predictions related to stellar granulation that cause line shifts, asymmetries, and broadening (e.g. Dravins et al. 2021), that can also act to desaturate and strengthen strong lines.

We also note that 3D RHD models should not be confused with horizontally- and temporally-averaged 3D RHD models, hereafter <3D> models. These <3D> models are sometimes referred to in the literature as 3D models, but this should be avoided. Such models suffer from several disadvantages that theoretical 1D hydrostatic models are also prone to, due to the anisotropy of convective motions and the non-linearity of spectral line formation in stellar atmospheres (Uitenbroek & Criscuoli 2011).

**2.1.1. Codes and grids.** Most 3D non-LTE abundance analyses for stars other than the Sun have employed simulations based on the parallelised 3D R(M)HD codes **Stagger** (Nordlund & Galsgaard 1995, Collet et al. 2018, Stein et al. 2024) and **C0<sup>5</sup>BOLD** (Wedemeyer et al. 2004, Freytag et al. 2012, Ludwig & Kučinskas 2012). Other codes that are commonly used for realistic simulations of stellar surface convection include for example **MURaM** (Vögler et al. 2005) and **Antares** (Muthsam et al. 2010); further examples can be found within the review of Kupka & Muthsam (2017). Reassuringly, comparisons of solar models with independent codes tend to show rather small differences in granulation and mean structure (Kupka 2009, Beeck et al. 2012, Cubas Armas & Fabbian 2021). These are likely to be negligible in the context of solar abundance determinations. For instance, the comparisons of Si I lines based on **Stagger** and **C0<sup>5</sup>BOLD** models (albeit also using different 3D LTE spectrum synthesis codes) presented in Appendix A of Deshmukh et al. (2022) suggests differences of at most 0.01 dex in abundance. Similarly, only small differences are found in 3D LTE for lines of C I (Sect. 4.2 of Amarsi et al. 2019a) and N I (Fig. 5 of Amarsi et al. 2020a).

The reason for the dominance of **Stagger** and **C0<sup>5</sup>BOLD** in this context is in part due to them being used to construct grids of 3D RHD models; namely, the **Stagger**-grid (Magic et al. 2013a, Rodríguez Díaz et al. 2022, 2023) and the **CIFIST**-grid (Ludwig et al. 2009b, Ludwig & Kučinskas 2012, Bertran de Lis et al. 2022). These grids span a wide enough range of three fundamental stellar parameters to be useful for abundance analyses: effective temperature  $T_{\text{eff}}$ , surface gravity  $\log g$ , and Fe abundance  $[\text{Fe}/\text{H}]$ , which serves as a proxy for the overall stellar metallicity  $Z$ . Other grids of models exist (e.g. Tanner et al. 2013b,a, Trampedach et al. 2013), but are more limited in stellar parameter space. We illustrate the coverage of the **Stagger**-grid and **CIFIST**-grid in Fig. 2. By comparing to MIST model isochrones (Dotter 2016), we see that the grids have good coverage of the main sequence and subgiants with  $4500 < T_{\text{eff}} < 6500$  K, but would benefit from a more complete coverage of the metal-poor red giant branch. It may be important to introduce more parameters into these grids to properly model stars with peculiar abundances and recently a version of **Stagger** was developed to help facilitate this (Zhou et al. 2023). Selected snapshots of the original **Stagger**-grid models, reprocessed and tailored for abundance analyses, will soon be publicly available (Rodríguez Díaz et al. 2023).

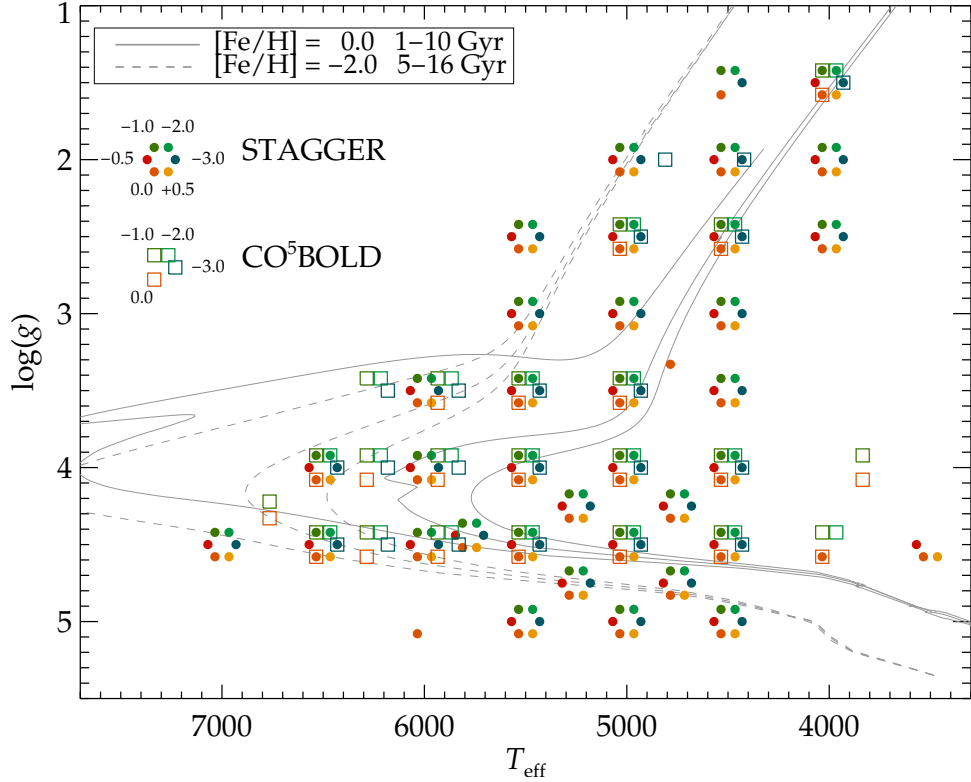


**Figure 2:** Extent of the *Stagger*-grid and *CIFIST*-grid of 3D RHD model atmospheres, in  $T_{\text{eff}}$ ,  $\log g$ , and  $[\text{Fe}/\text{H}]$ . Grid data are shown for 214 *Stagger* models from Rodríguez Díaz et al. (2023) and 84 *CO<sup>5</sup>BOLD* models from the *CIFIST*-grid used by Bertran de Lis et al. (2022). The values of  $T_{\text{eff}}$  are centered on grid nodes for clarity and representative to within  $\pm 100$  K of the true model. Metal-poor and solar-metallicity MIST isochrones are included for comparison, with ages as indicated by the legend. The  $[\text{Fe}/\text{H}] = -4$  models of the *Stagger*-grid have been omitted from the figure (see Rodríguez Díaz et al. (2023)).

**2.1.2. Overview of the simulation approach.** We refer the reader to other literature (e.g. Stein & Nordlund 1998, Freytag et al. 2012, Kupka & Muthsam 2017, Collet et al. 2018) for a full discussion of performing the 3D RHD simulations; here we give just a brief overview with emphasis on details pertinent to 3D non-LTE abundance analyses. Fundamentally, the simulations solve the coupled time-dependent equations describing the conservation of mass, momentum, and energy. The simulations in the *Stagger*-grid and *CIFIST*-grid are of similar extent and resolution. In the case of the former, they adopt a Cartesian mesh with  $240^3$  grid points that includes 10 vertical ghost zones distributed at the lower and upper boundaries, with finest resolution around the continuum forming regions. They span a vertical extent from  $-5.0 < \log \tau_{\text{Ross.}} < +6.0$  or around 14 pressure scale heights, thus capturing the outer part of the convective envelope as well as the photosphere. They exclude the chromosphere, which is assumed to not significantly impact the structure of the continuum- and line-forming regions of the photosphere. They cover a relatively small

area of the stellar disc, enclosing at least 10 granules at any time of the simulation; for the Sun this corresponds to around 0.004% of the total disc area (Rodríguez Díaz et al. 2022). Given the limited volume of the simulation box, the curvature of the stars can be neglected. Moreover a constant acceleration due to external forces is assumed throughout the box that corresponds to the  $\log g$  of the model, and centrifugal and Coriolis forces are neglected (the models are non-rotating). The horizontal boundaries are periodic and the vertical boundaries are open. The entropy and thermal pressure of the inflowing gas at the bottom boundary are assumed to be constant. The time-averaged  $T_{\text{eff}}$  of the simulation is a function of this entropy combined with the other parameters of the simulation, and this is why the nodes of the **Stagger**-grid and **CIFIST**-grid are slightly irregular in  $T_{\text{eff}}$ . Since the granulation as well as the  $T_{\text{eff}}$  of the simulations, calculated via integration of the emergent flux, fluctuate with time, it is necessary to carry out spectrum synthesis calculations on several snapshots; consequently the **Stagger**-grid models span around two convective turnover times, corresponding to several periods of the fundamental p-mode of the simulation domain.

The influence of radiation enters mainly through the energy equation, where it is necessary for describing the radiative heating and cooling rates. The radiative transfer equation is solved in the layers close to and above the optical surface at each time step of the simulation, for a small number of opacity bins (Sect. 2.1.3). **Stagger** uses a modified version of the long characteristics method of Feautrier (1964) as described in Stein & Nordlund (2003), and integrates the intensity for nine rays, or eighteen directions on the unit sphere. The latest version of **CO<sup>5</sup>BOLD** has a short characteristics solver that may give better overall time performance (Steffen 2017). Radiation also enters as pressure in the momentum equation, but it is generally negligible for the stars of interest here; in the **Stagger**-grid it is estimated in an approximate way by assuming it to be isotropic and carrying out radiative transfer calculations on <3D> models.

**2.1.3. Microphysics.** The EOS relates state variables and gives the distribution of nuclei in atomic, ionic, and molecular states. These are used to calculate opacities under the assumption of LTE (via the Boltzmann distribution; e.g. Hirose et al. 2022). The code **CO<sup>5</sup>BOLD** calculates this using the Saha equation and the analogous equation for molecular equilibrium, whereas **Stagger** adopts the free energy minimisation approach of Mihalas et al. (1988), often referred to as the MHD EOS, as implemented by Trampedach et al. (2013). In the latter, the 17 most abundant elements as well as the  $\text{H}_2$  and  $\text{H}_2^+$  molecules are considered, and the occupation probability formalism is used to account for the dissolution of Rydberg levels into the continuum (Hummer & Mihalas 1988). Recently **FreeEOS** (Irwin 2012), also based on free energy minimisation, was implemented into **Stagger**: Zhou et al. (2023) show, at least in the context of stellar spectroscopy, that this change in EOS leads to negligible differences on the solar simulations, at least when the elemental abundance ratios are kept fixed. This is consistent with the findings of Vitas & Khomenko (2015). In all cases, partition functions as well as ionisation energies and molecular equilibrium constants for the species of interests (e.g. Barklem & Collet 2016) are needed (in late-type stellar atmospheres it is usually sufficient to consider up to doubly-ionised species), and instantaneous chemical equilibrium is assumed.

The larger uncertainty comes from the treatment of opacities. This is a key aspect of 3D RHD simulations, as radiation has a strong influence on the mean temperature stratification of the model via the heating and cooling rates. A full monochromatic solution

of the radiative transfer equation at every time step is computationally prohibitive, even in LTE. Consequently, 3D RHD models typically solve the radiative transfer for a small number of representative opacity bins (Nordlund 1982, Skartlien 2000). In the **Stagger**-grid, 12 such bins are used. A careful selection of opacity bins is crucial to obtain the correct temperature structure in the optically thin layers. Collet et al. (2018) performed simulations for the metal-poor (adopted  $[\text{Fe}/\text{H}] = -2.5$ ) red giant HD 122563 with varying number of bins, and demonstrated that the 12-bin solution is in good agreement with the 48-bin one, provided that the opacity bins are constructed to take into account both strength and frequency (see their Fig. 1 and Fig. 9). At higher metallicities, the simulations are expected to be less sensitive to the detailed treatment of the radiation field. Still, future studies might consider improving the opacity binning scheme, for example by exploring the use of clustering algorithms.

The source function is usually assumed to be Planckian as per LTE. However, it should be noted that the **Stagger**-grid models estimate the continuum scattering contribution to the extinction (Sect. 2.3.5) and exclude it from the integrand in the optically thin layers. This is necessary to avoid errors of up to around 500 K in the upper layers of metal-poor stars (Collet et al. 2011). The most recent models in the **CIFIST**-grid adopt a similar approach.

**2.1.4. Cost.** The computational cost of 3D RHD models is determined by various timescales that are discussed in detail in for example Ludwig et al. (2002), Freytag et al. (2012), and Kupka & Muthsam (2017). For stars similar to the Sun, with a suitable choice of initial conditions such that the mean structure is already well described in the deeper layers, relaxation should occur after some number of convective turnover times,  $\tau_{\text{conv.}} \sim H_{\text{p}}/v_{\text{conv.}}$ , where  $H_{\text{p}} \propto T_{\text{eff}}/g$  is the pressure scale height and  $v_{\text{conv.}}$  is the convective velocity; here we assume the latter to scale as the sound speed  $c_{\text{s}} \propto \sqrt{T_{\text{eff}}}$ . It is relevant to consider this time scale relative to the time step  $\Delta t$  of the simulations, which is usually dictated by the minimum radiative timescale near the optical surface  $\tau_{\text{rad.}} \sim T_{\text{eff}}^{-3}$ . The ratio  $\tau_{\text{conv.}}/\tau_{\text{rad.}}$  then scales as  $T_{\text{eff}}^{3.5} g^{-1}$ . A typical red giant with  $T_{\text{eff}} = 4500$  K and  $\log g = 1.5$  K gives a cost around 400 times more than that for the Sun, demonstrating how such models are often the most expensive to compute within the existing grids. If a solar model takes of the order 300 CPU hours to run (Freytag et al. 2012), a red giant model takes 0.1 MCPU hours. However, these estimates do not include the often time consuming steps to optimize the opacity bin limits, damp oscillations, and arrive at the target  $T_{\text{eff}}$  by adjusting the bottom boundary condition (Rodríguez Díaz et al. 2023); these can take significant time and may even dominate the overall costs.

## 2.2. Model atoms

The second key input to 3D non-LTE spectrum synthesis codes is the so-called “model atom”. This represents all of the additional atomic (and ionic and molecular) data needed to relax the assumption of LTE, via solving for the statistical equilibrium (Sect. 2.3.3), sometimes referred to as collisional-radiative modelling: a) the energies ( $E_i$ ) and statistical weights ( $g_i = 2J_i + 1$ ) of the atomic, ionic, and also (less commonly) molecular levels; b) the Einstein coefficients or oscillator strengths for the bound-bound radiative transitions, and the cross-sections for the bound-free radiative transitions; and c) the cross-sections or rate coefficients for the most important inelastic collisional processes, which, in late-type



stars, are typically involving either electrons or neutral hydrogen atoms.

Our focus below is on the construction of tractable yet reliable model atoms for 3D non-LTE abundance analyses. A full description of the methods for how to go about accurately measuring or calculating the data themselves is beyond the scope of this paper, and we recommend the review of [Barklem \(2016a\)](#) as a starting point for more insight into this. Moreover, we focus on neutral and singly-ionised atomic species, which have been the main interest of the vast majority of non-LTE studies for late-type stars to date, although we briefly discuss molecules later in Sect. 2.5.2. In this context, excellent resources are the National Institute of Standards and Technology Atomic Spectra Database (NIST ASD; [Ralchenko & Kramida 2020](#)), the databases of the Opacity Project (TOPbase; [Cunto et al. 1993](#)) and the Iron Project (TIPbase; [Nahar & Pradhan 2005](#)), the Kurucz Smithsonian Atomic and Molecular Database (Kurucz database; [Kurucz 2017](#)), and VALD (formerly the Vienna Atomic Line Database; [Ryabchikova et al. 2015](#)). Relevant and useful data can also be found in the Nahar OSU Radiative database (NORAD-Atomic-Data; [Nahar 2020](#)) the CHIANTI atomic database (CHIANTI; [Dere et al. 2023](#)), and the Atomic Data and Analysis Structure database (OPEN-ADAS; [Summers & O’Mullane 2011](#)). These and other databases can also be accessed via the Virtual Atomic and Molecular Data Centre (VAMDC; [Albert et al. 2020](#)). The databases mostly contain information on energies and radiative transitions, although some also include inelastic electron collision data. However, they do not include results for inelastic collisions with hydrogen atoms. Such processes are crucially important in non-LTE studies of late-type stars, as we discuss below (Sect. 2.2.3).

**2.2.1. Levels.** The energy levels establish the infrastructure for the rest of the model atom. For species other than hydrogen (see [Kramida 2010](#)), the accuracy of experimental measurements of energies, via spectroscopic measurements of wavelengths and term analyses (e.g. [Nave et al. 1994](#)), almost always far exceeds that of theoretical calculations. As such, the usual starting point for energies is NIST ASD, which contains a critical compilation of experimental energy levels. Often these data are not sufficiently complete for non-LTE modelling, especially for heavier elements. Model atoms must then make use of theoretical data. For instance, for Fe I [Lind et al. \(2017\)](#) use the Kurucz database, which complements experimental data with semi-empirical predictions; in this case predicted fine-structure levels outnumber the experimental ones by a factor of three, as can be gauged from Fig. 3.

Model atoms usually must have a complete description of the levels of the species under investigation (neutral or singly-ionised), as well as the ground level(s) of the neighbouring ionisation stages. Elements with intermediate excitation potentials may require a comprehensive description of both the neutral and singly-ionised species, as they have comparable populations in late-type stellar atmospheres. A natural maximum for the number of excited levels to include comes from considering the dissolution of Rydberg levels due to perturbations by charged particles. Where this becomes significant can be roughly estimated from Eq. 8.86 of [Hubeny & Mihalas \(2015\)](#) for the reduction in binding energy, which gives around 0.01 eV in the deepest layers of the atmospheres of warm late-type stars, and smaller values in the line-forming regions. In reality, the levels this close to the ionisation threshold have small Boltzmann factors and are not significantly populated in late-type stars, and thus are often omitted. Usually, for the neutral species for example, only levels up to some tenths of an electron volt from the ionisation threshold are included explicitly. This is sufficient to allow for collisional coupling to the next ionisation stage ([Mashonkina et al. 2011](#); cf. the mean electron kinetic energy  $E = \frac{3}{2}k_B T = 0.75$  eV for solar photospheric conditions).

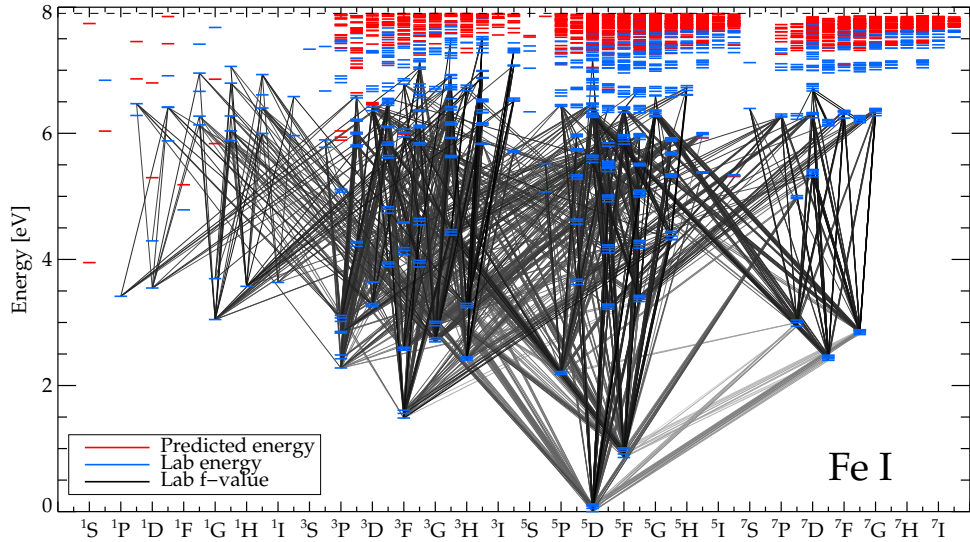


**Figure 3:** Grotrian diagram illustrating part of a model atom of Fe I. The energy levels are taken from the Kurucz database and include experimentally confirmed (blue) and predicted levels (red). Only transitions with experimentally measured transition probabilities are shown. Data sources are listed in Lind et al. (2017).

**2.2.2. Radiative transitions.** The radiative rates  $R_{ij}$  appearing in the equations of statistical equilibrium (Sect. 2.3.3) depend on the Einstein coefficients or oscillator strengths for the bound-bound radiative transitions, and the cross-sections for the bound-free radiative transitions, together with the radiation field. NIST ASD contains a critical compilation of experimental and theoretical data, including accuracy rating of transition probabilities, and is again the usual starting point in the current context. The VALD repository can also be very useful, containing a wealth of experimental and theoretical data compiled from the literature. It can be worth scanning literature directly for the latest results from the various groups measuring precise data (e.g. Belmonte et al. 2021, Geng et al. 2022, Burheim et al. 2023, Clear et al. 2023, Den Hartog et al. 2023, Zhou & Shang 2023), and groups calculating extended data of sufficient overall accuracy for stellar spectroscopy (e.g. Li et al. 2023a,b) based on for example Multi-Configuration Dirac-Hartree-Fock (MCDHF) methods (e.g. Froese Fischer et al. 2019). To complete the model atom, such data must often be complemented with the results of semi-empirical or fully theoretical calculations, for example from the Kurucz database, or from TOPbase, TIPbase, and NORAD-Atomic-Data that employ the  $R$ -matrix method (Burke 2011), as well as data compiled within CHIANTI. Fig. 3 shows the subset of radiative transitions in Fe I that have experimentally measured oscillator strengths, which in this case is only 0.5% of the more than half a million fine-structure transitions with semi-empirical values from the Kurucz database.

Theoretical line data, for example from TOPbase, are often calculated without fine structure. The Einstein coefficients or oscillator strengths can be redistributed over fine structure levels under the assumption of LS-coupling (see for example Sect. 10.16.6 of Martin & Wiese 2006). Even if the fine structure levels are merged in order to reduce the complexity of the model atom as we describe in Sect. 2.2.4, it may be important to consider this splitting

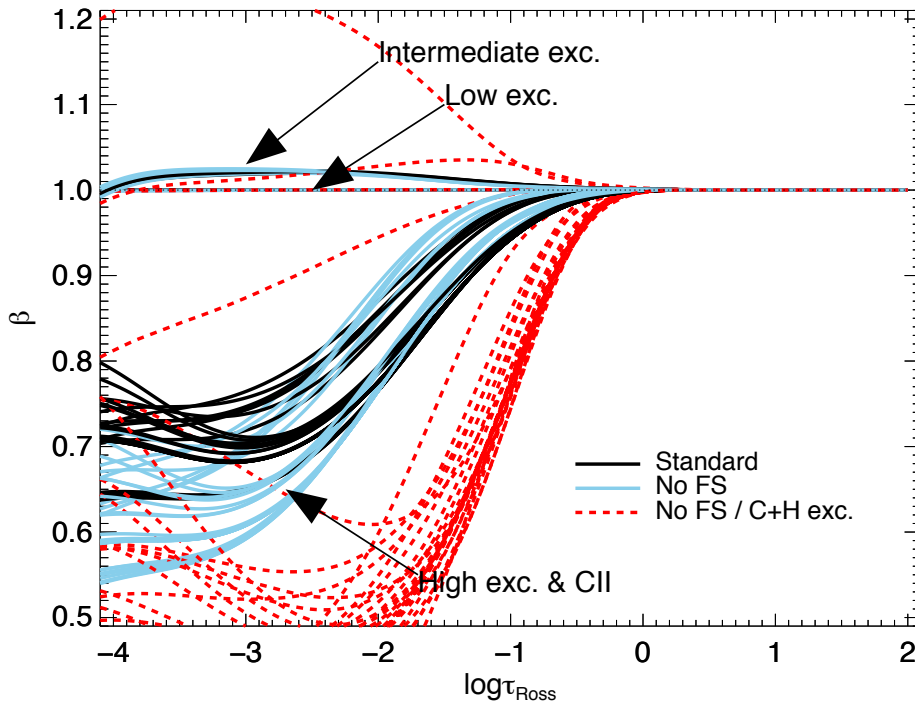


**Figure 4:** Departure coefficients for levels of neutral C as well as the ground level of singly-ionised C in a <3D> model of the solar atmosphere, with levels labelled by excitation energy. Results are shown for a model atom where most fine structure is resolved (“Standard”), where fine structure is merged (“No FS”), and where, in addition, excitation by hydrogen collisions is omitted (“No FS / C+H exc.”). From [Amarsi et al. \(2019a\)](#).

in the calculation of the bound-bound opacity profiles. This is especially the case when the multiplet components are unsaturated, but resolvable and separated. In this situation, neglecting fine structure then leads to a line that is significantly too strong, corresponding to an angle-averaged intensity  $J_\nu$  that is too small (see Appendix B of [Steffen et al. 2015](#)). This could, for example, lead to larger departures from LTE for some species due to enhanced photon losses (Fig. 4).

For photoionisation cross-sections, it is often necessary to use the results of theoretical calculations. For lighter elements these are usually drawn from TOPbase or NORAD-Atomic-Data. Other data also employing the  $R$ -matrix method can be found in the literature (e.g. [Bautista et al. 2017](#), [Smyth et al. 2019](#)). There are now also results for a number of important species based on the  $B$ -spline  $R$ -matrix method (BSR; e.g. [Zatsarinny & Bartschat 2013](#), [Zatsarinny et al. 2019](#)). Typically, for excited levels of heavier elements, it is necessary to resort to hydrogenic approximations (e.g. [Mashonkina et al. 2012](#)); however, the error in this approximation can be large enough to lead to, for example, predict absorption instead of emission for Si II lines in hot stars ([Mashonkina et al. 2022](#)). As mentioned above, the energies in these theoretical calculations are typically not of sufficient accuracy

for stellar spectroscopy, and for large deviations the cross-sections should be shifted so that the predicted thresholds match the experimental ones. Sharp autoionisation resonances in the data, while potentially important to the non-LTE solution, are similarly offset from their true frequencies, and also do not include for example thermal broadening. Thus it is justified to apply some Gaussian smoothing to the data (e.g. [Bautista et al. 1998](#), [Allende Prieto et al. 2003](#), [Lanz & Hubeny 2003](#)). This also aids in putting all of the photoionisation cross-sections onto a common frequency grid, which helps reduce the computational cost of the post-processing calculations (e.g. [Bard & Carlsson 2008](#)).

**2.2.3. Collisional transitions.** The collisional rates  $C_{ij}$  appearing in the equations of statistical equilibrium (Sect. [2.3.3](#)) depend on both the number density of perturbers, and the collisional rate coefficients (which is the Maxwellian-averaged collisional cross-section:  $\langle\sigma v\rangle$ ). Electrons are important perturbers in late-type stars because of their low masses and thus large mean thermal velocities, and also because, as per the Massey criterion ([Massey 1949](#)), the collisions for optical transitions should be close to resonance ([Barklem 2016a](#)). As discussed in [Lambert \(1993\)](#) and [Barklem et al. \(2011\)](#), hydrogen collisions were initially estimated to be of lesser importance, noting that hydrogen atoms move more slowly by a factor of  $\sqrt{m_{e^-}/m_H} \sim 10^{-2}$ , and that the transitions corresponding to optical wavelengths are in the adiabatic regime and so should have much smaller cross-sections per the Massey criterion. However, this is offset by the large abundance of hydrogen atoms:  $n_H/n_{e^-} \sim 10^4$  in the upper layers of the solar photosphere, with even larger ratios in cooler and more metal-poor stars ([Steenbock & Holweger 1984](#)). Moreover, hydrogen collisions move closer to resonance towards smaller wavelengths ([Lambert 1993](#)) and for this reason one expects levels with very small energy differences, for example Rydberg levels and fine structure levels, to be close to relative LTE in late-type stellar atmospheres (collision data are now available to test this in some cases; e.g. [Yan & Babb 2023](#)). In all, in light of quantum mechanical data for the collision cross-sections (discussed below), the current consensus is that (de-)excitation and ionisation or recombination by electron collisions, and (de-)excitation and charge transfer or mutual neutralisation by hydrogen collisions, are of critical importance for non-LTE studies of late-type stars.

For electron collisions, data for (de-)excitation ( $X_i + e^- \leftrightarrow X_j + e^-$ ) and ionisation or recombination ( $X_i + e^- \leftrightarrow X_j^+ + 2e^-$ ) based on  $R$ -matrix calculations can be found via TIPbase, NORAD-Atomic-Data, CHIANTI, and Open-ADAS for many species of interest. Data based on more advanced methods are also available for some species, for example employing the BSR method mentioned above ([Tayal & Zatsarinny 2022](#)) or the Convergent Close Coupling method (CCC; e.g. [Bray & Stelbovics 1992](#), [van Eck et al. 2020](#)). It is reassuring that BSR and CCC collision data have been demonstrated to agree to a remarkably high level ([Barklem et al. 2017](#), [Dipti et al. 2019](#), [Reggiani et al. 2019](#)). In general, however, data from  $R$ -matrix and more advanced calculations do not extend to Rydberg levels, and neutral species of heavier elements are less well represented overall. As such, it is necessary to also employ more approximate methods. For excitation, the most common recipes are the semi-empirical [van Regemorter \(1962\)](#) recipe and the semi-classical impact parameter method as formulated by [Seaton \(1962b\)](#). Their accuracies depend on the species and transitions in question; for K I, the former has errors of around a factor of ten, with larger errors for transitions corresponding to longer wavelengths (Fig. 2 of [Reggiani et al. 2019](#)). The latter approach is expected to be more reliable overall, particularly for transitions between Rydberg levels ([Barklem 2016a](#)), as also suggested by recent modelling of the Mg I infrared

emission lines that are highly sensitive to the collisional data (Osorio et al. 2015, Alexeeva et al. 2018). Both approaches employ the Bethe approximation, namely they use the oscillator strength  $f_{ij}$  and are thus only defined for permitted transitions. Some discussion of different approximations for forbidden and intercombination transitions can be found in Barklem (2016a). Similarly, the recipes of Bely & van Regemorter (1970) or Seaton (1962a) are often used for ionisation; the former typically has errors of around a factor of two.

For hydrogen collisions, the availability of reliable quantum mechanical data are much more limited. The challenge is that collisions in late-type stellar atmospheres fall in the low energy regime and calculations must take into account the structure of the quasi-molecule that forms as the hydrogen perturber and the atom or ion approach each other (Barklem et al. 2011). So-called “full quantum” (FQ) methods do this in two steps: first, using quantum chemistry calculations to describe the potential energies and the couplings for fixed nuclei (e.g. Croft et al. 1999, Dickinson et al. 1999, Guitou et al. 2010); and second, using these potentials and couplings in quantum mechanical scattering calculations (e.g. Belyaev & Barklem 2003, Belyaev et al. 2010, 2012). Relatively extended FQ rate coefficients are available for low-lying levels of neutral Li, Na, and Mg (Barklem et al. 2003, 2010, 2012). In light of these data it is now understood that charge transfer and mutual neutralisation ( $X_i + H \leftrightarrow X_j^+ + H^-$ ), dominate the overall statistical equilibrium for Li and Na (e.g. Barklem et al. 2021). For Mg, however, (de-)excitation ( $X_i + H \leftrightarrow X_j + H$ ) cannot be neglected (Osorio et al. 2015). In fact, by perturbing the rate coefficients of different transitions, it has been demonstrated for several species that (de-)excitation by hydrogen collisions can be the most important ingredient in the model atom (e.g. Amarsi & Asplund 2017, Amarsi et al. 2018a, 2019a, 2020a). For Na and Li, the FQ data for mutual neutralisation compare well against recent measurements from the Double Electrostatic Ion Ring Experiment (DESIREE; Schmidt et al. 2013, Eklund et al. 2020, 2021) as well as from UCLouvain (Launoy et al. 2019), at least to the level where the discrepancies do not significantly affect non-LTE abundance determinations (Barklem et al. 2021). The analogous comparisons for Mg, however, have highlighted the practical challenges of carrying out complete and detailed FQ calculations for complex species (Grumer et al. 2022, 2023).

Recent years have seen the development of so-called “asymptotic models” for inelastic hydrogen collisions (Belyaev 2013, Barklem 2016b). These models should not be confused with FQ models described above: rather than quantum chemistry calculations and quantum mechanical scattering calculations, asymptotic models employ a more simplified description of the potentials and couplings (for example, linear combinations of atomic orbitals) and of the collision dynamics (usually based on the semi-classical Landau–Zener model). Nevertheless, comparisons with the FQ data for Li, Na, and Mg show good agreement for (de-)excitation and charge transfer or mutual neutralisation processes, at least for the low-lying levels included in the FQ dataset and for the processes with the largest rate coefficients, suggesting order of magnitude accuracies (Barklem 2016a). Asymptotic model data are now available for many species (e.g. for Fe, Yakovleva et al. 2019 and Barklem 2018a; see also other papers by these authors and collaborators).

The asymptotic models predict zero rate coefficients for highly excited levels with energies less than 0.754 eV to the ionisation threshold (corresponding to the electron affinity of hydrogen). This is because these models describe a particular interaction mechanism, namely electron transfer between the atom and the hydrogen perturber via radial couplings at avoided ionic crossings (Barklem et al. 2011). For levels above this energy, the valence electron cannot bind to the hydrogen perturber. The free electron model of Kaulakys

(1991), describing momentum transfer between the perturber and the outer electron is appropriate to use here (e.g. Osorio et al. 2015), and codes are available to calculate these rates (Barklem 2017). Even below this threshold, asymptotic models predict low rate coefficients for collisional interactions happening at long and short internuclear distances, where other interaction mechanisms dominate. Thus, adding the coefficients from the asymptotic model and the free electron model together may lead to a better overall description of hydrogen collisions; as discussed in Amarsi et al. (2018a), the two models describe different interaction mechanisms and thus do not double count rates. Such an “asymptotic+free” approach has been shown to better reproduce the CLVs of lines of O I (Amarsi et al. 2018a, Bergemann et al. 2021) and C I (Amarsi et al. 2019a); this was also ultimately adopted by Bergemann et al. (2019) in their study of Mn I lines. The caveat is that the free electron model is valid in the limit of high effective principal quantum numbers; extending to lower  $n^*$  is an extrapolation, but arguably necessary in the absence of a more complete theory.

In the absence of asymptotic model data for inelastic hydrogen collisions, it is still common to use the Drawin recipe (see Appendix A of Lambert 1993). As discussed in Barklem et al. (2011) the recipe does not describe the physics in the low-energy regime relevant here. It is thus usual to scale the Drawin rate coefficients with a scale factor  $S_H$ , that can be calibrated astrophysically (e.g. Mashonkina et al. 2023), or possibly by comparison with the rate coefficients of some similar species. Another approach might be to use the general empirical fitting method presented in Ezzeddine et al. (2018), the results of which could be combined with the free electron model as described above.

**2.2.4. Model atom reduction.** Comprehensive model atoms as described above are usually too complex to be used for 3D non-LTE abundance analyses, given the high cost of the post-processing calculations. Reducing the complexity of the level structure sets the stage for further reductions, and a common first step is to merge fine structure levels: levels differing in energy and total angular momentum  $J$  can be collapsed into single terms labelled by their configurations as well as  $S$ ,  $L$ , and  $P$  (here assuming LS-coupling). The simplest approach is as follows:

$$g_I = \sum_{i \in I} g_i \quad (1)$$

$$E_I = \sum_{i \in I} E_i \frac{g_i}{g_I} \quad (2)$$

This exactly conserves the total LTE populations in the limit of zero energy differences between the fine structure sublevels. The corresponding assumption is that the fine structure sublevels are in relative LTE, meaning that their departure coefficients  $b_i \equiv n_i/n_{i,\text{LTE}}$  are identical. This holds if, for example, the levels are efficiently coupled via inelastic hydrogen collisions (Sect. 2.2.3).

Analogously, levels with different configurations and quantum numbers can be merged into super levels (Anderson 1989). As before, the assumption is that the merged levels are in relative LTE. It therefore makes sense to merge similar levels together, for example those that are close in energy, those that have the same core configurations, those in the same spin system  $S$  and with the same parity  $P$ , or those that are close in orbital angular momentum  $L$ . In general, the merging should be at least validated a posteriori via non-LTE radiative transfer calculations on 3D RHD model atmospheres, or <3D> or 1D columns, that are representative of the stars of interest. In some cases, very simple level structures can be



constructed in this way depending on the lines and stars of interest (e.g. the five level atom of [Leenaarts et al. 2013](#), used to study the Mg II H and K lines in the solar atmosphere).

Reducing the number of radiative transitions in the model atom is an effective way of reducing the overall computational cost of the post-processing calculations. For levels merged into terms and super levels, one can merge transitions into super transitions. There are multiple ways to approach this, that give slightly different results. For example, for lines  $i \rightarrow j$  with oscillator strengths  $f_{ij}$  connecting components of the super levels  $I$  and  $J$ , the oscillator strength of the super line  $f_{IJ}$  could be defined as follows:

$$f_{IJ} = \left( \sum_{i \in I} g_i \exp(-E_i / (k_B T_a)) \right)^{-1} \sum_{j \in J} \sum_{i \in I} f_{ij} g_i \exp(-E_i / (k_B T_a)) \quad (3)$$

Here  $T_a$  is a typical temperature for the line-forming region of the atmosphere (e.g. 5500 K). All other quantities can then be determined consistently based on these merged values to ensure the correct asymptotic behaviour. Bound-free transitions can be merged in a similar fashion, for example replacing  $f_{ij}$  with the photoionisation cross-sections  $\sigma_{ij}$ ; this is identical to Eq. 18.160 of [Hubeny & Mihalas \(2015\)](#) when the occupation probabilities are set to unity.

Even when lines in the model atom are merged as per Eq. 3, for important lines (Sect. 2.2.2) it is desirable to explicitly consider the splitting of bound-bound opacity for the calculation of  $J_\nu$ . For example, a particular radiative transition can be described as a composite of Voigt profiles of different strengths and centred on different wavelengths. [Steffen et al. \(2015\)](#) describe another efficient approach for the O I 777 nm triplet, where the oscillator strength of the collapsed line profile (Eq. 3) is artificially reduced by a factor of three, only for the calculation of  $J_\nu$ .

A complementary approach to the reduction of the model atom is based on consideration of the radiative bracket,  $n_i R_{ij} - n_j R_{ji}$ . One can carry out non-LTE radiative transfer calculations on representative 3D RHD model atmospheres, or <3D> or 1D columns to calculate these quantities. Radiative transitions with small absolute radiative brackets can be identified and excluded from the model atom, while retaining the collisional coupling. This approach was adopted by [Lind et al. \(2017\)](#) and [Mallinson et al. \(2022\)](#) for the study of Fe and Ti line formation, respectively. Investigations into more complex ways of merging and removing transitions, perhaps in a semi-automated way to minimise changes in departure coefficients (e.g. [Bard & Carlsson 2008](#)) or with the aid of machine learning algorithms, could be beneficial for more accurate 3D non-LTE modelling of complex species.

Unlike for radiative transitions, including more collisional transitions does not significantly impact the cost of 3D non-LTE spectrum synthesis. Nevertheless, it may be necessary to merge collisional transitions associated with super-levels. This can be done in an analogous way to radiative transitions: for example, by using Eq. 3 or and replacing  $f_{ij}$  with the upwards rate coefficient. For a given collisional transition, it is advisable to specify only either the upward or downward (merged) rate coefficient in the model atom, and then to calculate the rate of the reverse process consistently in the spectrum synthesis code via detailed balancing. This ensures that the solution converges to LTE in the deep layers, and in the limit of very large collisions.

**2.2.5. Cost.** Compared to the 3D RHD models (Sect. 2.1.4) and the 3D non-LTE spectrum synthesis (Sect. 2.3.6), it is less relevant to talk about computational costs for the model atoms, because most non-LTE modellers interested in stellar abundances are primarily compiling data already available in the literature, rather than carrying out atomic and

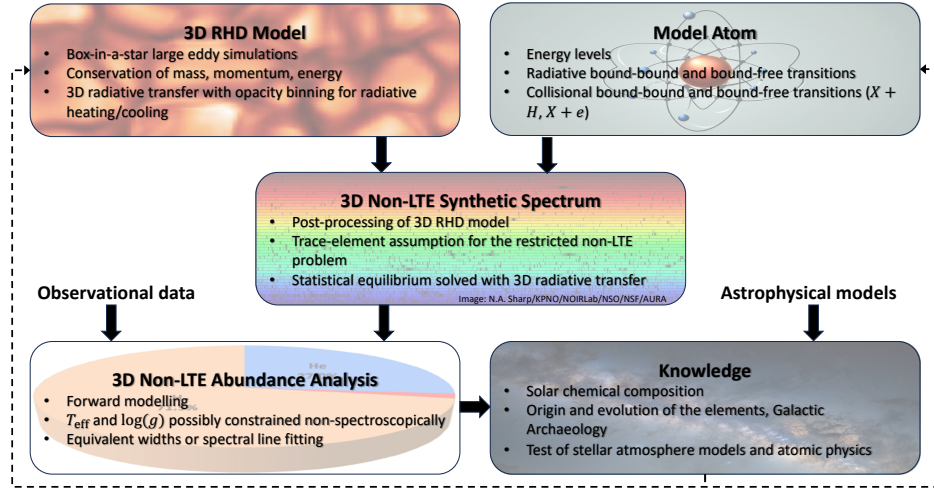


**Figure 5:** Highly simplified schematic of the workflow for 3D non-LTE abundance analyses.

molecular structure calculations themselves. Nevertheless, the human time for even this task can be considerable; a whole PhD thesis can easily be based around constructing and using a model atom for just one or two elements. The most time consuming tasks include linking together datasets in a consistent way when these datasets have different formats and often with sometimes inconsistent labelling or different physical assumptions; and reducing the complexity of the atom and validating this reduction. Semi-automated approaches are possible for light elements by utilising the databases listed in Sect. 2.2. However, these do not always contain the best available data; especially, as noted above, they do not contain data for inelastic hydrogen collisions.

### 2.3. Spectrum synthesis

Abundance analyses proceed via forward modelling (Fig. 5), that is to say one starts with constructing realistic synthetic spectra with different parameters, and then fits them to observational data to deduce stellar properties. These synthetic spectra are usually constructed via post-processing of model atmospheres: the model atmospheres are constructed first with a simplified treatment of radiative transfer (with opacity bins, and with a Planck source function, possibly with some treatment for isotropic, coherent scattering in the continuum), that is assumed to be sufficient for describing the radiative heating and cooling rates; and the synthetic spectra are calculated in a separate step, often with an independent code, by employing detailed radiative transfer calculations with typically much higher frequency resolution and with more accurate atomic, ionic, or molecular data relevant to the spectral lines of interest.

Furthermore, it is common to invoke the trace-element approximation, and to only consider the restricted non-LTE problem. The first approximation means that differences between the elemental abundances of a suitably chosen model atmosphere (for example with  $[\text{Fe}/\text{H}]$  chosen to match observations, and the other elements appropriately scaled



relative to the solar composition) and those of the star do not correspond to significant errors in the model atmosphere structure. The analysis can then proceed by varying the abundances only in the post-processing stage, without recomputing the model atmospheres themselves. The trace-element approximation is also commonly used in 1D LTE analyses. The restricted non-LTE problem is closely related; changes to the absorber populations and hence opacities due to non-LTE modelling are assumed to be sufficiently small to not significantly affect the model atmosphere structure.

**2.3.1. Codes.** There are a handful of codes that have been used for 3D non-LTE abundance analyses of late-type stars. Most results have been based on either the frequency- and domain-decomposed MPI-parallelised codes `Multi3D` (Botnen & Carlsson 1999, Leenaarts & Carlsson 2009) and its offshoot `Balder` (Amarsi et al. 2018b); or `NLTE3D` (Cayrel et al. 2007), the latest version of which solves the full 3D non-LTE radiative transfer problem (Steffen et al. 2015, Steffen 2017). We also refer the reader to the MPI-parallelised code `PORTA` (Štěpán & Trujillo Bueno 2013), that has to our knowledge not yet been used for 3D non-LTE abundance analyses and the 3D LTE codes `LinFor3D`, which can read departure coefficients (Gallagher et al. 2017b), `Scate` (Hayek et al. 2011), `OPTIM3D` (Chiavassa et al. 2009), or `ASSET` (Koesterke et al. 2008). Several other relevant codes use the so-called 1.5D approximation, whereby each column of the 3D RHD model atmosphere is treated independently for the solution of the statistical equilibrium. The quality of this approximation depends on the line, species, and star as well as the desired accuracy (e.g. Sect. 3.3 of Amarsi et al. 2016a for a discussion about the O I 777 nm lines; and Sect. 3.2.3 of Nordlander et al. 2017 for a discussion of various lines in an ultra metal-poor star). Several important studies of line formation in the Sun have used the 1.5D code `NATAJA` (Shchukina & Trujillo Bueno 2001). Readers interested in developing or using codes themselves might also look at the open-source, MPI-parallelised 1.5D non-LTE codes (Pereira & Uitenbroek 2015), and `NICOLE` (Socas-Navarro et al. 2015). As we discussed in Sect. 2.1.1, 3D LTE synthetic spectra tend to be in good agreement when using different radiative transfer codes and model atmospheres. Unfortunately, systematic comparisons of 1.5D or 3D non-LTE calculations have not yet been performed, and one expects larger differences owing in particular to different treatments of background opacity (Sect. 2.3.5)

**2.3.2. Overview of post-processing in 3D LTE.** Post-processing in 3D non-LTE, like that in 3D LTE, 1D non-LTE, and 1D LTE, usually begins by calculating the EOS and extinction and emissivity coefficients in LTE. Two or more state variables, for example temperature and gas density, are extracted from the model atmospheres as a function of 1D or 3D geometric space. For the 3D RHD models, several temporal snapshots are considered individually. Next, given these quantities as well as the elemental abundance ratios (which, under the trace-element approximation, do not necessarily correspond exactly to that with which the model atmosphere was constructed), the EOS and the monochromatic LTE opacities are re-determined (Sect. 2.1.3). The careful treatment of line profiles is crucial for spectral line fitting; metal-line profiles are usually treated with Voigt profiles with collisional broadening by hydrogen atoms best accounted for via ABO theory (Barklem et al. 2000), while hydrogen line profiles can include self-broadening and Stark broadening for example via the `HLINOP` suite of software (Barklem 2016a, and references therein).

The radiation field and hence the emergent intensity can be calculated by solving the radiative transfer equation, given the model atmosphere, EOS, and opacities. We refer the

reader to [Rutten \(2003\)](#) and [Hubeny & Mihalas \(2015\)](#) for an introduction into radiative transfer in stellar atmospheres, and, for example, [Auer \(2003\)](#) and [de Vicente et al. \(2021\)](#) for an overview of the associated challenges. The latter authors suggest that short characteristics methods, which are more efficient for multidimensional problems and parallelise well, are sufficiently accurate provided one is interested in spatially-integrated spectra. [Ibgui et al. \(2013\)](#), [Štěpán & Trujillo Bueno \(2013\)](#), and [Steffen \(2017\)](#) describe the implementation of such methods on 3D cartesian grids. For box-in-a-star 3D RHD models as well as for semi-infinite 1D models, one solves the radiative transfer equation along several outgoing rays of different inclinations  $\mu = \cos \theta$ , where the vertical ray at  $\mu = 1$  corresponds to light emergent from the centre of the stellar disc; in 3D one must also solve for different azimuthal angles  $\phi$ . The astrophysical flux can then be obtained via disc-integration, adopting a suitable angle quadrature ([Štěpán et al. 2020](#), [Jaume Bestard et al. 2021](#)). Abundance analyses based on spectral line fitting (rather than equivalent widths) must take macroscopic broadening effects into account. In particular, rotational broadening can be added following [Dravins & Nordlund \(1990\)](#) or [Ludwig \(2007\)](#), and the synthetic profiles must also be convolved with the instrumental profile.

Post-processing of 1D and <3D> models invoke at least two additional parameters, microturbulence and macroturbulence (e.g. [Piskunov & Valenti 2017](#)). They are necessary to account for spectral line broadening primarily due to the velocity gradients, on scales much smaller than or much larger than an optical depth, respectively. Despite their names, they are explained by stellar granulation rather than by turbulence ([Nordlund et al. 1997](#)), and are thus predicted from first principles by the 3D RHD simulations ([Asplund et al. 2000a](#)). Not having to deal with these imperfect fudge parameters ([Steffen et al. 2013](#)) is a major advantage of 3D abundance analyses.

**2.3.3. Solving for the statistical equilibrium.** Moving to non-LTE brings about additional complications. We once again recommend [Rutten \(2003\)](#) and [Hubeny & Mihalas \(2015\)](#) for an introduction into this topic. In brief, rather than assuming that absorber populations are given by the Saha ionisation equation and the Boltzmann distribution, one solves for the time-independent equations of statistical equilibrium:

$$n_i \sum_{j \neq i} (R_{ij} + C_{ij}) - \sum_{j \neq i} n_j (R_{ji} + C_{ji}) = 0 \quad (4)$$

Here,  $n_i$  are the number densities of atoms or ions in a particular level  $i$ ,  $R_{ij}$  and  $C_{ij}$  are the total radiative and collisional rates (with dimensions  $T^{-1}$ ) from level  $i$  to level  $j$ , which are calculated given the radiative transition probabilities or cross-sections (together with the angle-averaged intensity  $J_\nu$ ) and collisional rate coefficients described in the model atom. Sect. 9.2 of [Hubeny & Mihalas \(2015\)](#) explains how Eq. 4 follows from the Boltzmann transport equation. A more general form of this equation has a source term on the right hand side,  $dn_i/dt = \partial n_i/\partial t + \nabla \cdot (n_i \mathbf{v})$ ; this is set to zero under the assumption that the radiative and collisional transitions happen on much shorter timescales than the dynamical timescales in the stellar atmosphere. To a good approximation, the particles follow Maxwellian velocity distributions (see Chapter 4 of [Hubeny & Mihalas 2015](#)); as such Eq. 4 reflects the competition between inelastic collisions that bring the overall system closer to LTE, and radiative processes that in general drive the system away from LTE.

The equations are closed by number conservation:

$$\sum_i n_i = N \quad (5)$$

Here,  $N$  is the total number density of particles in all of the levels of the atoms, ions, and possibly molecules described in the model atom. The quantity  $N$  is extracted from the LTE EOS (and excludes any nuclei locked away in species not explicitly described by the model atom; this could be, for example, molecules and more than doubly-ionised species). Eq. 4 and Eq. 5 are solved at every gridpoint in the model atmosphere. The radiative rates require  $J_\nu$ , which is obtained by solving the radiative transfer equation. The radiative transfer equation, however, depends on the extinction and source function which depend on the absorber populations  $n$ . As such, the equations are non-linear; they are also non-local, as the radiation couples different parts of the atmosphere together.

Multi3D, Balder, and NLTE3D solve the non-linear Eq. 4 as well as the radiative transfer equation iteratively, preconditioning them (analogous to linearising them; Socas-Navarro & Trujillo Bueno 1997) as per Multi-level Accelerated Lambda Iterations (MALI; Rybicki & Hummer 1992, see also Auer et al. 1994) which is a generalisation of the method presented in Olson et al. 1986. It is common to use a local (diagonal) approximate operator, amounting to Jacobi iterations; this is simple to implement and parallelise well in 3D, compared to more complex approaches, for example Gauss-Seidel iterations (Trujillo Bueno & Fabiani Bendicho 1995) that have better convergence properties. The MALI approach is usually combined with acceleration methods (Auer 1991) that can help increase the convergence rate and prevent the iterations from stabilising away from the true solution. In the near future, significant improvements to convergence rates could be had via the use of multigrid methods (Fabiani Bendicho et al. 1997, Bjørgen & Leenaarts 2017), non-stationary methods (Paletou & Anterrieu 2009, Lambert et al. 2016), or asynchronous iterations implemented within the DISPATCH framework (Nordlund et al. 2018, Nordlund 2019).

The overall number of iterations depends on how close the initial guess is to the converged solution. For a given snapshot of a 3D RHD model atmosphere, the usual approach is to start with LTE populations (as well as  $J_\nu = B_\nu$  if background scattering is included). It should be possible to improve the initial guess based on the converged solutions from other snapshots of the same model, and possibly from snapshots of other models, perhaps using machine learning algorithms (Chappell & Pereira 2022).

**2.3.4. Sampling the 3D RHD models.** There are a number of compromises between accuracy and speed that must be made when carrying out 3D non-LTE spectrum synthesis calculations. Of the order of two to five snapshots are sufficient for analyses based on equivalent widths or abundance corrections to achieve a precision of 0.01 dex (Nordlander et al. 2017, Rodríguez Díaz et al. 2023). It is common to use up to 20 snapshots for analyses of profiles of weak lines (Deshmukh et al. 2022), but half that number has been shown to suffice (Rodríguez Díaz et al. 2023). Models in the Stagger-grid and CIFIST-grid tend to be down-sampled in the horizontal by factors ranging from two to four (Steffen et al. 2015, Amarsi & Asplund 2017); again introducing an abundance error smaller than 0.01 dex (Amarsi & Asplund 2017, Rodríguez Díaz et al. 2023). The tests of Nordlander et al. (2017) suggest that higher horizontal resolution is needed in 3D non-LTE compared to in 3D LTE. Conversely, it is desirable to increase the vertical resolution of the 3D RHD models, by trimming away the optically-thick layers and interpolating onto a new depth scale with finer resolution of the steep continuum-forming regions (Amarsi et al. 2018b).

Typically the angle-averaged intensity  $J_\nu$  is calculated using around 15 rays or 30 directions on the unit sphere (e.g. Klevas et al. 2016 use 17 rays). Amarsi & Asplund (2017) suggest to use the Lobatto quadrature for the integration over the cosine of the polar angle  $\mu = \cos \theta$  (i.e. the Gaussian quadrature but which is pinned on both of the integration limits, namely  $\mu = 1$  and  $\mu = -1$ ) and, for the inclined rays, trapezoidal integration over the azimuthal angle  $\phi$ . One advantage of this simple approach is that it results in the Lobatto quadrature in the limit of a horizontally homogenous, semi-infinite 1D atmosphere, and should give results close to the optimal Gauss quadrature. Nevertheless, it may be that the angle quadratures tailored for 3D applications proposed by Štěpán et al. (2020) and Jaume Bestard et al. (2021) give higher accuracy for the same number of rays.

**2.3.5. Background opacities and scattering.** The opacity contributed by background species can have a significant impact on the statistical equilibrium of the element under consideration. In particular, recent results (e.g. Amarsi et al. 2015, Wang et al. 2021) have demonstrated that it can be important to consider the opacity from background lines that overlap (blend with) the bound-bound transitions in the model atom. However, the computation of background opacity due to millions of atomic/ionic lines and billions of molecular lines, for  $10^6$  grid points of a 3D RHD model atmosphere snapshot and  $10^4$  frequency points of a model atom is computationally expensive. As such, to save time these can be precomputed and interpolated on the fly. `Balder` does this on a regular grid of logarithmic temperature and density, and a frequency grid that corresponds exactly to that of the model atom, for the chemical composition corresponding to that of the particular 3D RHD model.

It is common to consider some background continuum scattering processes, in particular Rayleigh scattering from H I on the red wing of the Lyman- $\alpha$  line. This is treated assuming the scattering is coherent and isotropic, such that the background continuum source function becomes  $S_\nu = \epsilon_\nu B_\nu + (1 - \epsilon_\nu) J_\nu$ , with background continuum photon destruction probability  $\epsilon_\nu$  (e.g. Hayek et al. 2011). Following Hayek et al. (2010) and Amarsi et al. (2020b), one can make a similar approximation for background lines via Eq. 22 of van Reemorter (1962) that can be modified to estimate  $\epsilon_\nu$  for a given line due to electron collisions and under the assumption of a two-level atom. This approach probably underestimates  $\epsilon_\nu$  by neglecting hydrogen collisions; this could easily be estimated via the Drawin recipe (see Appendix A of Lambert 1993). However, it may be better simply to treat background lines in true absorption ( $\epsilon_\nu = 1$ ) given the limitations of the two-level atom, and that coherent scattering is a poor approximation for weak lines in stellar photospheres (we note here that complete frequency redistribution is a good approximation at least for the solar photosphere; Uitenbroek & Bruls 1992). Perhaps it is instead worth moving away from the single-element approach altogether, and to develop more efficient algorithms for multi-element non-LTE calculations, which are now feasible at least in 1D (see below). Including scattering in the source function requires updating  $J_\nu$  (or the emissivity  $\eta_\nu$ ) after every MALI iteration. We note that the algorithm of Rybicki & Hummer (1992) can be modified to also use preconditioning for this background component, and this can slightly improve the overall convergence rate when these processes strongly affect the statistical equilibrium.

**2.3.6. Cost.** The cost of 3D non-LTE spectrum synthesis with respect to 1D LTE can be estimated under the assumption that the radiative transfer dominates the overall cost (which is often the case for simple model atoms) and that there are no overheads when scaling up the calculations and when doing 3D radiative transfer. For an entire spectrum

of lines of a given species or element, the non-LTE to LTE cost is then given by the number of iterations to reach convergence, which can be around 10 to 50. The 3D to 1D cost can be estimated via the number of snapshots, horizontal gridpoints, and azimuthal angles,  $N_t \times N_x \times N_y \times N_\phi$ , which is at least  $10^5$ . In all, the 3D non-LTE to 1D LTE cost comes to around  $10^6$  to  $10^7$  for an entire spectrum of a given species or element. Thus a 1D LTE analysis taking around 1 hour on a single CPU would amount to several million CPU hours in 3D non-LTE, necessitating the use of a supercomputer. If one is only interested in performing the abundance analysis with just a single line, these relative cost increase by an amount proportional to the number of lines in the model atom, which can be hundreds or sometimes thousands; the 3D non-LTE to 1D LTE cost then can reach around  $10^9$ .

## 2.4. Astrophysical validation

The physics underpinning 3D non-LTE models are far more sophisticated and realistic than the various simpler alternatives (1D LTE, 1D non-LTE, <3D> LTE, <3D> non-LTE, 3D LTE). Nevertheless, it is worth asking if this translates into more accurate abundance results overall. Various astrophysical tests of the 3D RHD models have been performed using the Sun as a testbench, for which  $\mu$ -resolved observations (e.g. [Ellwarth et al. 2023](#)) with high signal-to-noise ratios and resolving powers can be used; it is also the only star for which the uncertainties in  $T_{\text{eff}}$  and  $\log g$  can be neglected (in this context). The continuum limb darkening is better reproduced by 3D RHD models than by theoretical and semi-empirical 1D models as well as <3D> models (e.g. [Koesterke et al. 2008](#), [Pereira et al. 2013](#)), giving confidence to the mean temperature stratification predicted by the simulations. Intensity fluctuations ([Pereira et al. 2013](#)) as well as line shifts and asymmetries, none of which can be predicted by 1D models, are well-reproduced by 3D RHD models (e.g. [Asplund et al. 2000a](#), [Nordlund et al. 2009](#), [Pereira et al. 2009b](#)), giving confidence to the gas dynamics. Similarly, the profiles of strong H I Balmer and Paschen lines are better reproduced by 3D RHD models as discussed in Sect. 3.2.1.

Solar CLVs of spectral lines are a probe of coupled 3D non-LTE effects. Spectral lines observed towards the limb form higher up in the photosphere (in a cooler, less dense environment) than those observed at disc-centre. Lines of different excitation potential, and in different ionisation stages, and molecular lines, exhibit different CLVs, to first order due to their temperature and pressure dependences described by Saha-Boltzmann statistics. As such, CLVs are sensitive to the mean structure of the atmosphere. They are also sensitive to the fluctuations, due in part to the non-linearities, but in this case more because towards the limb one begins to see the granules edge-on ([Nordlund et al. 2009](#), [Uitenbroek & Criscuoli 2011](#)); as a consequence, in 1D one requires higher values of microturbulence to reproduce observations towards the limb ([Takeda 2022](#)) even though 1D inversions of the solar disc-centre intensity have microturbulence values that decrease with height ([Holweger & Mueller 1974](#)). Solar CLVs offer an opportunity to validate the model atom and the non-LTE modelling: departures from LTE are larger for lines observed towards the limb, where gas densities are lower and thus collisions are too infrequent to maintain Saha-Boltzmann statistics. In particular, the ionisation fraction decreases towards the cooler upper photosphere such that the ratio  $n_{\text{H}}/n_{\text{e}^-}$  increases steeply with height, and thus the CLV can be used to test the description of hydrogen collisions ([Allende Prieto et al. 2004](#), [Pereira et al. 2009a](#), [Steffen et al. 2015](#)) insofar as these are the largest uncertainty in the model atom. In practice, the method strives to reproduce the disc centre and limb spectra with

a uniform abundance. By virtue of such tests for O I and C I lines in 3D non-LTE, [Amarsi et al. \(2018a, 2019a\)](#) suggest to use the asymptotic+free approach for hydrogen collisions (Sect. 2.2.3), although this should be explored for more species. Despite these uncertainties, it is clear that 3D non-LTE outperforms 1D or <3D> LTE or non-LTE and 3D LTE (e.g. [Lind et al. 2017](#)) as also seen for Na I ([Canocchi et al. 2023](#), and Sect. 3.4.2).

For stars other than the Sun, analogous tests as those described above may soon be possible with the benefit of high fidelity observations of exoplanet transits (e.g. [Dravins et al. 2017, Maxted 2018](#)). In general, however, astrophysical validation for such stars comes from various consistency checks on inferred abundances. By similar arguments to the solar CLVs, the coupled 3D non-LTE effects influence the predicted strengths of spectral lines due to different levels of different species and forming at different heights in the atmosphere; the inferred abundances should all agree with each other to within the observational uncertainties. One can explore a wider parameter space by also considering benchmark stars for which stellar parameters are well-constrained on an absolute scale for example by means of interferometry and parallaxes (e.g. [Karovicova et al. 2018, 2020](#)), as discussed in Sect. 3.2.

Lastly, we note that the scatter in abundance-abundance planes can be dominated by systematics caused by the 1D or LTE assumptions. Analyses of large samples of stars thus offer a further way to validate the 3D non-LTE modelling, and reduced scatter can potentially reveal new and exciting astrophysics, as we elaborate on in Sect. 3. We stress that results from 1D models have various parameters that are calibrated to fit the observations, and as such, even when 1D or <3D> (non-)LTE abundances appear to give consistent results in terms of excitation, ionisation, or molecular equilibrium, the average abundance may still lie further from the absolute truth than 3D non-LTE.

## 2.5. 3D non-LTE effects on abundances

We present an overview of the physics behind some common 3D non-LTE effects. Specific results for different species and elements, and their astrophysical implications, are given in Sect. 3; moreover, general advice for astronomers working with 1D LTE abundances are provided in Sect. 4.

**2.5.1. 3D effects.** Before discussing the 3D effects on profile-integrated equivalent widths, we first note that there is a large literature on spectral line shapes (e.g. [Dravins et al. 1981, Dravins 1982](#)). The flow of gas due to stellar granulation, overshooting into the convectively-stable regions, impart net blueshifts, line asymmetries, and line broadening when considering spatially-integrated or disc-integrated spectra. This field has seen renewed interest due to their degeneracies with radial velocity signatures of exoplanets (e.g. [Dalal et al. 2023](#)). We refer the reader to other literature for a discussion of these effects (e.g. [Löhner-Böttcher et al. 2019, Dravins et al. 2021](#)). The severity and possibly the direction of the abundance corrections when inferred via spectral line profile fitting will depend on the adopted line masks and the treatment of rotational velocity. The line shape is particularly important for measurements of isotopic ratios, as discussed in Sect. 3.3.1 and Sect. 3.3.5.

For a first order understanding of the 3D effects on equivalent widths, it is helpful to separately consider the “stratification effects”  $\Delta_{\text{strat.}}$  due to differences in the mean atmospheric stratification, and the “granulation effects”  $\Delta_{\text{gran.}}$  due to temperature and velocity inhomogeneities. The former may be tested by comparing <3D> abundances to 1D abundances, and the latter by comparing 3D to <3D> (all in non-LTE). Fig. 6 shows an

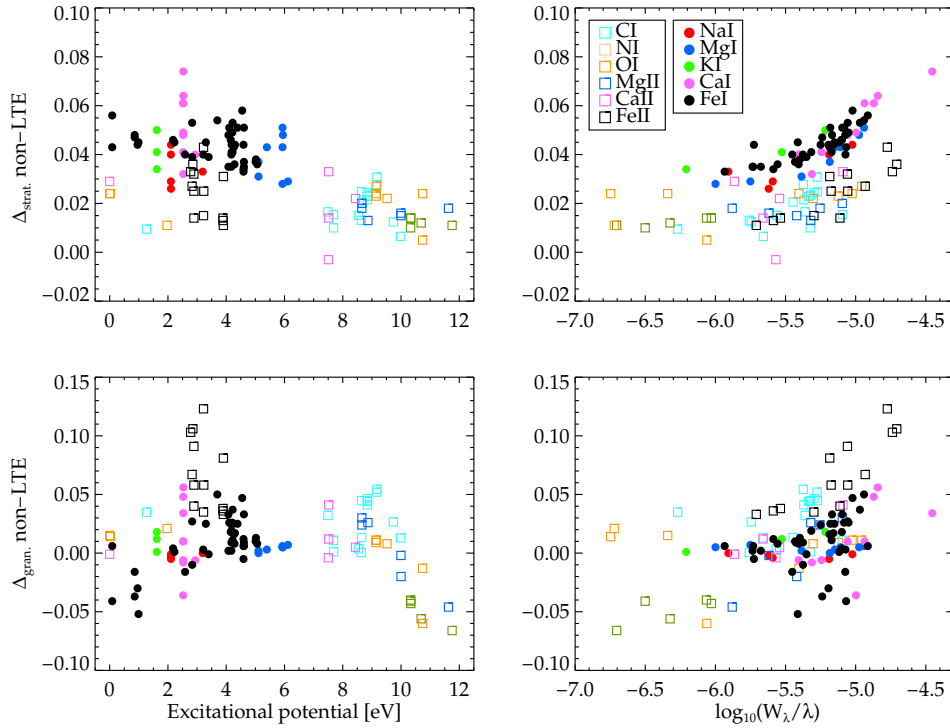


**Figure 6:** The difference in solar abundances determined under different assumptions; the top panels represent the influence of the atmospheric stratification by showing the difference between abundances determined in <3D> and 1D ( $\Delta_{\text{strat.}}$ ), and the lower panels represent the impact of granulation by showing the difference between 3D and <3D> abundances ( $\Delta_{\text{gran.}}$ ). All abundances have been computed in non-LTE, and are based on analyses of the disc-centre intensity. The data have been compiled from [Amarsi et al. \(2019a, 2020a\)](#) and [Asplund et al. \(2021\)](#). Majority species are marked with open squares, minority species with filled bullets.

overview of  $\Delta_{\text{strat.}}$  and  $\Delta_{\text{gran.}}$  for eight of the elements that have been consistently analysed in 3D non-LTE in the solar disc-centre intensity. We note that the trends identified with line strength in these plots strongly depend on the adopted microturbulence in the 1D and <3D> analyses, here 1 km/s. We also emphasize that <3D> models are not unambiguously defined from their parent 3D models, but depend strongly on the averaging method, in particular the reference depth scale (geometric, column mass, optical depth) as demonstrated by [Magic et al. \(2013b\)](#), as well as the choice of which quantities to average and which (if any) to recalculate from the EOS. The <3D> models represented in Fig. 6 have been computed by averaging the logarithmic gas density, and the gas temperature raised to the fourth power, on surfaces of equal Rosseland optical depth ([Amarsi et al. 2018a](#)).

The stratification effects  $\Delta_{\text{strat.}}$  show a clear trend, with increasingly positive values with increasing line strength, essentially independently of excitation potential, with minority species more affected than majority species. This is likely a consequence of the slightly shallower temperature gradient of the <3D> model (line weakening) combined with a slight



reduction in electron density (line strengthening of majority species). In metal-poor stars, the effect of the mean stratification is more prominent. Although for example the Sun is approximately in radiative equilibrium (Nordlund et al. 2009), towards lower metallicities radiation plays a smaller role on the energy balance, and the upper layers are able to cool efficiently as the upflows overshoot into the convectively-stable regions and expand (the 1D models are too hot). For example, Bergemann et al. (2012) show that Fe I are typically strengthened and Fe II lines typically weakened in <3D>-models of metal-poor stars.

The granulation effects show more complex behaviour. For weak lines in the Sun, Fig. 6 shows that  $\Delta_{\text{gran.}}$  is close to zero. The exception is for minority species of low excitation potential ( $< 1 \text{ eV}$ ), and majority species of high excitation potential ( $> 10 \text{ eV}$ ). These are also the most temperature-sensitive lines: For minority species, the ratio between line opacity and continuous opacity (when the latter is dominated by  $H^-$ ) scales approximately with  $\exp(I - (E_i + E_{H^-}))/k_B T$ , where  $I$  is the ionisation potential,  $E_i$  the excitation potential, and  $E_{H^-} = 0.754 \text{ eV}$  is the electron affinity of hydrogen. Low excitation lines are therefore more temperature sensitive. For majority species, both neutral and ionized, the ratio scales as  $n_e T^{3/2} \exp(-(E_i + E_{H^-}))/k_B T$ , explaining why high-excitation lines of majority species react more strongly to temperature changes. Typically, the larger the temperature-sensitivity of the line under investigation, the larger the impact of granulation. Dobrovolskas et al. (2013) and Kučinskas et al. (2013) draw similar conclusions based on fictitious weak-line analysis in LTE in red giants, but they also show that different elements can react very differently at low metallicity. Partially or fully saturated lines are expected to be more strongly sensitive to granulation in general, because the atmospheric inhomogeneities become more pronounced at higher layers, where desaturation and strengthening in 3D by fluctuations should lead to negative  $\Delta_{\text{gran.}}$  compared to when neglecting velocity fields; however, the calibration of the microturbulence parameter makes this ambiguous and can produce positive  $\Delta_{\text{gran.}}$  (see for example Fig. 3 of Amarsi et al. 2022).

Although not illustrated in Fig. 6, extreme granulation effects can be found for molecular lines. Inhomogeneities in the 3D models leads to enhanced molecule formation in the cool pockets of gas, leading to extreme negative abundance corrections for CO (Uitenbroek & Criscuolo 2011, Amarsi et al. 2021). In the most metal-poor stars, the stratification effect can also be significant, but the granulation effect dominates (Dobrovolskas et al. 2013).

**2.5.2. Non-LTE effects.** One can begin a physical interpretation of non-LTE effects on multi-level atoms by considering two-level and three-level atoms, as presented by Rutten (2003) and in Chapter 14 of Hubeny & Mihalas (2015). The two fundamental effects are photon losses and photon pumping. Via bound-bound transitions, these lead to over-deexcitation and over-excitation of populations relative to LTE; while via bound-free transitions they lead to over-recombination and over-ionisation. The effects are driven by splits between  $J_\nu$  and  $B_\nu$  that occur naturally across the spectrum even in LTE, because of how the Planck function’s sensitivity to temperature varies with wavelength.

Photon losses occur because photons manage to scatter large distances when they are emitted via a bound-bound or bound-free transition, instead of being immediately reabsorbed as per thermodynamic equilibrium. As described by Rutten (2003), the loss of photons by back-scattering to deeper layers is not compensated for by the reverse effect in the lack of incoming light, and therefore the emergent intensity is reduced by such processes. The imbalance between photoexcitations and photoemissions shifts the equilibrium relative to LTE with fewer atoms (or ions or molecules) sitting in the upper level of the



bound-bound or bound-free transition, and more sitting in the lower level. Photon pumping is the opposite: here an excess of photons are absorbed compared to that expected from the local Planck function, these photons typically scattering out of the deeper, hotter layers of the atmosphere, and is typically very effective for UV transitions because the Planck function has a steep temperature gradient at such wavelengths.

In a multi-level atom, the non-LTE effects of individual transitions may enhance or cancel each other; for example can a 'ladder' of bound-bound transitions with high scattering probability lead to efficient photon losses, referred to as photon suction (e.g. Carlsson et al. 1994). To understand which radiative transitions are most influential for the statistical equilibrium of a given model atom and atmosphere, we recommend to start by inspecting the size of the radiative bracket (e.g. Lind et al. 2012). The strengthening or weakening of a given line can be understood by a combination of the change in opacity (proportional to the departure coefficient of the lower level) and the source function (proportional to the ratio between the upper and lower departure coefficient in the Wien regime).

The same effects that are frequently studied in atoms are also of relevance to molecules. Quantitative studies of non-LTE effects on molecules have been limited by their complexity and the lack of required data. Thompson (1973) and Hinkle & Lambert (1975) have shown that ro-vibrational transitions within the ground electronic state of diatomic molecules are collisionally controlled and thus should not show departures from LTE, and this appears to be borne out in calculations for the Sun (Ayres & Wiedemann 1989, Schweitzer et al. 2000, Uitenbroek 2000). On the other hand, Hinkle & Lambert (1975) show that excited electronic states may be radiatively coupled to the ground state, rather than collisionally; and using a simple two-level atom, Asplund & García Pérez (2001) demonstrate abundance effects of the order 0.2 dex for electronic UV lines of the OH molecule. Species with small dissociation energies may be susceptible to over-photodissociation, and recent calculations by Popa et al. (2023) suggest this could be significant for CH ( $E_{\text{dis.}} = 3.47$  eV). Accurately quantifying these effects requires reliable cross-sections for excitation and ionisation by collisions with electrons and with hydrogen atoms, which are still lacking.

Another kind of departure from LTE was recently investigated by Deshmukh & Ludwig (2023). The authors challenged the hypothesis that the longer chemical timescales of metal-poor stars may cause deviations from molecular equilibrium, and thereby bias abundance determination under this assumption, by allowing time-dependent chemistry of CO, OH, CH, CN, C<sub>2</sub> in 3D hydrodynamic atmospheres of metal-poor dwarfs. They conclude that the molecules are generally in equilibrium throughout the photospheres, but that deviations can be present in shallow layers, in particular for stars with C/O ratios much greater than unity. However, the deviations are unlikely to contribute significantly to spectroscopic measurements because the key diagnostic species CH and OH are formed in deeper layers.

**2.5.3. Coupling of 3D and non-LTE effects.** Although we have discussed 3D and non-LTE effects separately, in reality the two are coupled. This coupling can be quantified in terms of abundances for example by comparing the 3D non-LTE result  $A_{3N}$  with the approximation that is obtained by separately applying 3D LTE and 1D non-LTE abundance corrections to the 1D LTE result, namely  $A_{\text{approx.}} = (A_{3L} - A_{1L}) + (A_{1N} - A_{1L}) + A_{1L}$ . For Fe I lines in the ultra metal-poor G-dwarf SDSS J102915.14+172927.9 (Caffau et al. 2011a), one finds, for Fe,  $A_{3N} = 3.28$ , and  $A_{\text{approx.}} = (-0.10) + (0.25) + 2.80 = 2.95$  (Lagae et al. 2023). Similarly, for the K-giant SMSS J031300.36-670839.3 (Keller et al. 2014) one finds upper limits on the Fe abundance of  $A_{3N} = 0.97$ , and  $A_{\text{approx.}} = (-0.34) + (0.61) + 0.16 = 0.43$

(Nordlander et al. 2017). For Li in a very metal-poor dwarf (Wang et al. 2021, Sect. 3.3.1),  $A_{3N} = 2.02$  and  $A_{\text{approx.}} = (-0.21) + (-0.07) + 2.00 = 1.72$ . Thus,  $A_{\text{approx.}}$  is 0.3 – 0.5 dex too low, reflecting how the steeper gradients in the 3D RHD models enhance the non-LTE overionisation of the minority neutral species (Amarsi et al. 2016b). For the Sun, both 3D and non-LTE effects are smaller and so is the inferred error if lines are selected with care.  $A_{\text{approx.}}$  is accurate to within  $\pm 0.03$  dex for several species according to Asplund et al. (2021, Table A1). For Ba, Gallagher et al. (2020) show that  $A_{\text{approx.}}$  would underestimate the abundance by 0.05 dex.

In general, for species with significant departures from LTE, 1D (non-)LTE abundances are often closer to 3D non-LTE than are the 3D LTE abundances. Nevertheless, we stress that 3D LTE should be preferred when departures from LTE are negligible, such as for lines of Fe II (Amarsi et al. 2022) or the forbidden [O I] lines (Amarsi et al. 2016a).

**2.5.4. Magnetic fields.** Aside from the simplified treatment of radiative transfer (Sect. 2.1.3), it could be that the most important missing physics in the context of 3D non-LTE stellar abundances comes from magnetic fields. The use of 3D RMHD model atmospheres for abundance analyses of late-type stars analyses have so far been largely explorative, and limited to the Sun. Pilot studies were carried out by Fabbian et al. (2010, 2012) and Fabbian & Moreno-Inertis (2015), who performed 3D RMHD simulations with a net vertical magnetic field using a modified version of *Stagger* (Galsgaard & Nordlund 1996). They found for example large effects on Fe I spectral lines corresponding to positive abundance corrections of the order 0.05 to 0.09 dex for simulations with mean unsigned vertical flux density of around 100 G (see Fig. 2 of Shchukina & Trujillo Bueno 2015).

However, local dynamo simulations with zero net vertical magnetic flux density might better reflect the actual case of the solar photosphere (Rempel 2014). Shchukina & Trujillo Bueno (2015), Shchukina et al. (2016) as well as Moore et al. (2015) have analysed the 3D RMHD MURaM local dynamo simulations of Rempel (2014), which have mean unsigned vertical flux density of around 80 G near the optical surface. They quantified the MHD effects on the equivalent widths of spectral lines of different species (C I, N I, O I, Fe I). The net effects are small; Moore et al. (2015) report abundance changes of the order +0.004 dex overall for Fe I lines, while Shchukina & Trujillo Bueno (2015) report slightly more severe effects of the order +0.014 dex. It should be noted that the effects grow for lines that form higher up in the atmosphere. At least in these studies, the MHD effects on spectral lines are mainly the indirect ones, namely due to changes in the atmosphere itself, which tend to weaken the lines. The direct effect due to Zeeman broadening tends to act in the opposite direction, strengthening lines and reducing inferred abundances.

### 3. RESULTS

In this section, we quantify 3D and non-LTE effects for late-type stars based on recent literature, and discuss the impact in four research fields: the Sun (Sect. 3.1), stellar parameters (Sect. 3.2), the origins of the elements (Sect. 3.3) and planet-host stars (Sect. 3.4).

#### 3.1. Solar modelling problem

High-quality spectroscopic observations of the quiet Sun today allow for the determination of the photospheric composition of 62 elements (Asplund et al. 2021). The abundance of a

handful of other elements can be detected in the solar wind (the noble gases) or be derived from molecular lines in sunspots (F, Cl, In, Tl). The solar chemical composition not only provides a fundamental reference frame for many fields of stellar and galactic astrophysics, but is crucial to model its interior structure and evolution. In the 20th century, spectroscopic analysis of the Sun pointed to a metal-to-hydrogen mass fraction  $Z/X = 0.0231$  (Grevesse & Sauval 1998) or higher. The decade to follow saw a downward revision of this value by approximately 10 – 20% (Asplund et al. 2009, Caffau et al. 2011c), thanks to many improvements on the 3D and non-LTE modelling and atomic data, but a strong consensus between competing groups is still lacking. Recently, a claim was made that the photospheric metallicity is in fact very close to the 25 year old canonical value,  $Z/X = 0.0225$  (Magg et al. 2022), based on <3D>-modelling.

The reduction of the abundances of a handful of key elements caused a reduction of opacity in the solar interior, with the consequence that standard solar models could no longer well reproduce the sound speed profile as determined from helioseismic inversions of the p-mode oscillations (e.g. Basu & Antia 2008). The offset is particularly large, of order 1%, in the radiative zone just below the convective envelope. The largest contributions, > 80% in total, to the Rosseland opacity in this region are provided by O, Ne, and Fe and the abundances of these elements thus have the largest impact on the sound speed (Villante et al. 2014). Fig. 7 depicts how the use of different model atmospheres have affected the inferred solar O abundance over time. There are no detectable Ne lines forming in the solar photosphere, and so the solar Ne abundance must be inferred through indirect means, for instance via spectroscopy of the transition region (Young 2018) and of solar flares (Landi & Testa 2015), or via measurements of the solar wind (Heber et al. 2009, Burnett et al. 2019). However, as discussed in Asplund et al. (2021), care must be taken to account for fractionation relative to the solar photosphere due to the so-called FIP effect. Important metal opacity is also provided by C, N, Mg, Si, S, and Ni, while remaining elements contribute individually by less than  $\sim 1\%$  in this region (Krief et al. 2016). To shed light on the solar modelling problem, it is of particular interest to understand how 3D RHD models and non-LTE line formation have affected the solar abundances of the largest opacity contributors, and what the remaining uncertainties are and we comment on these elements individually in Sect. 3.1.1 to 3.1.4.

**3.1.1. Carbon and nitrogen.** The 3D non-LTE line formation of atomic lines of C I and N I in the Sun was recently investigated for the first time by Amarsi et al. (2019a, 2020a), with subsequent updates (Li et al. 2021, 2023a, Asplund et al. 2021). Here, we summarize the main conclusions. Both species have highly excited (7 – 9 eV for C, 10 – 12 eV for N) permitted atomic lines that can be used for abundance determination. Photon losses in these lines create sub-thermal line source function and small negative non-LTE effects that do not exceed  $-0.07$  dex for C and  $-0.02$  dex for N (using disc centre intensity). Larger negative effects were found in 1D for infrared lines of C by Caffau et al. (2010a) and Alexeeva & Mashonkina (2015); however, these studies predated the arrival of asymptotic models for inelastic hydrogen collisions (Amarsi & Barklem 2019). The low-excitation forbidden [C I] line at 872 nm is formed in LTE.

As evident from Fig. 6, the granulation effect, as measured by  $\Delta_{\text{gran}} = 3\text{D abundances} - \langle 3\text{D} \rangle \text{ abundances}$ , has the opposite sign for C (+0.02 dex, Caffau et al. 2010a, Amarsi et al. 2019a) and N ( $-0.05$  dex Caffau et al. 2009, Amarsi et al. 2020a), as a consequence of the difference in lower-level excitation potential. Magg et al. (2022) analysed a

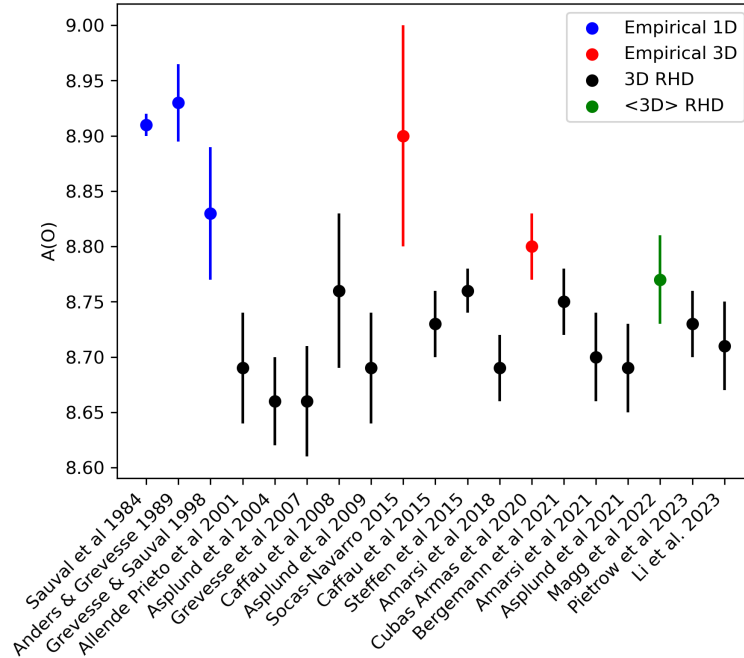


**Figure 7:** The evolution of the Solar photospheric O abundance over the last 40 years, colour-coded by the type of model atmosphere employed in the analysis.

subset of three atomic C I lines and two N I lines in <3D> LTE and found abundances that are  $\sim 0.10$  dex higher than Amarsi et al. (2019a) and Li et al. (2021) for C and  $\sim 0.15$  dex higher than Amarsi et al. (2020a), when differences in oscillator strengths have been accounted for. On first look, these differences are too large to be explained by granulation effects and the agreement is significantly better when 1D LTE MARCS models are used. The high result of Magg et al. (2022) may be related to the treatment of the blending CN lines or to the limitations and possible ambiguity connected to <3D> models (Sect. 2.5.1).

The 3D LTE line formation calculations of C<sub>2</sub>, CH, CO, NH and CN by Amarsi et al. (2021) highlight their larger sensitivity to granulation, in particular for CO where  $\Delta_{\text{gran}} = -0.2$  dex. The C abundance inferred from molecular lines agrees well with the 3D non-LTE abundance from atomic lines, while the N abundance inferred from molecular lines is  $\sim 0.1$  dex higher than the most recent 3D non-LTE N abundance from atomic lines (Amarsi et al. 2020a). The difference cannot be explained by uncertainties in atomic oscillator strengths (Li et al. 2023a). The CLV of molecular lines may be indicative of their sensitivity to non-LTE, and so should be confronted with 3D LTE and eventually non-LTE modelling.

**3.1.2. Oxygen and nickel.** Despite being the third most abundant element, O has few atomic lines forming in the photosphere that are strong enough and clean enough to be used as abundance diagnostics (Lambert 1978, Allende Prieto et al. 2001). The most useful lines are the low-excitation forbidden [O I] 630 nm line, and the high-excitation permitted O I 777 nm triplet. infrared transitions of the OH molecule is another alternative that has been

explored. Fig. 7 shows an overview of the evolution of the O abundance over the previous 40 years.

The [O I] 630 nm line couples to the ground state of neutral O, which has a dominant level population in the solar atmosphere and is not significantly perturbed by non-LTE effects. However, the line is strongly blended with a Ni I line, separated by only 0.003 nm, that first had its transition probability determined experimentally, with an uncertainty of 0.06 dex, by Johansson et al. (2003). Combined with the uncertainty of the solar Ni abundance, the strength of the blend is still fairly ill-constrained and its treatment impacts significantly on the O abundance. Studies that perform 3D LTE analyses and constrain the strength of the blend using the CLV have reported  $A(\text{O}) = 8.69 \pm 0.05$  based on Stagger (Allende Prieto et al. 2001) and  $A(\text{O}) = 8.73 \pm 0.02 \pm 0.05$  based on CO<sup>5</sup>BOLD (Caffau et al. 2015). Fixing the blend strength using the Ni abundance determined from unblended lines ( $A(\text{Ni}) = 6.20 \pm 0.04$ ), Asplund et al. (2021) finds  $A(\text{O}) = 8.70$ , with 0.02 dex variation between different solar intensity atlases. Bergemann et al. (2021) adopt a slighter higher Ni abundance based on meteorites ( $A(\text{Ni}) = 6.23 \pm 0.04$ ), but show that 3D non-LTE calculations significantly weaken the Ni blend, when employing the scaled Drawin formalism for hydrogen collisions, and finally arrive at  $A(\text{O}) = 8.77 \pm 0.05$ . However, using an improved version of the same model atom, Magg et al. (2022) later showed that Ni lines form close to LTE in the Sun. An even higher value,  $A(\text{O}) = 8.80 \pm 0.03$ , was recently reported by Cubas Armas et al. (2020), based on an LTE analysis with a semi-empirical model atmosphere and spatially resolved observations. To make further progress, the Ni abundance and 3D non-LTE Ni line formation of the Sun must be better constrained. Hydrogen collisions were recently published by Voronov et al. (2022), but tailored calculations of photo-ionisation cross-sections are still lacking. The Ni I-Ni II ionisation balance is not a reliable diagnostic in the Sun (Scott et al. 2015a), but the observed CLV-dependence of unblended Ni I lines can and should be challenged by new models to verify the magnitude of non-LTE effects.

The O I 777 nm triplet lines originate from the meta-stable level  $2p^3 3s^5 S_2^o$  at 9.15 eV. That the assumption of LTE line formation was inadequate to model these lines was realized already more than 50 years ago based on their observed CLV (Altrock 1968), pointing to an over-population of the lower level and sub-thermal line source functions. Further improvements in the model-fits to spatially resolved data were found with a combined 3D and non-LTE treatment by Kiseľman & Nordlund (1995) and several authors since. A milestone was reached following the work by Barklem (2018b), after which several studies could demonstrate that the CLV of the O triplet can be well reproduced by 3D non-LTE calculations without using the efficiency of hydrogen collisions as a free parameter. It is reassuring that they advocate abundances that agree to within 0.03 dex;  $8.69 \pm 0.03$  by Amarsi et al. (2018a) was renormalised to  $8.71 \pm 0.03$  with the new atomic data presented by Li et al. (2023b), compared to  $8.74 \pm 0.03$  by Bergemann et al. (2021) and  $8.73 \pm 0.03$  by Pietrow et al. (2023). The remaining difference may partly be attributed to the choice of observational data (Bergemann et al. 2021). It should also be noted that the O I 777 nm triplet lines are strongly sensitive to the rate of (de-)excitation by hydrogen collisions; these recent analyses are based on the asymptotic+free approach described in Amarsi et al. (2018a), but a more fundamental understanding of the relevant physics would be desirable (Sect. 2.2.3).

Amarsi et al. (2021) recently re-determined the 3D LTE solar O abundance from OH rovibrational transitions of OH ( $|\Delta\nu| = 1$ ) at around  $3 - 4 \mu\text{m}$ . The mean abundance  $A(\text{O}) = 8.70 \pm 0.04$  is in agreement with the atomic indicators. They are also in agreement

with the mean results from rotational ( $|\Delta\nu| = 0$ ) transitions in the far infrared ( $9 - 12\mu\text{m}$ ) as well as the weak first overtone lines ( $|\Delta\nu| \geq 1$ ) at  $1.5 - 1.7\mu\text{m}$ , although for these latter diagnostics there are noticeable trends in line-by-line abundances with excitation potential and line strength probably related to missing physics in the 3D RHD model at the shallow surface layers as well as uncertainties in the equivalent widths, respectively. Both the <3D> and the semi-empirical 1D [Holweger & Mueller \(1974\)](#) model (hereafter HM model) return higher abundances, due to their neglect of temperature inhomogeneities.

In summary, the recommended O abundance for the Sun has been revised downward by at least 0.1 dex in the 21st century (Fig. 7), thanks to the combination of several effects that coincidentally act in the same direction; in particular the recognition of the Ni blend in the [O I] 630 nm line, the use of non-LTE rather than LTE models for the O I 777 nm triplet and the use of 3D, rather than 1D, models for OH lines.

**3.1.3. Magnesium, silicon, and sulphur.** Full 3D non-LTE solar calculations have also recently been performed using high-quality model atoms for Mg and Si ([Amarsi & Asplund 2017](#), [Asplund et al. 2021](#)). Differences between 3D LTE and <3D> LTE, as well as their differences with LTE results from the HM model, are small for both elements, of order 0.01 dex ([Scott et al. 2015b](#), [Asplund et al. 2021](#)). The non-LTE effects for the selected lines in the solar disc-centre intensity are only  $\pm 0.01$  dex, which is (as expected) slightly smaller than that in the solar disc-integrated flux reported in 1D for Mg ([Lind et al. 2022](#)) and Si ([Mashonkina 2020](#)). We caution that more severe effects exist for other lines. Indeed, these latter sources report 1D non-LTE corrections that reach  $-0.1$  dex for both elements; and the 3D non-LTE versus 1D LTE correction for the 571 nm Mg I line is estimated to be 0.06 dex in the Sun ([Nissen et al. 2023](#)).

Despite this relatively weak modelling sensitivity, the solar Si abundance is debated: [Deshmukh et al. \(2022\)](#) report a value of  $7.57 \pm 0.04$  based on a 3D LTE analysis with a  $-0.01$  dex non-LTE correction applied from [Amarsi & Asplund \(2017\)](#), which is significantly higher than the  $7.51 \pm 0.03$  reported by [Asplund et al. \(2021\)](#), mainly as a consequence of the choice of oscillator strengths and line fitting technique. An even higher value but with a large scatter was found by [Magg et al. \(2022\)](#),  $7.59 \pm 0.07$ , based on a <3D> non-LTE analysis of the solar disc-integrated flux. For Mg, there is a greater consensus between groups, with several recent 3D ([Asplund et al. 2021](#)), <3D> ([Bergemann et al. 2017a](#)), and 1D ([Alexeeva et al. 2018](#)) non-LTE values in the range  $7.54 - 7.57$ . However, this agreement is partly coincidental as different model atmospheres and Mg I lines were used. For example, limiting the comparison to 1D MARCS calculations for the same four Mg II lines, with almost identical gf-values, the average difference between [Alexeeva et al. \(2018\)](#) and [Asplund et al. \(2021\)](#) is 0.17 dex in LTE and 0.09 dex in non-LTE. Part of the reason may be the use of disc-integrated flux in the former study and the disc centre intensity in the latter study, but in general, caution is advised for abundance determination using Mg II lines because of the unconstrained hydrogen collisional cross-section and the large sensitivity of this majority species on the electron number density ([Asplund et al. 2021](#)). Since the Mg and Si abundances are very close in absolute numbers, the Mg/Si ratio in the solar photosphere cannot yet be definitely established to be above or below unity, which is important in the context of exoplanet mineralogy (Sect. 3.4).

The solar abundance of S has not yet been calculated using consistent 3D non-LTE calculations. Indeed, no study has even determined the 1D non-LTE abundance of this important refractory element using recently published hydrogen collisional cross-sections

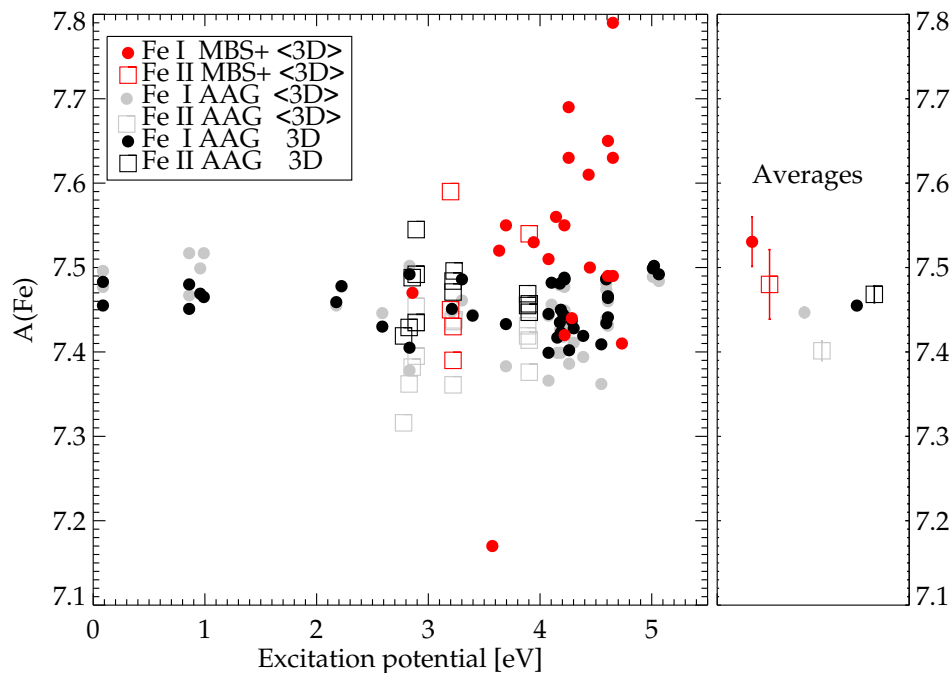


**Figure 8:** The left-hand panel compares the Fe line abundance results of [Magg et al. \(2022, MBS+\)](#) and [Asplund et al. \(2021, AAG\)](#). All abundances have been computed in non-LTE. Simple averages and standard errors are shown in the right-hand panel. The recommended Fe abundances are  $A(\text{Fe}) = 7.51 \pm 0.06$  (MBS+) and  $A(\text{Fe}) = 7.46 \pm 0.04$  (AAG).

([Belyaev & Voronov 2020](#)). This is of high priority, in particular considering the known non-LTE sensitivity of the near-infrared S I triplet (e.g. [Takeda et al. 2005](#)).

**3.1.4. Iron.** A high-resolution optical and near-infrared solar atlas can resolve thousands of Fe I lines and at least a hundred Fe II lines, allowing a critical selection of lines based on blending properties and atomic data quality. Fe lines thereby allow powerful diagnostic tests to support claims of preferred Fe abundance for our star; consistent abundances should be determined from different lines regardless of their excitation potential, ionisation stage, line strength, central wavelength, viewing angle, and so on.

It is well known that the neutral Fe atom is over-ionized compared to LTE in the solar atmosphere, an effect that is boosted by over-excitation of the lowest levels (e.g. [Lind et al. 2012](#)). [Mashonkina et al. \(2011\)](#) emphasized the need for non-LTE studies to include highly excited theoretically predicted levels of neutral Fe in the atom (see Fig. 3), to achieve realistic coupling to the next ionisation stage and remove the need for artificial thermalization of the upper levels (e.g. [Gehren et al. 2001](#)). Nevertheless, prior to the arrival of asymptotic model calculations of collisional cross-sections for excitation and charge transfer with neutral hydrogen ([Barklem 2018a](#)), model atoms had to be astrophysically calibrated. Using either the Drawin formula with  $S_{\text{H}}$  between 0.1 and 1.0 or the rates from [Barklem \(2018a\)](#), perhaps



combined with those computed with the recipe of [Kaulakys \(1991\)](#), recent work in 1D and 3D agree that the average non-LTE impact on Fe I lines in the Sun is positive and of order 0.01 – 0.03 dex (e.g. [Mashonkina et al. 2011](#), [Bergemann et al. 2012](#), [Scott et al. 2015a](#), [Sitnova et al. 2015](#), [Lind et al. 2017](#), [Asplund et al. 2021](#)), with effects for individual lines ranging from slightly negative to at most +0.1 dex, depending on the atmosphere and the model atom. In the Sun, the non-LTE effect on Fe II lines is consistently reported to be less than 0.01 dex in both 1D and 3D ([Lind et al. 2012, 2017](#), [Amarsi et al. 2022](#)).

The first quantitative determination of the solar Fe abundance using a high-resolution 3D simulation ( $200 \times 200 \times 82$  meshsize) was published by [Asplund et al. \(2000b\)](#). The average value determined from Fe II lines using 3D RHD models and 3D LTE or non-LTE radiative transfer have since then varied in the range 7.45 – 7.53 ([Asplund et al. 2000b](#), [Caffau et al. 2011c](#), [Scott et al. 2015a](#), [Asplund et al. 2021](#)), which is 0.04 – 0.1 dex higher than theoretical 1D models and 0.04 – 0.07 dex higher than corresponding <3D> models (e.g. [Bergemann et al. 2012](#), [Asplund et al. 2021](#)). As seen in [Fig. 6](#), the weakening of synthetic Fe II lines in 3D reflects both on the shallower mean temperature stratification of 3D RHD models compared to 1D models in line-forming regions and on the effect of granulation and temperature inhomogeneities.

Consistent 3D non-LTE calculations for Fe using realistic model atoms have only recently become possible (see [Sect. 2.2.4](#)). [Lind et al. \(2017\)](#) determined the solar abundance using both Fe I and Fe II lines with the result  $7.48 \pm 0.04$  dex, which was later improved further by [Asplund et al. \(2021\)](#) to  $7.46 \pm 0.04$  dex. In these studies, it is shown that 3D RHD modelling outperforms <3D> and 1D modelling in reproducing the CLV of Fe lines (also demonstrated in LTE by [Pereira et al. 2009a](#)) and the excitation and ionisation balance of Fe ([Fig. 8](#)). However, earlier studies (e.g. [Mashonkina et al. 2011](#), [Bergemann et al. 2012](#)), have demonstrated that excellent excitation and ionisation balance is also achievable with 1D and <3D> models, which reflects the large influence that line selection and fitting, treatment of blends, as well as the choice of atomic data, have on such conclusions. [Fig. 8](#) compares the Fe I and Fe II non-LTE line-by-line abundances inferred using 3D and <3D> models by [Asplund et al. \(2021\)](#), and using an <3D> model by [Magg et al. \(2022\)](#). The line selection is very different, only four lines overlap, but they have a systematic offset (0.07 dex) that is representative of the difference between the recommended Fe abundances. The upward skew in the latter results may reflect the influence of blends or treatment of microturbulence. We note that excitation balance cannot be verified by the [Magg et al. \(2022\)](#) selection and the substantial scatter in the data (0.12 dex standard deviation) prevents conclusions on a satisfactory ionisation balance to better than 0.04 dex precision.

**3.1.5. Recommendations.** In summary, solar 3D non-LTE abundance determinations have been performed for Li, C, N, O, Na, Mg, Al, Si, K, Ca, Fe and Ba (e.g. [Asplund et al. 2021](#), and references therein) as well as Mn ([Bergemann et al. 2019](#)). We argue that 3D LTE modelling for molecules and 3D non-LTE modelling from atoms can result in consistent abundances for available abundance diagnostics without empirical tuning, for the elements for which this has been tested, with the exception of N. Nevertheless, discrepancies between recommended abundances from different studies can be up to 0.1 dex: importantly, these are likely not caused by the choice of 3D atmosphere or model atom. Instead, they can often, but not always, be attributed to differences in line selection and fitting, consideration of blends, source of oscillator strengths for diagnostic lines, and choice of observational data. As solar interior models improve in sophistication (e.g. [Christensen-Dalsgaard 2021](#), and references



therein), abundance and opacity changes of only a few percent can significantly alter our understanding of the solar modelling problem, hence a stronger consensus is desirable. We list general and element-specific advice in bullet-point form below.

Simply raising the solar metallicity does not resolve all facets of the solar modelling problem: as well as the sound speed profile, the observed neutrino fluxes and the Li depletion relative to meteorites need to be consistently explained (Buldgen et al. 2023a). Neutrino fluxes are sensitive to the assumed model metallicity, but measurements of observed fluxes from the CNO cycle are not yet precise enough to provide strong constraints (Borexino Collaboration et al. 2018). In connection to these issues, it is interesting to consider the radiative opacities below the base of the convection zone (Bailey et al. 2015, Pradhan 2023), pebble-accretion in the pre-main sequence phase (Kunitomo et al. 2022), as well as macroscopic transport (Eggenberger et al. 2022). As demonstrated by Buldgen et al. (2023b), helioseismic inversions of the adiabatic exponent in the convective envelope, independent of the opacities in the radiative interior, in fact favour a low metal mass fraction that is in line with Asplund et al. (2021). This underlines the need for further theoretical and experimental work before strong conclusions about the origins of the solar modelling problem can be drawn; it seems improbable, however, that the discrepancies can be resolved simply by adjusting the abundances alone. Our recommendations to make further progress on the solar debate from a stellar-atmosphere theory perspective are as follows:

- 3D non-LTE modelling for S, Ni, and CNO-bearing molecules should be performed.
- Model validation using the observed CLV is desirable for more spectral lines, for example using the data presented in Ellwarth et al. (2023).
- The impact on the 3D model atmosphere from abundance changes (Zhou et al. 2023) or RMHD simulations should be further investigated (e.g. Shchukina & Trujillo Bueno 2015, Shchukina et al. 2016).
- There is still a need for higher quality atomic data, for example concerning inelastic hydrogen collisions for Mg II, photoionisation cross-sections for Ni I, and oscillator strengths for diagnostic lines of Fe II.
- Further theoretical and experimental studies into the physics of inelastic hydrogen collisions, for example with the DESIREE experiment (Barklem et al. 2021, Grumer et al. 2022) are necessary.

## 3.2. Stellar parameters

Before turning to abundance analyses for stars other than the Sun in Sect. 3.3 and 3.4, we shall discuss stellar-parameter determination using 3D RHD models and non-LTE calculations. As elaborated on below, spectroscopic stellar parameters inferred from Balmer lines and excitation/ionisation-balance of Fe are indeed model dependent. However, the improved models show great promise to overcome systematic uncertainties and allow the community to fully leverage the reddening-independence and the high precision that is technically achievable with spectroscopy. Throughout this section and next, we refer to Fig. 9 that shows examples of how 1D LTE, 1D non-LTE, 3D LTE, and 3D non-LTE lines profiles may differ for a very metal-poor dwarf star.

**3.2.1. Balmer lines.** The Balmer lines are prominent in optical spectra of solar-type stars; H $\alpha$  in particular, situated as it is in a relatively line-free region, is often used to determine stellar  $T_{\text{eff}}$ . In the era of large surveys, the large data volumes necessitate parameter

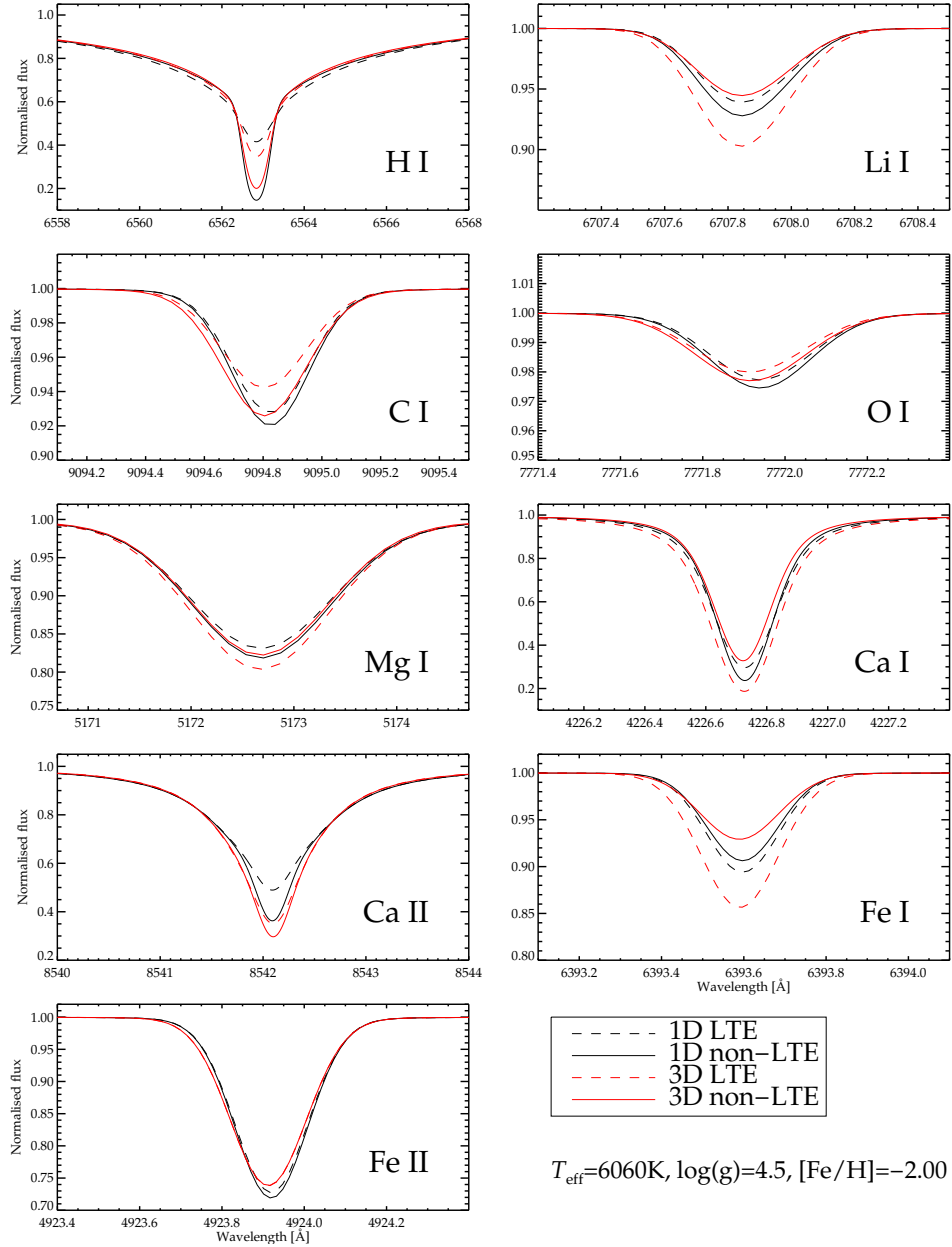


**Figure 9:** Synthetic line profiles computed under different assumptions for a metal-poor dwarf star, with stellar parameters as indicated to the bottom right. The figure has been produced from the calculations by Amarsi et al. (2018b, HI), Wang et al. (2021, Li I), Amarsi et al. (2019c, CI and OI), Matsuno et al. (2024, Mg I), Lind et al. (2013, Ca), and Amarsi et al. (2022, Fe).

optimization via data-driven methods, in which the observed flux in every (unmasked) pixel contributes to maximize precision. This ought to give the very broad Balmer lines a large influence on the  $T_{\text{eff}}$  determination, in particular at low metallicity, where there are fewer metal lines with competing influence. However, these lines are prone to uncertainties in the continuum definition (e.g. [Barklem et al. 2002](#)).

Despite the inherent freedom to tune the parameters of the mixing length theory, most importantly the mixing length  $\alpha$ , 1D models struggle to reproduce the Balmer line profiles predicted by 3D RHD models. The outer wings form deep in the atmosphere and are often stronger in 3D than in 1D, due to the steeper temperature gradients of the hot upflows in this region, while the inner wings of strong Balmer lines can experience the reversed situation at shallower depths ([Amarsi et al. 2018b](#), [Bertran de Lis et al. 2022](#)). The final influence on  $T_{\text{eff}}$  thus depends critically on the choice of line, fitting method, and mixing length, and 1D models errors can reach up to 300 K ([Ludwig et al. 2009a](#)). To disentangle the influence of atmospheric inhomogeneities with the difference in average atmospheric structures in 1D and 3D LTE, [Ludwig et al. \(2009a\)](#) also computed  $\langle 3D \rangle$  Balmer line profiles. Interestingly, they find that the full 3D profiles, including the effects of granulation, are substantially different from  $\langle 3D \rangle$  in many cases. Even the sign of the temperature correction found for 3D–1D can differ from  $\langle 3D \rangle$ –1D, e.g.,  $-65$  K and  $+106$  K, respectively, for  $H\beta$  in a very metal-poor turn-off star ( $\alpha = 1.0$ ). [Giribaldi et al. \(2019\)](#) proposed an empirical  $[\text{Fe}/\text{H}]$ -dependent positive correction to  $H\alpha$ - $T_{\text{eff}}$  inferred from 1D models of dwarfs and subgiants, equal to 28 K at  $[\text{Fe}/\text{H}] = 0$  and 139 K at  $[\text{Fe}/\text{H}] = -0.7$ . They find good qualitative agreement of this trend with expected 3D–1D effects, and conclude that 3D models are superior in this respect.

[Amarsi et al. \(2018b\)](#) investigated 3D non-LTE line formation of Balmer lines over a large grid of atmospheres. They find photon pumping by  $\text{Ly}\alpha$  to be an important non-LTE effect, over-populating the first excited state of neutral hydrogen, which is the lower level of the Balmer series. In combination with several other influential bound-bound and bound-free transitions among highly excited levels, the non-LTE effect can reach  $\pm 100$  K for the  $H\alpha$  line wings; the non-LTE effects are more muted for the wings of  $H\beta$  and  $H\gamma$  that form deeper in the atmosphere. For metal-poor turn-off stars, 3D and non-LTE effects act in the same direction and 1D LTE models of  $H\alpha$  underestimates  $T_{\text{eff}}$  by 150 K for typical choices of mixing length parameters (see [Fig. 9](#)). For the Sun, 3D non-LTE modelling of  $H\alpha$ ,  $H\beta$  and  $H\gamma$  returns  $T_{\text{eff}}$ -values that are hotter than 1D models, but still slightly too low at 5709–5722 K ([Amarsi et al. 2018b](#)), which [Giribaldi et al. \(2021\)](#) suggest is caused by a small normalisation distortion in the adopted solar atlas ([Giribaldi et al. 2019](#)).  $\langle 3D \rangle$  models cannot well reproduce the 3D line profiles in the Sun, either in LTE ([Ludwig et al. 2009a](#)) or non-LTE ([Pereira et al. 2013](#)). [Giribaldi et al. \(2023\)](#) find excellent agreement within  $\pm 46$  K between 3D non-LTE  $H\alpha$ -temperatures, using the synthetic profiles by [Amarsi et al. \(2018b\)](#), and the infrared flux method for an extended sample of metal-poor and metal-rich stars, including red giants.

The central  $\pm 0.1$  nm has the largest  $T_{\text{eff}}$  and non-LTE sensitivity, but the Balmer line cores are poorly reproduced by both 1D and 3D photospheric models, because of the chromospheric influence (e.g. [Leenaarts et al. 2012](#)), necessitating RMHD models including non-equilibrium hydrogen ionisation. [Bergemann et al. \(2016\)](#) found empirical correlations between the width of the  $H\alpha$  line core in red giants and other fundamental stellar parameters;  $[\text{Fe}/\text{H}]$ ,  $\log g$  and, interestingly, stellar mass. However, in the lack of RMHD chromospheric simulations for such stars, the authors forego speculation about the un-

derlying cause of the observed correlations. The first RHD model of a late-type giant (Aldebaran,  $T_{\text{eff}}/\log g/[\text{Fe}/\text{H}] = 4000/1.5/0.0$ ) that extends to the chromosphere was computed by [Wedemeyer et al. \(2017\)](#), revealing a dynamic and shock-heated layer above the photosphere. However, they show that the 3D non-LTE line profile of  $\text{H}\alpha$  is still far too narrow to reproduce the observed core width, which could be due to missing physics in the model atmosphere itself, not least magnetic fields.

**3.2.2. Fe lines.** A common method to determine stellar parameters spectroscopically is to exploit the excitation equilibrium of the numerous Fe I lines present in late-type spectra and the ionisation equilibrium of Fe I and Fe II lines. However, 1D LTE spectroscopic parameters are known to underestimate both  $T_{\text{eff}}$  and  $\log g$  for metal-poor stars (e.g. [Frebel et al. 2013](#), and references therein). The determination of  $\log g$  has seen significant improvement with 1D non-LTE calculations (e.g. [Korn et al. 2003](#), [Mashonkina et al. 2023](#)), which capture the over-ionisation of Fe I and raise the Fe abundances determined from these lines, while non-LTE effects on Fe II lines are negligible. [Lind et al. \(2012\)](#) illustrate how the effect on  $\log g$  varies over the FGK star parameter space, and can exceed 1 dex for hot, metal-poor giants. However,  $T_{\text{eff}}$  inferred from the excitation balance of Fe I lines tend to be even lower than in LTE in metal-poor stars, as a consequence of the erroneous temperature stratification and neglect of inhomogeneities. 1D non-LTE studies have attempted to mitigate this problem by excluding the lines with lowest excitation potential ([Li & Ezzeddine 2023](#)) or by combining photometric  $T_{\text{eff}}$  with spectroscopic  $\log g$  ([Ruchti et al. 2013](#)). As shown by [Serenelli et al. \(2013\)](#), the model-dependence of  $T_{\text{eff}}$  and  $\log g$  furthermore leads to severely underestimated ages and overestimated masses and distances from 1D LTE analyses.

Since the first 3D LTE analysis studies of Fe II lines, it has been known that the impact on Fe abundances is significant and can be both positive and negative, depending on line properties and stellar parameters (e.g. [Allende Prieto et al. 2002](#), [Nissen et al. 2004](#), [Korn et al. 2007](#)). Weak Fe II lines are typically affected by  $\pm 0.1$  dex, as shown for red giants using fictitious lines ([Collet et al. 2007](#), [Hayek et al. 2011](#), [Dobrovolskas et al. 2013](#)). This behaviour was later confirmed for both dwarfs and giants using real lines ([Amarsi et al. 2019c](#)), while saturated lines have larger corrections that also can be both positive and negative. Significant impact is not only seen for low-metallicity stars, but a turn-off star like Procyon is affected by of order  $+0.1$  dex ([Allende Prieto et al. 2002](#), [Amarsi et al. 2022](#)). The LTE assumption for Fe II line formation in 3D models has been shown to be accurate within  $\sim 0.02$  dex for  $[\text{Fe}/\text{H}] > -2.5$ , but non-LTE effects reach  $\sim +0.1$  dex for extremely metal-poor turn-off stars ([Amarsi et al. 2016b, 2022](#)) and thereby exacerbate the difference with respect to 1D LTE in such stars.

Fe I lines are affected by both 3D and non-LTE effects that can act in the same or opposite directions, emphasizing the need for consistent modelling, in particular when non-LTE effects are large ([Shchukina et al. 2005](#), [Amarsi et al. 2016b](#), [Nordlander et al. 2017](#), [Lind et al. 2017](#), [Amarsi et al. 2022](#), [Lagae et al. 2023](#)). The combined impact on average metallicities is of order  $+0.3$  dex for very/extremely metal-poor turn-off stars ([Amarsi et al. 2016b, 2022](#)), increasing to  $+0.5$  dex at  $[\text{Fe}/\text{H}] < -4$  ([Lagae et al. 2023](#)). A slightly smaller  $+0.2$  dex effect was reported for the red giant HD122563 ([Amarsi et al. 2016b](#)), but caution is advised given the significant ionisation imbalance remaining in 3D non-LTE, which is expected to improve with an updated 3D model that use the  $-0.2$  dex revision of the parallax-constrained  $\log g$  ([Karovicova et al. 2018](#)). The upper limit to  $[\text{Fe}/\text{H}]$  for the most Fe-poor star known, also a red giant, was raised by  $+0.8$  dex ([Nordlander et al. 2017](#)).

In the most recent 3D non-LTE study by Amarsi et al. (2022), it is seen that Fe I lines of low and high excitation are differently impacted, such that the abundance slope with excitation potential increases and flattens the negative gradients seen for the benchmark metal-poor stars HD84937 and HD140283 in 1D LTE. The effect corresponds to a  $T_{\text{eff}}$ -change of 250 – 300K and reflects on the complex and coupled 3D non-LTE mechanisms. The low excitation lines of Fe I, when the species is in minority, are the most sensitive to the steeper temperature stratification and inhomogeneities that strengthen the lines (Collet et al. 2007, Dobrovolskas et al. 2013, Gallagher et al. 2015), but they are also most affected by non-LTE effects in 3D models that weaken them (Amarsi et al. 2016b). The high-excitation Fe I lines have a behaviour that is more similar to Fe II lines.

The full impact of 3D non-LTE modelling on stellar parameters can be exemplified with G64-12, an extremely metal-poor dwarf/turn-off star used as benchmark star in many studies. Fe line formation in 3D non-LTE (Amarsi et al. 2016b) gives approximately  $T_{\text{eff}} = 6450$  K,  $\log g = 4.3$  and  $[\text{Fe}/\text{H}] = -3.0$ , in line with the infrared flux method  $T_{\text{eff}} = 6463$  K (Meléndez et al. 2010), while 1D LTE spectroscopic analysis returns  $T_{\text{eff}} = 6100$  K,  $\log g = 3.9$  and  $[\text{Fe}/\text{H}] = -3.6$  (Snedden et al. 2023); i.e., a 0.6 dex error in  $[\text{Fe}/\text{H}]$ .

**3.2.3. Photometry.** The impact of 3D RHD models on photometric colours have been investigated by Chiavassa et al. (2018) using the *Stagger*-grid (with grids of spectra available via the POLLUX database: Palacios et al. 2010), and Kučinskas et al. (2018) and Bonifacio et al. (2018a) using the *CIFIST*-grid. Some degree of sensitivity of continuum fluxes to granulation is in fact expected simply from the non-linear temperature-dependence of the Planck function, with cooler models and shorter wavelengths being most affected (see Appendix A in Kučinskas et al. 2018). The *CIFIST* results show that 1D narrow-band colours, such as  $g - z$ , can underestimate  $T_{\text{eff}}$  by up to 200 K for the hot end of the grid, with a smaller effect in the opposite direction seen for the cooler end. Excluding UV-centered bands, the maximum effect on the investigated colours is small, but non-negligible at  $\pm 0.03$  mag. However, as cautioned by the authors, the treatment of scattering as true absorption in the *CIFIST*-grid may overestimate the effect.

### 3.3. Origin of the elements

Stars act as cosmic element factories, forging elements through nuclear reactions, and redistributing them into the universe through powerful winds and explosions. The ongoing cycle of stellar birth, evolution, and death enriches the cosmos with heavy elements and provides the raw materials for new stars and planets. The observed element abundances in stars in our Galaxy serve to constrain the ingredients of this process, e.g., the star formation history, the hierarchical assembly of the Galaxy, and the mass-dependent yields of stars, and allow us to validate and calibrate models of Galactic chemical evolution. In the newborn and metal-poor universe, massive stars were the main producers of new elements, forged either during hydrostatic burning or in core-collapse supernovae (SNe) and hypernovae (HNe) explosions that return the elements to the interstellar medium. We focus mainly on the metallicity regime  $-4 < [\text{Fe}/\text{H}] < -1$ , in which the chemical pattern of Galactic stars reflect on the initial mass function of star formation and the yields from an accumulated large number of events, rather than the stochastic effects of individual explosions. The limit in metallicity where chemical enrichment from delayed sources, such as AGB stars and thermonuclear supernovae (SNIa), becomes noticeable is element and model-dependent, e.g.,

$[\text{Fe}/\text{H}] \gtrsim -2.5$  for N, but  $[\text{Fe}/\text{H}] \gtrsim -1$  for  $\alpha$ -elements (e.g. Kobayashi et al. 2020).

We limit the discussion to the origin of Li, C, N, O,  $\alpha$ -elements, Fe-peak elements, and the neutron-capture element Ba, in the light of 3D non-LTE calculations. The main focus on metal-poor stars is a reflection on the larger modelling errors that are often associated with their 1D LTE abundances: reduced UV line blocking leads to amplification of non-LTE effects, and there are also larger differences between the 1D and 3D temperature stratifications at lower metallicities (Sect. 2.5). The use of the Sun as reference star to cancel systematic errors also works less well compared to the solar-metallicity regime, thus making the need for realistic stellar atmosphere and line formation modelling all the greater.

**3.3.1. Lithium.** More than two decades ago, Li was the first element targeted with 3D non-LTE modelling in a metal-poor dwarf and subgiant (Asplund et al. 2003). It is also the first element for which a grid of 17 models was produced for such stars (Sbordone et al. 2010), a number that has today grown to cover 70 CO<sup>5</sup>BOLD models (Mott et al. 2020) and 195 Stagger models for metal-poor and metal-rich dwarfs and giants (Wang et al. 2021). This astonishing progress is partly a consequence of the simple term structure of this alkali element, making grid computations numerically feasible, and the reliability of the atomic data in particular with full quantum mechanical data for the inelastic hydrogen collisions (Barklem et al. 2003), which help justify carrying out expensive 3D non-LTE calculations. It also of course reflects on the great astrophysical interest in Li. The Big Bang origin of the dominant isotope <sup>7</sup>Li, combined with both production and depletion by stars and stellar environments give rise to a complex abundance pattern that is correlated with stellar, and possibly planetary, parameters, but also involves Li-rich and Li-poor outliers (see, e.g., review by Randich & Magrini 2021).

The non-LTE line formation of the resonant Li I 670.7 nm line follows a simple pattern: when the line is weak, the corrections are small and depend mainly on the photoionisation/photorecombination balance, while at larger line strength, significant photon losses cause increasingly negative corrections until the point of maximum saturation. Wang et al. (2021) uncovered an important systematic error affecting all previous work that has neglected background line opacity for bound-bound transitions (e.g. Lind et al. 2009, Mott et al. 2020). If blending metal lines are not included in the calculation of radiative bound-bound rates, UV Li I lines cause significant photon pumping, which leads to non-LTE corrections that are too positive or not sufficiently negative by up to +0.15 dex for a test case. For giants and cool dwarfs around  $[\text{Fe}/\text{H}] = -2$ , the assumption of 1D non-LTE is often accurate to within  $\pm 0.03$  dex, while cancellation of 3D and non-LTE effects coincidentally lead to similarly accurate 1D LTE results for warm dwarfs and TO stars (see Fig. 9). However, we caution that these comparisons depend on both metallicity and Li abundance, as well as the microturbulence adopted for the 1D analysis.

Wang et al. (2021) analyse how their 3D non-LTE results impact particularly important Li abundance measurements. The Spite plateau of unevolved metal-poor stars experiences a small decrease ( $-0.03$  dex) compared to 1D LTE at  $[\text{Fe}/\text{H}] = -2$ . At  $[\text{Fe}/\text{H}] = -3$ , corrections are close to zero, while they revert sign and reach +0.1 dex at  $[\text{Fe}/\text{H}] = -4$ . This has a flattening effect on the plateau but likely not sufficiently large to completely erase the positive slope with increasing metallicity (see e.g. Norris et al. 2023), which instead should be understood in the context of atomic diffusion and internal mixing. Similar conclusions on the robustness of the Spite plateau were drawn by Mott et al. (2020). Recently, Gao et al. (2020) uncovered a systematic 0.4 dex difference in 1D non-LTE Li abundance between

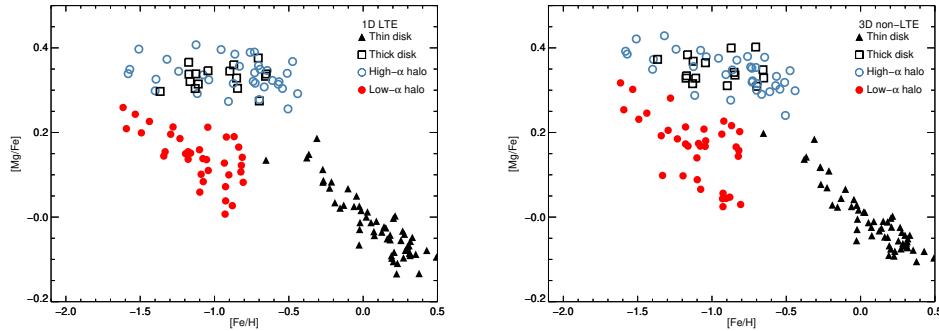


**Figure 10:** The  $[\text{Mg}/\text{Fe}]$  ratios of different Galactic populations obtained from 1D LTE (left) and 3D non-LTE (right) analysis. Two separate tracks are uncovered in the low- $\alpha$  halo from the more accurate abundances displayed in the right-hand panel, implying that two separate accretion events have taken place (Nissen et al. 2023, Matsuno et al. 2024).

stars on the hot and cool sides of the so called Li dip that is centered on  $T_{\text{eff}} = 6500$  K on the main sequence, suggesting that the cool stars have indeed undergone depletion by approximately this amount. Due to the similarity in stellar parameters, the relative difference is not expected to change significantly in 3D non-LTE, but the absolute plateau levels may experience a slight increase. As discussed by Wang et al. (2021), the effect on the RGB stars is more severe, reducing Li abundances on the lower RGB compared to 1D LTE by approximately  $-0.15$  dex at  $[\text{Fe}/\text{H}] = -2$ . When corrected for the large dilution caused by the first dredge-up, the initial Li abundances are broadly in agreement with the canonical Spite plateau. In Li-rich giants, the 670.7 nm line can be very strong, and abundance corrections have been shown to reach  $-0.6$  dex; clearly these are important to implement to understand the underlying cause of the enrichment (e.g. Kowkabay et al. 2022).

Several studies have shown that the  ${}^6\text{Li}/{}^7\text{Li}$  isotopic ratio can be constrained from the shape of the 670.7 nm line in high-resolution spectra and several significant detections at a level of 5% were reported for stars on the Spite plateau at  $-3 < [\text{Fe}/\text{H}] < -1$  (e.g. Asplund et al. 2006, and references therein). However, any significant detection of the lighter isotope in unevolved very metal-poor stars is difficult to reconcile with a standard Big Bang nucleosynthesis scenario, in particular when simultaneously considering stellar depletion of this element, prior to and during the main sequence. Cayrel et al. (2007) demonstrated how the impact of convective motions on the line profile shape is degenerate with the amount of  ${}^6\text{Li}$ , in LTE as well as non-LTE. A reappraisal of the Li isotopic ratios in halo stars with 3D non-LTE calculations were later performed by Lind et al. (2013) and Wang et al. (2022), transforming previous detections to upper limits at  $< 2\%$ , thereby removing the tension with the cosmological predictions. As shown, for example, by Mott et al. (2017), non-LTE modelling in both 1D and 3D can still lead to significant detection of the lighter isotope in a solar-metallicity subgiant, suggesting a connection to planet engulfment or stellar activity.

**3.3.2. Carbon and  $\alpha$ -element abundances from atomic lines.** The so called  $\alpha$ -elements, O, Mg, Si, S, and Ca, are over-produced with respect to Fe by core-collapse SNe and HNe, while



their building block C is less so. However, the abundance patterns predicted by Galactic chemical evolution models have many uncertainties. First, the  $[\alpha/\text{Fe}]$ -ratios in metal-poor stars are affected (0.1–0.5 dex for  $[\text{O}/\text{Fe}]$ ) by assumptions made for the mass range of failed SNe, for which the entire CO-core fall back onto the black hole, and the upper mass limit of HNe (Romano et al. 2010, Kobayashi et al. 2020). Secondly, the assumed fraction of HNe affects the tilt of the  $[\alpha/\text{Fe}]$  trends with metallicity before the onset of SNIa, which can be either steep ( $\sim 0.6$  dex decline over  $-4 < [\text{Fe}/\text{H}] < -1$ ) in the absence of HNe or shallow, almost flat, if all stars  $M > 20M_{\odot}$  explode as HNe (Romano et al. 2010). Thirdly, mixing and fallback of HNe also influences yields (Umeda & Nomoto 2002), but is treated as a free parameter. Ratios between alpha elements are much less sensitive to the mass ranges, but can, e.g., be affected by changes in the  $^{12}\text{C}(\alpha, \gamma)^{16}\text{O}$  nuclear reaction rate.

The metallicity range  $[\text{Fe}/\text{H}] > -3.5$  can be probed by atomic C and O lines, for which both 3D and non-LTE effects have been investigated. 1D non-LTE effects for the highly excited allowed transitions are slightly negative in this metallicity regime for unevolved stars, of order  $-0.1$  dex (Zhao et al. 2016, Amarsi et al. 2019b), placing the  $[\text{O}/\text{Fe}]$  values at  $\sim 0.6 - 0.7$  and the  $[\text{C}/\text{Fe}]$  values at  $\sim 0.1 - 0.2$ . Consistent 3D non-LTE calculations have not dramatically altered the picture, but cause a further decrease of order  $0.05 - 0.1$  dex for both elements (Amarsi et al. 2019b, Hansen et al. 2020) and display a slight increasing trend towards lower metallicity, in reasonable agreement with the predictions by Kobayashi et al. (2020) that are based on an assumed HNe fraction of 0.5 at low metallicity. Cayrel et al. (2004) reported a similar mean  $[\text{O}/\text{Fe}]$  value for extremely metal-poor giants based on 1D LTE analysis of the 630 nm line. The authors estimate a  $-0.23$  dex correction for 3D effects, following Nissen et al. (2002), but more recent work have shown that 3D corrections to  $[\text{O I}]$  line abundances are in fact very small in extremely metal-poor giants (Dobrovolskas et al. 2015, Collet et al. 2018). Importantly, the trend of the  $[\text{C}/\text{O}]$  ratio with metallicity is constant at  $-0.6$  in 3D non-LTE (Amarsi et al. 2019c), in agreement with, e.g., Kobayashi et al. (2020). In contrast, in 1D LTE  $[\text{C}/\text{O}]$  shows a striking upturn towards low metallicity. This was previously interpreted as a possible signature of Pop III stars (Akerman et al. 2004), or of rapid rotation in low-metallicity massive stars (Chiappini et al. 2006); although more recent GCE models including rotation by Prantzos et al. (2018) suggest that while there is a small positive effect on the absolute C and O levels, rotation does not strongly impact the tilt of the  $[\text{C}/\text{O}]$  ratio.

Several recent studies place the  $[\text{Mg}/\text{Fe}]$  plateau in very metal-poor Milky Way stars around  $\sim 0.3$  in 1D non-LTE, which is considerably lower than  $[\text{O}/\text{Fe}]$  (Zhao et al. 2016, Bergemann et al. 2017b, Mashonkina et al. 2017, Amarsi et al. 2020b, Hansen et al. 2020). Non-LTE effects are typically minor for Mg, but become increasingly positive with decreasing metallicity for unsaturated lines, and increasingly negative with line strength until saturation (e.g. Osorio & Barklem 2016). The large positive (0.3–0.4 dex) non-LTE effects predicted for extremely metal-poor turn-off stars by Andrievsky et al. (2010), which would raise  $[\text{Mg}/\text{Fe}]$  to 0.6, are not confirmed by later works. However, the same studies that predict smaller non-LTE corrections have also revealed an ionisation imbalance of 0.2 dex in the sense that Mg II lines give higher abundances than Mg I for metal-poor unevolved stars (Alexeeva et al. 2018, Lind et al. 2022).

Sample 3D non-LTE calculations were performed for a mildly metal-poor dwarf and very metal-poor giant model by Bergemann et al. (2017a) with the result that Mg abundances based on Mg I lines can be both higher and lower in 3D non-LTE compared to 1D non-LTE, largely dependent on the microturbulence. Recently, Nissen et al. (2023) used a grid of



3D–1D non-LTE corrections for the Mg I 571.1 nm in dwarfs (Matsumo et al. 2024), with differential abundance corrections of  $-0.03$  dex for the coolest stars to  $+0.06$  dex in the warmest, most metal-poor stars around  $[\text{Fe}/\text{H}] = -1.5$ , on top of a solar correction of  $+0.06$  dex. Thus, Nissen et al. (2023) demonstrate the first 3D non-LTE Mg abundances for a large sample of stars, in this case halo dwarfs. Combined with 3D LTE Fe II-based Fe abundances (Amarsi et al. 2019c), the  $[\text{Mg}/\text{Fe}]$ -ratio is reported to be stable around  $\sim 0.3$ , but split between slightly higher and lower values in two halo populations with different chemical enrichment histories (Fig. 10). The 3D non-LTE  $[\text{O}/\text{Mg}]$ -values are not affected by this bimodality, but are uniformly centered on  $\sim 0.2$ , in good agreement with the predictions by Kobayashi et al. (2020). At even lower metallicities, tailored studies of two ultra metal-poor stars have shown that 3D non-LTE Mg abundances are  $0.3 - 0.5$  dex higher than 1D LTE, and  $0.1 - 0.2$  dex higher than 1D and  $\langle 3\text{D} \rangle$  non-LTE for a dwarf and a giant (Nordlander et al. 2017, Lagae et al. 2023). However, the corresponding effect on Fe is even larger (Sect. 3.2.2), and  $[\text{Mg}/\text{Fe}]$  is therefore effectively reduced.

The  $[\text{Ca}/\text{Fe}]$  plateau in very metal-poor stars is at a very similar level to Mg in 1D non-LTE in the Milky Way, i.e., at approximately  $\sim 0.3 - 0.4$ , including similar corrections to neutral lines in 1D (e.g. Zhao et al. 2016, Mashonkina et al. 2017, Sitnova et al. 2019, Amarsi et al. 2020b, Hansen et al. 2020). A 3D non-LTE investigation was made by Lind et al. (2013) for four unevolved stars in the range  $-3.5 < [\text{Fe}/\text{H}] < -2$ , indicating that 3D non-LTE abundances are higher than 1D non-LTE by  $0.2$  dex for the neutral resonance  $422.67$  nm line (see Fig. 9) and  $0.1$  dex higher for neutral subordinate lines. The Ca II triplet, on the other hand, usually has negative corrections in 1D (e.g. Sitnova et al. 2019, Osorio et al. 2022), which may cancel or decrease even further in 3D (Lind et al. 2013, Nordlander et al. 2017, Lagae et al. 2023). Reassuringly, a  $0.5$  dex Ca ionisation imbalance seen in 1D LTE for an ultra metal-poor dwarf is strongly reduced in 1D non-LTE and removed completely in 3D non-LTE (Lagae et al. 2023). A similar degree of improvement was seen in 1D non-LTE for a larger sample of ultra metal-poor stars by Sitnova et al. (2019).

**3.3.3. Carbon, nitrogen, oxygen, and magnesium abundances from molecular lines.** Since the first discovery of metal-poor stars with anomalously strong CH features, C-enhanced metal-poor stars (CEMP stars) has continued to further our understanding of the very first stellar generations. Of particular importance in this context is the subclass CEMP-no, that are characterized by high abundances of light elements (C, N, O, Na, Mg, Al), but lack enhancement of neutron-capture elements (Norris & Yong 2019, and references therein). The fraction of CEMP stars grow steadily toward lower metallicity and they dominate the ultra metal-poor regime.

The only available CNO abundance indicators in  $[\text{Fe}/\text{H}] < -4$  stars are molecular bands, hence it is of great importance to understand the systematic uncertainties associated with them in model spectra. The first 3D RHD models that were created for metal-poor stars (Asplund & García Pérez 2001, Collet et al. 2006) showed that they have a profound impact on molecular line formation. As clearly illustrated by Dobrovolskas et al. (2013), the effect of the added granulation is larger than the change in temperature stratification. The contribution functions of molecules like CH, NH and OH extend to much shallower layers, strengthening synthetic line profiles and reducing abundances in 3D. CNO abundance corrections down to  $-1$  dex have been predicted for extremely metal-poor dwarfs (González Hernández et al. 2008, 2010, Gallagher et al. 2016) and giants (Collet et al. 2007, Hayek et al. 2011, Dobrovolskas et al. 2013). Some notable differences in the size of the predictions

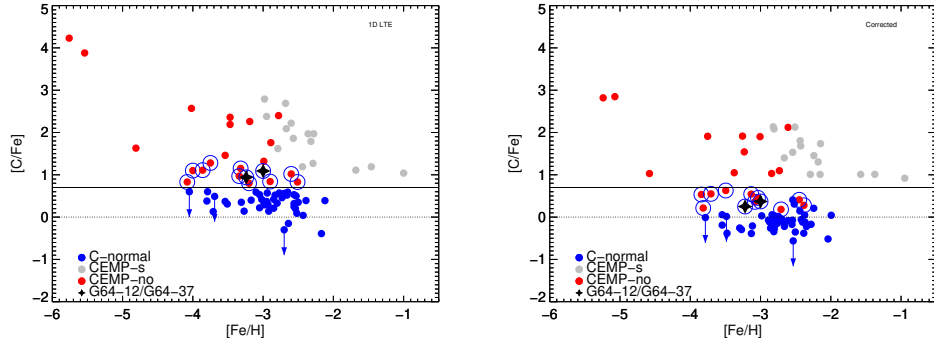


**Figure 11:** The left-hand panel shows 1D LTE abundances for C and Fe for the metal-poor star sample ( $T_{\text{eff}} < 6600$  K and  $\log g > 2$ ) of Yong et al. (2013) and two stars (G64-12 and G64-37) from Placco et al. (2016) and Norris & Yong (2019). The right-hand panel shows C abundances corrected using 3D LTE line formation of the CH-band, and Fe abundance corrected for 1D non-LTE effects. The stars marked with blue open circles would be categorized as C-enhanced in the left panel, but C-normal in the right panel.

for different stars do exist, but there is agreement on increasingly large negative corrections with decreasing metallicity. CH is often less affected by 3D effects than NH and OH, which in turn are less affected than CN and CO (e.g. Dobrovolskas et al. 2013).

It has also been recognised that the C/O ratio plays an important role in metal-poor 3D atmospheres, because of the atoms’ preference to form CO (Collet et al. 2007, Gallagher et al. 2016). When C and O abundances are optimized simultaneously or constrained by atomic lines, corrections between  $-0.2$  to  $-0.7$  dex for the UV OH bands and  $+0.05$  dex to  $-0.7$  dex for the CH bands have been reported for several stars (Behara et al. 2010, Bessell et al. 2015, Spite et al. 2017, Collet et al. 2018). Gallagher et al. (2016) quantified the impact of the C/O ratio in dwarfs; for example, when increasing the ratio from 0.2 to 4, the predicted OH lines become weaker while the CH lines become stronger and the 3D correction to the C abundance becomes more negative by  $-0.5$  dex at  $[\text{Fe}/\text{H}] = -3$ . Gallagher et al. (2017a) and Steffen et al. (2017) further pointed out the importance of consistency between the abundances used to construct the 3D RHD model atmosphere and the abundances used to synthesize the spectrum. However, the effects are at the  $0.1-0.3$  dex level and are reported at high C/O-ratios that are not necessarily representative of ultra metal-poor stars.

The agreement between C I and CH lines was investigated by Norris & Yong (2019), using 1D non-LTE corrections for C I by Fabbian et al. (2009) and 3D LTE corrections to CH based on several literature studies. They find good consistency down to  $[\text{Fe}/\text{H}] = -2.5$ , but that the atomic lines give  $\sim 0.5$  dex lower abundances than the molecules for the extremely metal-poor TO stars G64-12 and G64-36. In Fig. 11, we show the 1D LTE CH-based abundances of Yong et al. (2013) and compare them to 3D LTE abundances using new corrections based on Stagger-models and Scate. It can be seen that modelling assumptions indeed impact the classification of stars as C-enhanced, according to the traditional  $[\text{C}/\text{Fe}] > 0.7$  limit, in agreement with the conclusion of Norris & Yong (2019). However, our corrected  $[\text{C}/\text{Fe}]$  values are generally higher. For G64-12 and G64-36, we find an average  $[\text{C}/\text{Fe}] =$

0.19, which is only 0.05 – 0.1 dex higher than the values reported for atomic C lines by [Amarsi et al. \(2019c\)](#), after correcting for differences in stellar parameters.

For O, the agreement between atomic and molecular abundance indicators is less satisfactory. For the metal-poor giant HD122563, studies report almost solar [O/Fe] values based on the UV OH lines, 0.3–0.5 dex below the abundances derived from the [O I] 630 nm line ([Prakapavičius et al. 2017](#), [Collet et al. 2018](#)). For the metal-poor TO star HD84937, [Spite et al. \(2017\)](#) report reasonable agreement between 1D non-LTE abundances from the O I triplet and 1D LTE abundances from UV OH lines; applying an estimated 3D effect of –0.7 dex to the latter would again bring the [O/Fe] close to solar, in stark disagreement with the atomic lines. Missing continuous opacity in the the UV region may be part of the problem, or non-LTE effects over-predicting the strength of synthetic OH lines in LTE. [Spite et al. \(2017\)](#) speculate that the presence of a chromosphere, as implied by core emission in Mg H & K, may raise the temperature of the 3D model and improve the agreement. The OH infrared lines are better aligned with the atomic indicators ([Dobrovolskas et al. 2015](#)).

The N abundances of extremely metal-poor stars have attracted less attention. 3D LTE analyses of the UV NH and CN bands has been performed for individual stars (e.g. [Frebel et al. 2008](#), [Spite et al. 2013](#)), but not applied to large samples. This is crucial, considering the importance to understand the need for a primary source of this element and thus constrain the yields of AGB, super-AGB, and rotating massive stars at low metallicity ([Prantzos et al. 2018](#), [Kobayashi et al. 2020](#)). In [Spite et al. \(2005, 2013\)](#) a systematic offset of 0.4 dex between NH and CN-based N abundances were reported, as well as a possible 3D effect exceeding –2 dex for the CN band in TO stars, again largely dependent on the sensitivity of C/O.

Investigations have been made to understand the robustness of the predicted large negative 3D corrections for molecules. First, [Hayek et al. \(2011\)](#) concluded that accounting for continuum scattering in red giants has a relatively small impact on molecular line based abundances, in fact making them increasingly negative by up to 0.1 dex at  $[\text{Fe}/\text{H}] = -3$ . Secondly, [Popa et al. \(2023\)](#) recently performed 1D non-LTE calculations for the CH molecule and find that metal-poor stars indeed suffer from over-dissociation by radiation, which can affect abundances determined from the G band by +0.2 dex in ultra metal-poor giants. We caution that this result is likely to be sensitive to the collisional cross-sections with neutral hydrogen, which were computed with the Drawin formula in the lack of alternatives. However, if the sensitivity to departures from LTE is realistic, they may have an even greater impact in 3D. Non-LTE calculations for OH lines have so far only been tentatively explored with a two-level approximation in 1D ([Asplund & García Pérez 2001](#)). Full 3D non-LTE calculations for CNO-bearing molecules, including a systematic investigation of the impact of uncertainties in molecular data, are needed to shed further light on the abundances of the most metal-poor stars. Thirdly, deviations from molecular equilibrium was investigated by [Deshmukh & Ludwig \(2023\)](#) and found insignificant, as discussed in Sect. 2.5.2

Several lines of MgH are present around 510 nm in cool stars. The lines are not normally used to infer Mg abundances, but the isotopic shifts between molecular lines involving  $^{24}\text{Mg}$ ,  $^{25}\text{Mg}$  and  $^{26}\text{Mg}$  are of order 0.01 nm and thus detectable in high-resolution spectra, allowing determination of Mg isotopic ratios. The lightest isotope is produced primarily by SNe, while the two heavier signal contribution from AGB stars to the chemical enrichment. Mg isotopic ratios determined from MgH lines have therefore been used to constrain the chemical evolution of globular clusters and the Milky Way ([Thygesen et al. 2016](#), and

references therein). The error introduced in the inferred isotopic ratio when modelling the shapes of MgH lines in 1D was analysed by Thygesen et al. (2017) for metal-poor dwarfs and giants, with the result that  $^{25}\text{Mg}/^{24}\text{Mg}$  can be underestimated by up to five percent and  $^{26}\text{Mg}/^{24}\text{Mg}$  by up to two percent. This is small compared to the spread reported, for example, for the globular cluster  $\omega$  Centauri (Da Costa et al. 2013). [Mg/H] abundances determined from MgH lines in 1D, however, suffer effects of similar order as the CNO-bearing molecules, i.e., 3D corrections can reach  $-0.7$  dex in metal-poor dwarfs. In a recent study of  $\omega$  Centauri giants, Reddy (2020) determine 1D LTE abundances from both MgH and atomic Mg lines and find that while for some stars they are in agreement, for others they differ by up to  $+0.44$  dex. Intriguingly, the author argues that 3D and non-LTE effects, as known from literature, are not responsible for this difference, but that it reflects on a true difference in the atmospheric He abundance. Increasing the He mass fraction of the atmospheric model, relatively fewer hydrogen atoms are available to form MgH, and the lines decrease in strength to agree with the atomic ones.

**3.3.4. Iron-peak elements.** The elements with atomic number  $Z = 21 - 30$  share many important properties both in terms of nucleosynthetic origin and line formation. The first ionisation potentials fall in the range  $6.6 - 9.4$  eV and all the neutral atoms, except Cu and Zn, have complex term diagrams with up to four multiplets and a large number of theoretically predicted highly excited levels. This complexity makes full 3D non-LTE calculations extremely challenging. Several recent 1D non-LTE studies including non-hydrogenic photoionisation cross-sections (except for Ni), together with asymptotic model data for inelastic hydrogen collisions, have been performed, e.g. for Ti (Mallinson et al. 2022), Mn (Eitner et al. 2020), Ni (Eitner et al. 2023), Cu (Xu et al. 2022), and Zn (Sitnova et al. 2022), revealing significant over-ionisation of the neutral atoms. The typical size of the effect at  $[\text{Fe}/\text{H}] = -2$  is  $+0.2$  dex, which is similar to neutral Fe, slightly lower for Ni and Zn, slightly higher for Mn and Cu. Lines of both neutral and ionized species of Fe-peak elements are available and can in principle be used to verify the ionisation equilibrium, at least for a subset, however Cu II and Zn II require vacuum UV observations and Sc I and V I are not detectable in hot metal-poor dwarfs (Cowan et al. 2020, Ou et al. 2020).

The only 3D non-LTE investigation for an Fe-peak element other than Fe, for stars other than the Sun, has been performed for Mn in metal-poor dwarfs and giants by Bergemann et al. (2019) and we therefore mainly limit further discussion to this element. Substantial positive 3D non-LTE corrections are reported, such that the difference with respect to 1D (MARCS) LTE is approximately  $+0.4$  dex for Mn I lines and  $+0.15$  dex for Mn II lines, for a very metal-poor dwarf and subgiant. The numbers are similar to those found for Fe for the same stars (Amarsi et al. 2016b, 2022), which reflects on robustness in the [Mn/Fe] ratio. However, for the metal-poor giant HD122563, the effect reported for Mn I ( $+1$  dex) and for Mn II ( $+0.4$  dex), are much higher than found for Fe I ( $+0.17$  dex) and Fe II ( $+0.08$  dex) in Amarsi et al. (2016b). This difference is not expected, given that the same 3D RHD model was used in Amarsi et al. (2016b) and Bergemann et al. (2019). We recommend further, independent 3D non-LTE studies to understand if [Mn/Fe] is indeed sub-solar or super-solar in this star.

Fe-peak elements are produced in the explosive nucleosynthesis of thermonuclear and core-collapse SNe, with relative yields that depend strongly on the nature of the explosion (e.g. Nomoto et al. 2013). Eitner et al. (2020) demonstrate a close to flat [Mn/Fe] trend over several dex in metallicity, in agreement with the 3D non-LTE abundances for Mn by

Bergemann et al. (2019), can be achieved if hypernovae are neglected and a high fraction of SNIa explode with sub-Chandrasekhar mass. However, we note that Fe was not consistently corrected for non-LTE for the lowest metallicity stars from Bonifacio et al. (2009) which were included in the Eitner et al. (2020) study, and their [Mn/Fe] ratios were therefore inflated. At  $[\text{Fe}/\text{H}] = -2$ , [Mn/Fe] is reported at  $\sim -0.1$  dex, which is approximately 0.2 dex higher than the 1D non-LTE [Mn/Fe] ratios found by other studies with the same Mn corrections (Amarsi et al. 2020b, Hansen et al. 2020, Nissen et al. 2023). These latter results are in turn 0.2 dex higher than the Kobayashi et al. (2020) GCE model including hypernovae and only near-Chandrasekhar mass SNIa. Additional observational evidence to support the sub-Chandrasekhar mass channel is provided by mildly super-solar non-LTE [Ni/Fe]-ratios (Eitner et al. 2023). The suggested predominance of the sub-Chandrasekhar mass channel should be further explored with consistent 3D non-LTE calculations for Mn, Fe, and Ni.

**3.3.5. Barium.** Ba is among the most well studied of the neutron-capture elements, largely thanks to the availability of strong optical absorption lines of Ba II. According to our current understanding of Galactic chemical evolution, the element has multiple formation sites; at the lowest metallicities, contributions from both a rapid (r-process) channel in core-collapse SNe and/or compact star mergers as well as a slow (s-process) channel in rotating massive stars are necessary to raise the model predictions to observed levels (Prantzos et al. 2018). The s-process nucleosynthesis in low and intermediate mass AGB stars becomes noticeable at  $[\text{Fe}/\text{H}] > -1.5$ , which combined with the simultaneous Fe enrichment of SNIa produces a close to solar [Ba/Fe] ratio.

Non-LTE effects in 1D models have recently been investigated for Ba II lines by several studies (Mashonkina & Belyaev 2019, Hansen et al. 2020, Mashonkina et al. 2023), making use of asymptotic model data for inelastic hydrogen collisions as computed by Belyaev & Yakovleva (2017, 2018). At extremely low metallicity, over-ionisation and over-excitation (see e.g. Andrievsky et al. 2009) produce positive abundance corrections for Ba II 455.4 nm, that can exceed +0.2 dex. At increasing metallicity and line strength, photon losses lead to more negative corrections down to  $-0.2$  dex for the resonance line and even more negative for subordinate lines (Hansen et al. 2020, Mashonkina et al. 2023). As shown by Hansen et al. (2020), the [Ba/Fe] trend in the range  $-3 < [\text{Fe}/\text{H}] < -1$  is shifted downwards by approximately 0.3 dex and flattened when both elements are consistently treated in 1D non-LTE. This improves the agreement with the GCE model by Prantzos et al. (2018).

3D LTE abundance analyses of Ba II lines point to corrections of up to +0.18 dex for subordinate lines in metal-poor red giants (Dobrovolskas et al. 2012), while  $-0.15$  dex was found for the resonance line in the metal-poor subgiant HD140283 (Gallagher et al. 2015). Dobrovolskas et al. (2012) and Mishenina et al. (2009) both emphasize the strong sensitivity of the 1D abundance to the choice of the fudge parameter microturbulence. A consistent 3D non-LTE treatment is indeed particularly important for saturated lines, but such analysis has so far only been performed for the Sun by Gallagher et al. (2020). They demonstrate a cancellation between substantial positive 3D effects and negative non-LTE effects such that their combined impact on the Ba abundance is small for the Sun, 0.03 dex higher than 1D LTE. This cannot, however, be extrapolated to metal-poor stars.

In addition to the absolute abundances of Ba and other neutron capture elements, important clues to the nucleosynthesis channels involved in their creation comes from the isotopic ratios. Specifically, the ratio between odd and even Ba isotopes is different for the

s-process and r-process, and this ratio can be determined from a careful profile analysis of the Ba II resonance line, because the odd isotopes show significant hyper-fine splitting. The larger the contribution from the s-process, the broader the line. Mashonkina & Belyaev (2019) enforced agreement in the Ba abundance from the resonance and subordinate lines in 1D non-LTE, and thereby found a clearly dominant r-process origin of the element in four metal-poor stars. In contrast, Collet et al. (2009) used Fe lines to constrain broadening due to micro/macroturbulence (in the 1D case) and rotation and found that a 3D LTE analysis of HD140283 reduced the ratio between odd and even isotopes compared to a 1D analysis, thus favouring an s-process origin of Ba. This result was later challenged by Gallagher et al. (2015), who found the opposite behaviour with a 3D LTE analysis, supporting a predominant r-process origin in this star. The authors speculate that the former result was caused by problems with the line selection or with the 3D RHD model used previously, e.g., erroneous temperature, insufficient resolution or opacity bins. Clearly, this type of application is the ultimate challenge for stellar atmosphere modelling and synthetic line formation; a 3D non-LTE profile analysis of the Ba isotopic ratio would certainly shed further light on the matter.

### 3.4. Planet-host stars

We will now briefly comment on the implications that improved models of stellar spectra may have for our understanding of exoplanets and their host stars. We focus on spectral line formation in this review, but note that several studies have also been devoted to using 3D RHD models to characterize intrinsic stellar brightness fluctuations that may interfere with planetary detection (e.g. Rodríguez Díaz et al. 2022).

**3.4.1. Chemical compositions of planet hosts.** Thanks to the ever increasing number of exoplanet discoveries, numerous investigations have been made between stellar properties, such as chemical abundances, and planet occurrence and properties. First, the now well-established correlation between stellar metallicity and occurrence rate of giant planets (e.g. Adibekyan 2019), has been extended to consider additional aspects, e.g. planetary mass, radius, orbital properties, heavy-metal content, and stellar alpha-element abundance (e.g. Biazzo et al. 2022, and references therein). Second, significant trends have been found in relative abundances with respect to condensation temperature between the Sun and carbonaceous chondrites on the one hand, and the Sun and solar twins on the other hand (Asplund et al. 2021, Nissen & Gustafsson 2018). Several proposed explanations have been put forth, involving formation of both terrestrial and giant planets, but the observational landscape is complex, with the intertwined effects of age, chemical evolution, and radial migration clouding the picture. Third, planet properties have been linked to specific element abundances; Li, because of its unique sensitivity to stellar rotation and mixing (Delgado Mena et al. 2015, Carlos et al. 2019), and C/O and Mg/Si because of their decisive influence on the planetary mineralogy (Brewer & Fischer 2016, Suárez-Andrés et al. 2018).

In order to disentangle different intrinsic sources of abundance differences, the analysis for such applications as those mentioned above must in general be very precise, with systematic errors not exceeding 0.05 dex. However, exoplanet host stars are found all over the HR diagram, populating the main sequence from M to B dwarfs, and extending to the subgiant and red giant branches for late-type stars (e.g. Berger et al. 2018, Janson et al. 2021). While systematic effects may largely cancel in differential abundance analyses



of twin stars, this is obviously further from the truth the more extended the parameter space. The lowest metallicity stars known to host planets lie arguably somewhere around  $[\text{Fe}/\text{H}] \approx -1.0$  (Adibekyan 2019). In this range, 3D non-LTE  $[\text{Fe}/\text{H}]$  may differ from 1D LTE by up to 0.2 dex for FG dwarfs (Amarsi et al. 2022) — even more if 1D LTE spectroscopic stellar parameters are used (Sect. 3.2.2) — and must be considered, for example, when stellar abundances are compared to model predictions of the critical metallicity for planet formation (Johnson & Li 2012).

The C/O ratio of the planet-forming environment determines whether Si forms carbide or oxide species, with a critical limit at  $\text{C}/\text{O} = 0.8$ . As discussed by Nissen & Gustafsson (2018), several high-precision studies have shown that the C/O ratio of solar-type stars stays below this value. Amarsi et al. (2019c) confirmed this and also showed that 3D non-LTE effects, applied differentially with respect to the Sun, decreases the C/O ratios for sub-solar metallicity stars, but increases them for super-solar metallicity. Interestingly, the 3D non-LTE abundances showed that confirmed planet-host stars have systematically higher C/O ratios than the comparison sample for  $[\text{O}/\text{H}] > 0$ , which speculatively links the C/O ratio to planet formation efficiency.

The Mg/Si ratio governs the distribution of silicates in the planets. The solar ratio is very close to one; the value in CI-chondrites is 1.03 (Lodders 2021), but whether it is larger or smaller than one is not definitely settled in the solar photosphere (see Sect. 3.1.3). A correlation between Mg/Si ratio of planet-hosts and the planetary mass has been reported, claiming that the ratio is higher in stars with low-mass planets (Adibekyan et al. 2015, Biazzo et al. 2022), a result that is not strongly influenced by 1D non-LTE calculations (Adibekyan et al. 2017). However, for both elements the sensitivity to the model atmosphere can exceed the non-LTE effect for solar-type stars (Scott et al. 2015b) and we recommend that the Mg/Si of planet-hosts be reappraised with 3D non-LTE calculations.

**3.4.2. Transmission spectroscopy.** When a planet is in transit in front of its host, the light from the star is partly obscured, but also partly filtered through the planetary atmosphere. Thereby, transmission spectroscopy can help characterize the physical conditions and chemical composition at the surfaces of exoplanets. However, to accurately extract the planetary signal, the CLV of the stellar disc must be considered. Lines that are present in both the planetary and the stellar atmosphere are particularly complicated if they are blended, and erroneous planetary signal can be inferred if the stellar CLV is not accounted for (Casasayas-Barris et al. 2020). Naturally, 1D LTE model predictions of the CLV can also be expected to lead to errors, since it is well known that they cannot reproduce spatially resolved solar observation (Sect. 2.4). Yan et al. (2017) showed that transmission curves for a solar-type star are moderately flattened by 1D non-LTE calculations for the Na D lines, a result that was later confirmed for more species and also extended to 3D LTE by Reiners et al. (2023). The size of the effect varies with the observational configuration of the star-planet system, e.g., the impact parameter and passband, but evidently, the difference between transmission curves modelled under different assumptions can be as large as the CLV effect itself. Canocchi et al. (2023) illustrate that 3D non-LTE modelling produces the best match to the CLV of the resonance lines of Na and K in the Sun. The best-fit line profile and simulated transmission curves for a Jupiter-Sun system are shown in Fig. 12. The calculations can readily be extended to other FGK-type stars and planetary configurations.



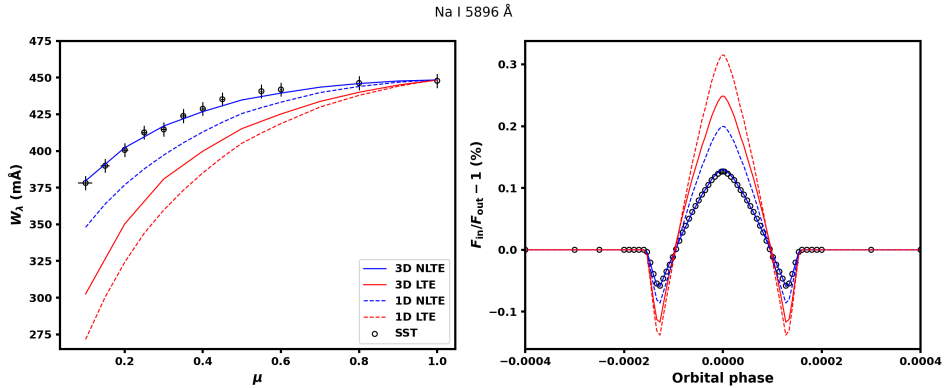


**Figure 12:** Observed and modelled CLV of the equivalent width of the Na I 589.6 nm line (left). All model curves have been normalised to their best-fit abundance at disc centre. The right-hand panel shows simulated transmission curves from a Jupiter-Sun edge-on system. In both panels, the 3D non-LTE model provides an excellent match to the observed data from the Swedish Solar Telescope, SST. From [Canocchi et al. \(2023\)](#).

## 4. DISCUSSION AND OUTLOOK

This century has seen tremendous improvement of model atmospheres and synthetic spectra for late-type stars. Grids of 3D RHD models have been computed and successfully validated against solar and stellar observations, for example in terms of abundance determination, CLV, spectral line shapes, and statistical properties of granulation. Applying non-LTE radiative transfer in the post-processing of snapshots of 3D RHD models is numerically expensive, but is becoming a feasible alternative for large-scale parameter and abundance analysis. Fig. 13 shows an overview of 3D (non-)LTE abundance analyses and hydrogen-line analyses for late-type stars other than the Sun over the past 25 years. As evident from the figure, the number of 3D RHD models used for grid calculations and quantitative spectroscopy has grown substantially, starting from a handful of models to now encompassing the full *Stagger* and *CIFIST*-grids shown in Fig. 2. Furthermore, we see a simultaneous shift from predominantly 3D LTE calculations to 3D non-LTE. The publications used to create this figure are listed in Table 1.

### 4.1. The transition from 1D LTE to 3D non-LTE

The gradual transitioning from the use of 1D LTE models to 3D non-LTE models may look different for different types of applications. Before we proceed with some general advice in this regard, we remind the reader that quantitative stellar spectroscopy includes a variety of sources of error such as continuum placement, blends, and atomic data (oscillator strengths), that are not directly related to the 3D non-LTE models themselves (as we have discussed, for example, in the context of the solar composition; Sect. 3.1). With the development of more realistic model atmospheres and synthetic spectra, a careful handle of these errors become all the more important.

Traditional (1D LTE) spectroscopic analysis is build on careful selection and fitting of individual lines. Line-by-line differential analyses can achieve remarkable precision, as

demonstrated e.g. for solar twins and analogues with respect to the Sun (e.g. [Nissen 2015](#), [Liu et al. 2016](#), [Bedell et al. 2018](#)), but also metal-poor stars with respect to benchmark stars ([Hawkins et al. 2016](#), [Reggiani et al. 2017](#)). The smaller the parameter space covered by a given study, the smaller the differential impact of 3D non-LTE calculations, although this depends on the science goal as well as the lines being analysed. [Nissen & Gustafsson \(2018\)](#) found that, as a rule of thumb, the forbidden O lines are reliable in a differential sense also with simplistic modelling if one limits the parameter space to 500 K in  $\Delta T_{\text{eff}}$  and 0.5 dex in  $\Delta \log g$  for solar-type stars. On the other hand, this is not true for an element like Li, which can have substantially different line strengths in stars with the same fundamental parameters, and for saturated lines like the O I 777 nm triplet ([Meléndez et al. 2017](#)).

To improve the accuracy of 1D LTE abundances, pre-computed 3D non-LTE abundance corrections can be applied. This is now possible for several species, on relatively extended grids of at least 40 combinations of  $T_{\text{eff}}$ ,  $\log g$ , and  $[\text{Fe}/\text{H}]$ : Li I, C I, O I, Mg I, Fe I, and Fe II. The user should be careful that the microturbulence value used in the 1D LTE analysis is the same as that used to calculate the 3D versus 1D abundance correction, to properly translate the 1D LTE abundance (microturbulence-dependent) to a 3D non-LTE one (microturbulence-independent). Directly fitting pre-computed 3D non-LTE spectra to observations for individual lines is also an option, and can include masking or empirical fitting of blends (e.g. [Giribaldi et al. 2023](#), [Wang et al. 2024](#)). For species where non-LTE effects are small (e.g. Fe II), 3D LTE abundance corrections and spectra can be used; such models are much cheaper to calculate and do not require model atoms.

Similarly, one may also consider using 1D or <3D> non-LTE abundance corrections or spectra to improve the accuracy of 1D LTE abundances. However, the 3D granulation effect, missing in both 1D and <3D> models, is large for temperature sensitive lines: namely, those of low excitation potential for minority species, and of high excitation potential for majority species; but cancellation effects due to the simultaneous change in mean atmospheric structure can occur. Using <3D> models may therefore improve abundances for temperature-insensitive lines, but they capture only a small part of the full 3D effect for other lines. The situation is worse if the lines are saturated and are thus highly sensitive to the velocity fields, crudely approximated in 1D and <3D> models by microturbulence and macroturbulence. Although the use of non-LTE calculations in 1D and <3D> models can significantly improve the ionisation balance with respect to 1D LTE, the absolute abundances can still be offset from 3D non-LTE due to the extra calibration parameters, and such models may also perform poorly for the excitation balance and for hydrogen line profiles (Sect. 3.2). The use of 3D LTE abundances combined with 1D or <3D> non-LTE corrections, in the lack of full 3D non-LTE calculations, may be justified for metal-rich stars like the Sun, whose atmospheric structures are in radiative equilibrium, but can introduce large errors for metal-poor stars (Sect. 2.5.2).

Unfortunately, 3D non-LTE calculations are expensive, and the amount of available 3D non-LTE data are far from sufficient for the demands of current large spectroscopic surveys. Significant computational gain may be accomplished by calculating non-LTE populations or departure coefficients with (open source) 1.5D non-LTE codes (Sect. 2.3.1) and reading them into a 3D LTE codes such as `LinFor3D`, `Scate`, `OPTIM3D`, or `ASSET` so as to obtain a 1.5D non-LTE disc-integrated spectrum which in some cases may satisfactorily approximate the full 3D non-LTE result, given all the other uncertainties ([Amarsi et al. 2016a](#), [Nordlander et al. 2017](#)). Another approach worth exploring further is to use machine learning to predict non-LTE populations from their 3D LTE counterparts ([Chappell & Pereira 2022](#)).

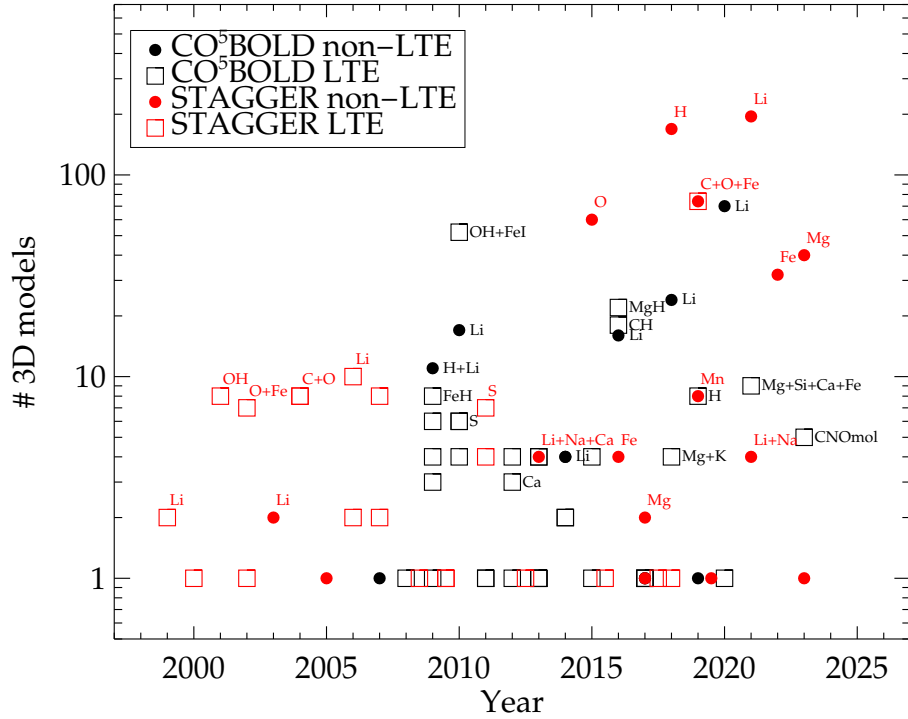


**Figure 13:** Overview of refereed publications of 3D (non-)LTE hydrogen line formation and abundance analyses for stars other than the Sun. The y-axis represents the number of 3D RHD models used (corresponding to different values of  $T_{\text{eff}}$ ,  $\log g$ , and  $[\text{Fe}/\text{H}]$ ). Species names are indicated for selected studies only. The references are listed in Table 1.

Spectroscopic surveys typically require high resolution spectrum synthesis including all detectable lines over a large wavelength interval. In the near future these surveys will benefit from grids of hybrid 1D LTE/non-LTE spectra generated using pre-computed grids of departure coefficients. The third data release of the GALAH survey treats 13 elements in non-LTE (Amarsi et al. 2020b), a number that will grow further before 4MOST (de Jong et al. 2019) sees first light. To mitigate errors in stellar parameters due to the use of 1D models for spectrum generation, photometric, astrometric and asteroseismic constraints can be folded into the analysis (e.g. Buder et al. 2021, Gent et al. 2022), in particular if colours and bolometric corrections use scaling relations based on 3D work (Sect. 3.2.3). It is a safe expectation that analogous hybrid 3D LTE/non-LTE spectra will become available in the future, but to truly give superior performance, they may need to treat essentially all minority species with significant absorption in non-LTE, given that departures from LTE are generally amplified. Grids of high-resolution 3D LTE spectra with large wavelength coverage are already available (Chiavassa et al. 2018, Bertran de Lis et al. 2022).

## 4.2. Future methodological developments

To facilitate 3D non-LTE abundance analyses, it seems necessary to extend the existing grids of model atmospheres. For instance, the current extent of the **Stagger** and **CIFIST** grids would benefit from more complete coverage of the very metal-poor red giant branch. However, warm, low-surface gravity models have the largest run-times as discussed in Sect. 2.1.4, and are the most challenging to relax. The development of better techniques to initialize new models with appropriate bottom boundary conditions, perhaps involving elements of machine learning, would be welcome. This can be done by using existing boundary conditions (energy and density values) and find lines of similar entropy, taking the variation in depth and metallicity of the models into account. It is also desirable to refine the grids. The nodes of the existing 3D **Stagger** grid are separated by up to 500 K in  $T_{\text{eff}}$ , 0.5 dex in  $\log g$  and 0.5 – 1 dex in  $[\text{Fe}/\text{H}]$  (Fig. 2); the step-sizes in  $T_{\text{eff}}$  and  $[\text{Fe}/\text{H}]$  are typically twice as large as the commonly used 1D **MARCS** grid (Gustafsson et al. 2008). Nevertheless, accurate interpolation of 3D non-LTE stellar spectra generated with the grid has been shown to be possible, e.g., using a method based on Gaussian process regression (Wang et al. 2021). With interpolation in four dimensions, i.e., the three stellar parameters and Li abundance, interpolation errors that correspond to 0.01 dex in abundance can be achieved. Bertran de Lis et al. (2022) uses an interpolation technique based on radial basis functions for the high-resolution 3D LTE full optical spectra computed for the **CIFIST**-grid and reports errors of  $< 2\%$  in flux. These results are promising, but larger errors are to be expected for a higher-dimensional abundance space and reducing the step size of the 3D grids would certainly be beneficial for applications that require high precision.

Improvements to the physics in the 3D RHD simulations may also be important, particularly for metal-poor stars where 3D non-LTE effects are often largest. Improvements to the opacity binning approach (Sect. 2.1.3) could cause changes to the temperature stratifications, which are predicted to be several hundred Kelvin cooler in 3D than in 1D for metal-poor stars. Such changes would have potentially large effects on temperature sensitive diagnostics (e.g. C abundances from CH lines, Sect. 3.3.3). Another future step is to investigate the validity of the restricted non-LTE problem by propagating the non-LTE level populations into the binned opacities. A more immediate consideration is the input abundances of the simulations (Gallagher et al. 2017a, Zhou et al. 2023). The most metal-poor stars have elemental abundance ratios that are peculiar (compared to the Sun), and it may be necessary to relax the trace-element assumption in order to obtain the most accurate results. The importance of consistency between the chemical composition used to construct the model atmosphere and the synthetic spectrum was tested for a solar-metallicity red giant by Ting et al. (2016, see Appendix A), concluding that a significant impact, increasing toward cooler temperatures, is seen in particular for what they call primary elements (C, N, Mg, Si, Fe), but also non-negligible impact for secondary elements (O, Na, Al, Ca, Ti). A specific example of how inconsistent abundances can lead to false abundance spreads in metal-poor globular clusters was shown for the Ca II triplet, whose line strengths are sensitive to the abundance of important electron donors like Mg (Mucciarelli et al. 2012). However, these studies are based on 1D atmospheres, while studies in 3D are so far limited, e.g., to the models with C/O enhanced above unity mentioned in Sect. 3.3.3.

To our knowledge, all 3D non-LTE abundance results so far have considered one element at a time. The validity of the single-element approach was investigated by Osorio et al. (2020) in 1D non-LTE for the elements Na, Mg, K, and Ca using **TLUSTY** (Hubeny & Lanz 2017). They found that departures from LTE for Mg affect those of Ca due to changes

to the ultra-violet (UV) opacity, amounting to differences in Ca abundance of  $-0.07$  dex for the Sun, but they do not find significant effects for the other elements. However, this result is sensitive to the amount of other UV opacity included in the models, and was not confirmed by [Asplund et al. \(2021\)](#), and furthermore appears to be insignificant in metal-poor stars ([Osorio et al. 2022](#)). Nevertheless, future work should aim to relax the single-element approximation, and ultimately move beyond the restricted non-LTE problem; this is already feasible with 1D models and realistic model atoms.

Finally, the non-LTE solutions are only as reliable as the model atoms that they are drawn upon (Sect. 2.2), which in turn are reliant on accurate and complete sets of atomic (and molecular) data — non-LTE calculations with unrealistic model atoms may give results of lesser overall accuracy than LTE. The fundamental theoretical and experimental work carried out by atomic (astro-)physicists should not be overlooked or taken for granted. In particular, non-hydrogenic photo-ionisation cross-sections are missing for several Fe-peak and neutron capture elements. On top of that, the physics of excitation by hydrogen collisions is still not satisfactorily understood, with significant impact on the solar O abundance for example (Sect. 3.1.2). Ongoing theoretical and experimental investigations may help in this regard ([Barklem et al. 2021](#), [Grumer et al. 2022](#)).

### 4.3. Concluding remarks

In this review, we have discussed how 3D non-LTE abundances have already shed new light on a number of astrophysical problems (Sect. 3), specifically:

1. They contributed to the lowering of the solar O abundance and helped reveal the solar modelling problem (Sect. 3.1)
2. They have mitigated or removed large systematic uncertainties in spectroscopic stellar parameter determination (Sect. 3.2)
3. They have removed the need for a cosmological origin of  ${}^6\text{Li}$  and helped us better define and interpret the Spite plateau in the context of Big Bang nucleosynthesis and stellar depletion (Sect. 3.3.1)
4. They have removed the need for C-production in excess of O in the early universe (Sect. 3.3.2)
5. They have helped calibrate and validate core-collapse SNe and HNe yields of  $\alpha$ -elements (Sect. 3.3.2)
6. They have uncovered previously unseen substructure in the  $[\text{Mg}/\text{Fe}]$ – $[\text{Fe}/\text{H}]$  plane in low- $\alpha$  halo (Sect. 3.3.2)
7. They have highlighted the importance of the sub-Chandrasekhar mass channel of SNIa (Sect. 3.3.4)
8. They have helped us trace the r-process origin of Ba in very metal-poor stars (Sect. 3.3.5)
9. They have helped uncover a relationship between stellar C/O-ratios and likelihood to host Jupiter-mass exo-planets (Sect. 3.4.1)
10. By their ability to accurately predict the CLV of spectral lines, they are fundamental for the characterization of exo-planet atmospheres through transmission spectroscopy (Sect. 3.4.2)

We have every reason to believe that this list will continue to grow in the years to come, but the rate of progress will reflect on the investment of researchers' time and resources.

## DISCLOSURE STATEMENT

The authors are not aware of any affiliations, memberships, funding, or financial holdings that might be perceived as affecting the objectivity of this review.

## ACKNOWLEDGMENTS

We are grateful to several colleagues for valuable contributions to this work in the form of discussions, detailed comments and figures, in particular Paul Barklem, Gloria Canocchi, Bengt Edvardsson, Nicolas Grevesse, Cis Lagae, Jonas Klevas, Hans Ludwig, Poul-Erik Nissen, Luisa Fernanda Rodríguez Díaz, Matthias Steffen, and Ella Xi Wang. KL acknowledge funds from the Knut and Alice Wallenberg foundation, and the European Research Council (ERC) under the European Union's Horizon 2020 research and innovation programme (Grant agreement No. 852977). AMA acknowledges support from the Swedish Research Council (VR 2020-03940).

## LITERATURE CITED

- Adibekyan V. 2019. *Geosciences* 9(3):105
- Adibekyan V, Gonçalves da Silva HM, Sousa SG, et al. 2017. *Astrophysics* 60(3):325–332
- Adibekyan V, Santos NC, Figueira P, et al. 2015. *A&A* 581:L2
- Akerman CJ, Carigi L, Nissen PE, Pettini M, Asplund M. 2004. *A&A* 414:931–942
- Albert D, Antony BK, Ba YA, et al. 2020. *Atoms* 8(4):76
- Alexeeva S, Ryabchikova T, Mashonkina L, Hu S. 2018. *ApJ* 866(2):153
- Alexeeva SA, Mashonkina LI. 2015. *MNRAS* 453(2):1619–1631
- Allende Prieto C, Asplund M, Fabiani Bendicho P. 2004. *A&A* 423:1109–1117
- Allende Prieto C, Asplund M, García López RJ, Lambert DL. 2002. *ApJ* 567(1):544–565
- Allende Prieto C, Lambert DL, Asplund M. 2001. *ApJ* 556(1):L63–L66
- Allende Prieto C, Lambert DL, Hubeny I, Lanz T. 2003. *ApJS* 147(2):363–368
- Altrock RC. 1968. *Sol. Phys.* 5(3):260–280
- Amarsi AM. 2016. Ph.D. thesis, Australian National University, Canberra
- Amarsi AM, Asplund M. 2017. *MNRAS* 464(1):264–273
- Amarsi AM, Asplund M, Collet R, Leenaarts J. 2015. *MNRAS* 454:L11–L15
- Amarsi AM, Asplund M, Collet R, Leenaarts J. 2016a. *MNRAS* 455(4):3735–3751
- Amarsi AM, Barklem PS. 2019. *A&A* 625:A78
- Amarsi AM, Barklem PS, Asplund M, Collet R, Zatsarinny O. 2018a. *A&A* 616:A89
- Amarsi AM, Barklem PS, Collet R, Grevesse N, Asplund M. 2019a. *A&A* 624:A111
- Amarsi AM, Grevesse N, Asplund M, Collet R. 2021. *A&A* 656:A113
- Amarsi AM, Grevesse N, Gruner J, et al. 2020a. *A&A* 636:A120
- Amarsi AM, Liljegren S, Nissen PE. 2022. *A&A* 668:A68
- Amarsi AM, Lind K, Asplund M, Barklem PS, Collet R. 2016b. *MNRAS* 463(2):1518–1533
- Amarsi AM, Lind K, Osorio Y, et al. 2020b. *A&A* 642:A62
- Amarsi AM, Nissen PE, Asplund M, Lind K, Barklem PS. 2019b. *A&A* 622:L4
- Amarsi AM, Nissen PE, Skúladóttir Á. 2019c. *A&A* 630:A104
- Amarsi AM, Nordlander T, Barklem PS, et al. 2018b. *A&A* 615:A139
- Anders E, Grevesse N. 1989. *Geochim. Cosmochim. Acta* 53(1):197–214
- Anderson LS. 1989. *ApJ* 339:558
- Andrievsky SM, Spite M, Korotin SA, et al. 2009. *A&A* 494(3):1083–1090
- Andrievsky SM, Spite M, Korotin SA, et al. 2010. *A&A* 509:A88
- Asplund M. 2005. *ARA&A* 43(1):481–530
- Asplund M, Amarsi AM, Grevesse N. 2021. *A&A* 653:A141

- Asplund M, Carlsson M, Botnen AV. 2003. *A&A* 399:L31–L34
- Asplund M, García Pérez AE. 2001. *A&A* 372:601–615
- Asplund M, Grevesse N, Sauval AJ, Allende Prieto C, Kiselman D. 2004. *A&A* 417:751–768
- Asplund M, Grevesse N, Sauval AJ, Scott P. 2009. *ARA&A* 47(1):481–522
- Asplund M, Lambert DL, Nissen PE, Primas F, Smith VV. 2006. *ApJ* 644(1):229–259
- Asplund M, Nordlund Å, Trampedach R, Allende Prieto C, Stein RF. 2000a. *A&A* 359:729–742
- Asplund M, Nordlund Å, Trampedach R, Stein RF. 1999. *A&A* 346:L17–L20
- Asplund M, Nordlund Å, Trampedach R, Stein RF. 2000b. *A&A* 359:743–754
- Athay RG, Lites BW. 1972. *ApJ* 176:809
- Auer L. 1991. In *Stellar Atmospheres - Beyond Classical Models*, vol. 341 of *NATO ASI Ser. C*.
- Auer L. 2003. In *Stellar Atmosphere Modeling*, vol. 288 of *ASP Conf. Ser.*
- Auer L, Bendicho PF, Trujillo Bueno J. 1994. *A&A* 292:599–615
- Ayres TR, Wiedemann GR. 1989. *ApJ* 338:1033
- Bailey JE, Nagayama T, Loisel GP, et al. 2015. *Nature* 517(7532):56–59
- Balmforth NJ, Gough DO. 1990. *Sol. Phys.* 128(1):161–193
- Bard S, Carlsson M. 2008. *ApJ* 682(2):1376–1385
- Barklem PS. 2016a. *A&A Rev.* 24(1):9
- Barklem PS. 2016b. *Phys. Rev. A* 93(4):042705
- Barklem PS. 2017. Astrophysics Source Code Library, record ascl:1701.005
- Barklem PS. 2018a. *A&A* 612:A90
- Barklem PS. 2018b. *A&A* 610:A57
- Barklem PS, Amarsi AM, Gruner J, et al. 2021. *ApJ* 908(2):245
- Barklem PS, Belyaev AK, Asplund M. 2003. *A&A* 409:L1–L4
- Barklem PS, Belyaev AK, Dickinson AS, Gadéa FX. 2010. *A&A* 519:A20
- Barklem PS, Belyaev AK, Guitou M, et al. 2011. *A&A* 530:A94
- Barklem PS, Belyaev AK, Spielfiedel A, Guitou M, Feautrier N. 2012. *A&A* 541:A80
- Barklem PS, Collet R. 2016. *A&A* 588:A96
- Barklem PS, Osorio Y, Fursa DV, et al. 2017. *A&A* 606:A11
- Barklem PS, Piskunov N, O’Mara BJ. 2000. *A&AS* 142:467–473
- Barklem PS, Stempels HC, Allende Prieto C, et al. 2002. *A&A* 385:951–967
- Basu S, Antia HM. 2008. *Phys. Rep.* 457(5-6):217–283
- Bautista MA, Lind K, Bergemann M. 2017. *A&A* 606:A127
- Bautista MA, Romano P, Pradhan AK. 1998. *ApJS* 118(1):259–265
- Bedell M, Bean JL, Meléndez J, et al. 2018. *ApJ* 865(1):68
- Beck B, Collet R, Steffen M, et al. 2012. *A&A* 539:A121
- Behara NT, Bonifacio P, Ludwig HG, et al. 2010. *A&A* 513:A72
- Belmonte MT, Gavanski L, Djurović S, Mar S, Aparicio JA. 2021. *J. Quant. Spectr. Rad. Transf.* 271:107703
- Bely O, van Regemorter H. 1970. *ARA&A* 8:329
- Belyaev AK. 2013. *Phys. Rev. A* 88(5):052704
- Belyaev AK, Barklem PS. 2003. *Phys. Rev. A* 68(6):062703
- Belyaev AK, Barklem PS, Dickinson AS, Gadéa FX. 2010. *Phys. Rev. A* 81(3):032706
- Belyaev AK, Barklem PS, Spielfiedel A, et al. 2012. *Phys. Rev. A* 85(3):032704
- Belyaev AK, Voronov YV. 2020. *ApJ* 893(1):59
- Belyaev AK, Yakovleva SA. 2017. *A&A* 608:A33
- Belyaev AK, Yakovleva SA. 2018. *MNRAS* 478(3):3952–3960
- Bergemann M, Collet R, Amarsi AM, et al. 2017a. *ApJ* 847(1):15
- Bergemann M, Collet R, Schönrich R, et al. 2017b. *ApJ* 847(1):16
- Bergemann M, Gallagher AJ, Eitner P, et al. 2019. *A&A* 631:A80
- Bergemann M, Hoppe R, Semenova E, et al. 2021. *MNRAS* 508(2):2236–2253
- Bergemann M, Lind K, Collet R, Magic Z, Asplund M. 2012. *MNRAS* 427(1):27–49



- Bergemann M, Serenelli A, Schönrich R, et al. 2016. *A&A* 594:A120
- Berger TA, Huber D, Gaidos E, van Saders JL. 2018. *ApJ* 866(2):99
- Bertran de Lis S, Allende Prieto C, Ludwig HG, Koesterke L. 2022. *A&A* 661:A76
- Bessell MS, Collet R, Keller SC, et al. 2015. *ApJ* 806(1):L16
- Biazzo K, D’Orazi V, Desidera S, et al. 2022. *A&A* 664:A161
- Björge JP, Leenaarts J. 2017. *A&A* 599:A118
- Bonifacio P, Caffau E, Ludwig HG. 2010. *A&A* 524:A96
- Bonifacio P, Caffau E, Ludwig HG, et al. 2018a. *A&A* 611:A68
- Bonifacio P, Caffau E, Spite M, et al. 2018b. *A&A* 612:A65
- Bonifacio P, Caffau E, Venn KA, Lambert DL. 2012. *A&A* 544:A102
- Bonifacio P, Spite M, Cayrel R, et al. 2009. *A&A* 501(2):519–530
- Borexino Collaboration, Agostini M, Altenmüller K, et al. 2018. *Nature* 562(7728):505–510
- Botnen A, Carlsson M. 1999. In *Numerical Astrophysics*, vol. 240 of *Astrophys. Space Sci. Libr*
- Bray I, Stelbovics AT. 1992. *Phys. Rev. A* 46(11):6995–7011
- Brewer JM, Fischer DA. 2016. *ApJ* 831(1):20
- Buder S, Sharma S, Kos J, et al. 2021. *MNRAS* 506(1):150–201
- Buldgen G, Eggenberger P, Noels A, et al. 2023a. *A&A* 669:L9
- Buldgen G, Noels A, Baturin VA, et al. 2023b. *arXiv e-prints* :arXiv:2308.13368
- Burheim M, Hartman H, Nilsson H. 2023. *A&A* 672:A197
- Burke PG. 2011. *R-Matrix Theory of Atomic Collisions*. vol. 61
- Burnett DS, Jurewicz AJG, Woolum DS. 2019. *Meteorit. Planet. Sci.* 54(5):1092–1114
- Caffau E, Bonifacio P, François P, et al. 2011a. *Nature* 477(7362):67–69
- Caffau E, Bonifacio P, François P, et al. 2011b. *A&A* 534:A4
- Caffau E, Bonifacio P, François P, et al. 2012. *A&A* 542:A51
- Caffau E, Gallagher AJ, Bonifacio P, et al. 2018. *A&A* 614:A68
- Caffau E, Ludwig HG, Bonifacio P, et al. 2010a. *A&A* 514:A92
- Caffau E, Ludwig HG, Steffen M, Freytag B, Bonifacio P. 2011c. *Sol. Phys.* 268(2):255–269
- Caffau E, Ludwig HG, Steffen M, et al. 2008. *A&A* 488(3):1031–1046
- Caffau E, Ludwig HG, Steffen M, et al. 2015. *A&A* 579:A88
- Caffau E, Maiorca E, Bonifacio P, et al. 2009. *A&A* 498(3):877–884
- Caffau E, Monaco L, Spite M, et al. 2014. *A&A* 568:A29
- Caffau E, Sbordone L, Ludwig HG, Bonifacio P, Spite M. 2010b. *Astronomische Nachrichten* 331(7):725
- Canocchi G, Lind K, Lagae C, et al. 2023. *arXiv e-prints* :arXiv:2312.05078
- Carlos M, Meléndez J, Spina L, et al. 2019. *MNRAS* 485(3):4052–4059
- Carlsson M, Rutten RJ, Bruls JHMJ, Shchukina NG. 1994. *A&A* 288:860–882
- Casasayas-Barris N, Pallé E, Yan F, et al. 2020. *A&A* 635:A206
- Cayrel R, Depagne E, Spite M, et al. 2004. *A&A* 416:1117–1138
- Cayrel R, Steffen M, Chand H, et al. 2007. *A&A* 473(3):L37–L40
- Chappell BA, Pereira TMD. 2022. *A&A* 658:A182
- Chiappini C, Hirschi R, Meynet G, et al. 2006. *A&A* 449(2):L27–L30
- Chiavassa A, Casagrande L, Collet R, et al. 2018. *A&A* 611:A11
- Chiavassa A, Plez B, Josselin E, Freytag B. 2009. *A&A* 506(3):1351–1365
- Christensen-Dalsgaard J. 2021. *Living Reviews in Solar Physics* 18(1):2
- Clear CP, Uylings P, Raassen T, Nave G, Pickering JC. 2023. *MNRAS* 519(3):4040–4046
- Collet R, Asplund M, Nissen PE. 2009. *PASA* 26(3):330–334
- Collet R, Asplund M, Trampedach R. 2006. *ApJ* 644(2):L121–L124
- Collet R, Asplund M, Trampedach R. 2007. *A&A* 469(2):687–706
- Collet R, Hayek W, Asplund M, et al. 2011. *A&A* 528:A32
- Collet R, Nordlund Å, Asplund M, Hayek W, Trampedach R. 2018. *MNRAS* 475(3):3369–3392
- Cowan JJ, Sneden C, Roederer IU, et al. 2020. *ApJ* 890(2):119

Croft H, Dickinson AS, Gadéa FX. 1999. *J. Phys. B: At. Mol. Phys.* 32(1):81–94  
 Cubas Armas M, Asensio Ramos A, Socas-Navarro H. 2020. *A&A* 643:A142  
 Cubas Armas M, Fabbian D. 2021. *ApJ* 923(2):207  
 Cunto W, Mendoza C, Ochsenbein F, Zeppen CJ. 1993. *A&A* 275:L5–L8  
 Da Costa GS, Norris JE, Yong D. 2013. *ApJ* 769(1):8  
 Dalal S, Haywood RD, Mortier A, Chaplin WJ, Meunier N. 2023. *MNRAS* 525(3):3344–3353  
 de Jong RS, Agertz O, Berbel AA, et al. 2019. *The Messenger* 175:3–11  
 de Vicente A, del Pino Alemán T, Trujillo Bueno J. 2021. *ApJ* 912(1):63  
 Delgado Mena E, Bertrán de Lis S, Adibekyan VZ, et al. 2015. *A&A* 576:A69  
 Den Hartog EA, Lawler JE, Sneden C, Roederer IU, Cowan JJ. 2023. *ApJS* 265(2):42  
 Dere KP, Del Zanna G, Young PR, Landi E. 2023. *ApJS* 268(2):52  
 Deshmukh SA, Ludwig HG. 2023. *A&A* 675:A146  
 Deshmukh SA, Ludwig HG, Kučinskas A, et al. 2022. *A&A* 668:A48  
 Dickinson AS, Poteau R, Gadéa FX. 1999. *J. Phys. B: At. Mol. Phys.* 32(23):5451–5461  
 Dipti, Das T, Bartschat K, et al. 2019. *Atomic Data and Nuclear Data Tables* 127:1–21  
 Dobrovolskas V, Kučinskas A, Andrievsky SM, et al. 2012. *A&A* 540:A128  
 Dobrovolskas V, Kučinskas A, Bonifacio P, et al. 2014. *A&A* 565:A121  
 Dobrovolskas V, Kučinskas A, Bonifacio P, et al. 2015. *A&A* 576:A128  
 Dobrovolskas V, Kučinskas A, Steffen M, et al. 2013. *A&A* 559:A102  
 Dotter A. 2016. *ApJS* 222(1):8  
 Dravins D. 1982. *ARA&A* 20:61–89  
 Dravins D, Lindegren L, Nordlund A. 1981. *A&A* 96(1-2):345–364  
 Dravins D, Ludwig HG, Dahlén E, Pazira H. 2017. *A&A* 605:A90  
 Dravins D, Ludwig HG, Freytag B. 2021. *A&A* 649:A16  
 Dravins D, Nordlund A. 1990. *A&A* 228:203–217  
 Eggenberger P, Buldgen G, Salmon SJAJ, et al. 2022. *Nature Astronomy* 6:788–795  
 Eitner P, Bergemann M, Hansen CJ, et al. 2020. *A&A* 635:A38  
 Eitner P, Bergemann M, Ruiter AJ, et al. 2023. *A&A* 677:A151  
 Eklund G, Grumer J, Barklem PS, et al. 2021. *Phys. Rev. A* 103(3):032814  
 Eklund G, Grumer J, Rosén S, et al. 2020. *Phys. Rev. A* 102(1):012823  
 Ellwarth M, Schäfer S, Reiners A, Zechmeister M. 2023. *A&A* 673:A19  
 Ezzeddine R, Merle T, Plez B, et al. 2018. *A&A* 618:A141  
 Fabbian D, Khomenko E, Moreno-Insertis F, Nordlund Å. 2010. *ApJ* 724(2):1536–1541  
 Fabbian D, Moreno-Insertis F. 2015. *ApJ* 802(2):96  
 Fabbian D, Moreno-Insertis F, Khomenko E, Nordlund Å. 2012. *A&A* 548:A35  
 Fabbian D, Nissen PE, Asplund M, Pettini M, Akerman C. 2009. *A&A* 500(3):1143–1155  
 Fabiani Bendicho P, Trujillo Bueno J, Auer L. 1997. *A&A* 324:161–176  
 Feautrier P. 1964. *Comptes Rendus Academie des Sciences (serie non specifique)* 258:3189  
 Frebel A, Casey AR, Jacobson HR, Yu Q. 2013. *ApJ* 769(1):57  
 Frebel A, Christlieb N, Norris JE, Aoki W, Asplund M. 2006. *ApJ* 638(1):L17–L20  
 Frebel A, Collet R, Eriksson K, Christlieb N, Aoki W. 2008. *ApJ* 684(1):588–602  
 Freytag B, Steffen M, Ludwig HG, et al. 2012. *Journal of Computational Physics* 231(3):919–959  
 Froese Fischer C, Gaigalas G, Jönsson P, Bierón J. 2019. *Comput. Phys. Commun.* 237:184–187  
 Gallagher AJ, Bergemann M, Collet R, et al. 2020. *A&A* 634:A55  
 Gallagher AJ, Caffau E, Bonifacio P, et al. 2016. *A&A* 593:A48  
 Gallagher AJ, Caffau E, Bonifacio P, et al. 2017a. *A&A* 598:L10  
 Gallagher AJ, Ludwig HG, Ryan SG, Aoki W. 2015. *A&A* 579:A94  
 Gallagher AJ, Steffen M, Caffau E, et al. 2017b. *Mem. Soc. Astron. Italiana* 88:82  
 Galsgaard K, Nordlund Å. 1996. *J. Geophys. Res.* 101(A6):13445–13460  
 Gao X, Lind K, Amarsi AM, et al. 2020. *MNRAS* 497(1):L30–L34  
 Gehren T, Butler K, Mashonkina L, Reetz J, Shi J. 2001. *A&A* 366:981–1002

Geng Y, Liu Y, Zheng H, et al. 2022. *ApJS* 259(2):44

Gent MR, Bergemann M, Serenelli A, et al. 2022. *A&A* 658:A147

Giribaldi RE, da Silva AR, Smiljanic R, Cornejo Espinoza D. 2021. *A&A* 650:A194

Giribaldi RE, Ubaldo-Melo ML, Porto de Mello GF, et al. 2019. *A&A* 624:A10

Giribaldi RE, Van Eck S, Merle T, et al. 2023. *A&A* 679:A110

González Hernández JI, Bonifacio P, Caffau E, et al. 2009. *A&A* 505(2):L13–L16

González Hernández JI, Bonifacio P, Caffau E, et al. 2019. *A&A* 628:A111

González Hernández JI, Bonifacio P, Ludwig HG, et al. 2008. *A&A* 480(1):233–246

González Hernández JI, Bonifacio P, Ludwig HG, et al. 2010. *A&A* 519:A46

Gough DO. 1977. *ApJ* 214:196–213

Grevesse N, Asplund M, Sauval AJ. 2007. *Space Sci. Rev.* 130(1-4):105–114

Grevesse N, Sauval AJ. 1998. *Space Sci. Rev.* 85:161–174

Grumer J, Eklund G, Amarsi AM, et al. 2022. *Phys. Rev. Lett.* 128(3):033401

Grumer J, Eklund G, Amarsi AM, et al. 2023. *Phys. Rev. Lett.* 130(2):029901

Guitou M, Spielfiedel A, Feautrier N. 2010. *Chemical Physics Letters* 488(4):145–152

Gustafsson B, Edvardsson B, Eriksson K, et al. 2008. *A&A* 486(3):951–970

Hanke M, Hansen CJ, Ludwig HG, et al. 2020. *A&A* 635:A104

Hansen CJ, Koch A, Mashonkina L, et al. 2020. *A&A* 643:A49

Harutyunyan G, Steffen M, Mott A, et al. 2018. *A&A* 618:A16

Hawkins K, Masseron T, Jofré P, et al. 2016. *A&A* 594:A43

Hayek W, Asplund M, Carlsson M, et al. 2010. *A&A* 517:A49

Hayek W, Asplund M, Collet R, Nordlund Å. 2011. *A&A* 529:A158

Heber VS, Wieler R, Baur H, et al. 2009. *Geochim. Cosmochim. Acta* 73(24):7414–7432

Henry L, Vardya MS, Bodenheimer P. 1965. *ApJ* 142:841

Hinkle KH, Lambert DL. 1975. *MNRAS* 170:447–474

Hirose S, Hauschildt P, Minoshima T, Tomida K, Sano T. 2022. *A&A* 659:A87

Holweger H, Mueller EA. 1974. *Sol. Phys.* 39(1):19–30

Hubeny I, Lanz T. 2017. *arXiv e-prints* :arXiv:1706.01859

Hubeny I, Mihalas D. 2015. *Theory of Stellar Atmospheres*.

Hummer DG, Mihalas D. 1988. *ApJ* 331:794

Ibgui L, Hubeny I, Lanz T, Stehlé C. 2013. *A&A* 549:A126

Irwin AW. 2012. Astrophysics Source Code Library, record ascl:1211.002

Janson M, Squicciarini V, Delorme P, et al. 2021. *A&A* 646:A164

Jaume Bestard J, Štěpán J, Trujillo Bueno J. 2021. *A&A* 645:A101

Jofré P, Heiter U, Soubiran C. 2019. *ARA&A* 57:571–616

Johansson S, Litzén U, Lundberg H, Zhang Z. 2003. *ApJ* 584(2):L107–L110

Johnson JL, Li H. 2012. *ApJ* 751(2):81

Jönsson H, Ryde N, Nissen PE, et al. 2011. *A&A* 530:A144

Karovicova I, White TR, Nordlander T, et al. 2018. *MNRAS* 475(1):L81–L85

Karovicova I, White TR, Nordlander T, et al. 2020. *A&A* 640:A25

Kaulakys B. 1991. *J. Phys. B: At. Mol. Phys.* 24(5):L127–L132

Keller SC, Bessell MS, Frebel A, et al. 2014. *Nature* 506(7489):463–466

Kiselman D. 1991. *A&A* 245(1):L9–L12

Kiselman D, Nordlund A. 1995. *A&A* 302:578

Klevas J, Kučinskas A, Steffen M, Caffau E, Ludwig HG. 2016. *A&A* 586:A156

Kobayashi C, Karakas AI, Lugaro M. 2020. *ApJ* 900(2):179

Koesterke L, Allende Prieto C, Lambert DL. 2008. *ApJ* 680(1):764–773

Korn AJ, Grundahl F, Richard O, et al. 2007. *ApJ* 671(1):402–419

Korn AJ, Shi J, Gehren T. 2003. *A&A* 407:691–703

Kowkabany J, Ezzeddine R, Charbonnel C, et al. 2022. *arXiv e-prints* :arXiv:2209.02184

Kramida AE. 2010. *Atomic Data and Nuclear Data Tables* 96(6):586–644

- Krief M, Feigel A, Gazit D. 2016. *ApJ* 821(1):45
- Kunitomo M, Guillot T, Buldgen G. 2022. *A&A* 667:L2
- Kupka F. 2009. *Mem. Soc. Astron. Italiana* 80:701
- Kupka F, Muthsam HJ. 2017. *Living Reviews in Computational Astrophysics* 3(1):1
- Kurucz RL. 2017. *Canadian Journal of Physics* 95(9):825–827
- Kučinskas A, Dobrovolskas V, Bonifacio P. 2014. *A&A* 568:L4
- Kučinskas A, Klevas J, Ludwig HG, et al. 2018. *A&A* 613:A24
- Kučinskas A, Steffen M, Ludwig HG, et al. 2013. *A&A* 549:A14
- Lagae C, Amarsi AM, Rodríguez Díaz LF, et al. 2023. *A&A* 672:A90
- Lambert DL. 1978. *MNRAS* 182:249–272
- Lambert DL. 1993. *Physica Scripta Volume T* 47:186–198
- Lambert J, Paletou F, Josselin E, Glorian JM. 2016. *European Journal of Physics* 37(1):015603
- Landi E, Testa P. 2015. *ApJ* 800(2):110
- Lanz T, Hubeny I. 2003. *ApJS* 146(2):417–441
- Launoy T, Loreau J, Dochain A, et al. 2019. *ApJ* 883(1):85
- Leenaarts J, Carlsson M. 2009. In *The Second Hinode Science Meeting: Beyond Discovery-Toward Understanding*, vol. 415 of *ASP Conf. Ser.*
- Leenaarts J, Carlsson M, Rouppe van der Voort L. 2012. *ApJ* 749(2):136
- Leenaarts J, Pereira TMD, Carlsson M, Uitenbroek H, De Pontieu B. 2013. *ApJ* 772(2):89
- Li HN, Ludwig HG, Caffau E, Christlieb N, Zhao G. 2013. *ApJ* 765(1):51
- Li MC, Li W, Jönsson P, Amarsi AM, Grumer J. 2023a. *ApJS* 265(1):26
- Li W, Amarsi AM, Papoulia A, Ekman J, Jönsson P. 2021. *MNRAS* 502(3):3780–3799
- Li W, Jönsson P, Amarsi AM, Li MC, Grumer J. 2023b. *A&A* 674:A54
- Li Y, Ezzeddine R. 2023. *AJ* 165(4):145
- Lind K, Amarsi AM, Asplund M, et al. 2017. *MNRAS* 468(4):4311–4322
- Lind K, Asplund M, Barklem PS. 2009. *A&A* 503(2):541–544
- Lind K, Bergemann M, Asplund M. 2012. *MNRAS* 427(1):50–60
- Lind K, Melendez J, Asplund M, Collet R, Magic Z. 2013. *A&A* 554:A96
- Lind K, Nordlander T, Wehrhahn A, et al. 2022. *A&A* 665:A33
- Liu F, Yong D, Asplund M, Ramírez I, Meléndez J. 2016. *MNRAS* 457(4):3934–3948
- Lodders K. 2021. *Space Sci. Rev.* 217(3):44
- Löhner-Böttcher J, Schmidt W, Schlichenmaier R, Steinmetz T, Holzwarth R. 2019. *A&A* 624:A57
- Ludwig HG. 2007. *A&A* 471(3):925–927
- Ludwig HG, Allard F, Hauschildt PH. 2002. *A&A* 395:99–115
- Ludwig HG, Behara NT, Steffen M, Bonifacio P. 2009a. *A&A* 502(2):L1–L4
- Ludwig HG, Caffau E, Steffen M, et al. 2009b. *Mem. Soc. Astron. Italiana* 80:711
- Ludwig HG, Kučinskas A. 2012. *A&A* 547:A118
- Magg E, Bergemann M, Serenelli A, et al. 2022. *A&A* 661:A140
- Magic Z, Collet R, Asplund M, et al. 2013a. *A&A* 557:A26
- Magic Z, Collet R, Hayek W, Asplund M. 2013b. *A&A* 560:A8
- Mallinson JWE, Lind K, Amarsi AM, et al. 2022. *A&A* 668:A103
- Martin W, Wiese W. 2006. *Atomic Spectroscopy*. In *Springer Handbook of Atomic*. 175
- Mashonkina L. 2020. *MNRAS* 493(4):6095–6108
- Mashonkina L, Gehren T, Shi JR, Korn AJ, Grupp F. 2011. *A&A* 528:A87
- Mashonkina L, Jablonka P, Sitnova T, Pakhomov Y, North P. 2017. *A&A* 608:A89
- Mashonkina L, Pakhomov Y, Sitnova T, et al. 2023. *MNRAS* 524(3):3526–3536
- Mashonkina L, Ryabtsev A, Frebel A. 2012. *A&A* 540:A98
- Mashonkina L, Sitnova T, Korotin S. 2022. *Astronomy Letters* 48(5):303–310
- Mashonkina LI, Belyaev AK. 2019. *Astronomy Letters* 45(6):341–352
- Masseron T, Osorio Y, García-Hernández DA, et al. 2021. *A&A* 647:A24
- Massey HSW. 1949. *Reports on Progress in Physics* 12(1):248–269

Matsuno T, Amarsi AM, Carlos M, Nissen PE. 2024. *A&A* (in prep.)

Maxted PFL. 2018. *A&A* 616:A39

Meléndez J, Bedell M, Bean JL, et al. 2017. *A&A* 597:A34

Meléndez J, Casagrande L, Ramírez I, Asplund M, Schuster WJ. 2010. *A&A* 515:L3

Mihalas D, Dappen W, Hummer DG. 1988. *ApJ* 331:815

Mishenina TV, Kučinskas A, Andrievsky SM, et al. 2009. *Baltic Astronomy* 18:193–203

Monaco L, Boffin HMJ, Bonifacio P, et al. 2014. *A&A* 564:L6

Moore CS, Uitenbroek H, Rempel M, Criscuoli S, Rast MP. 2015. *ApJ* 799(2):150

Mott A, Steffen M, Caffau E, Spada F, Strassmeier KG. 2017. *A&A* 604:A44

Mott A, Steffen M, Caffau E, Strassmeier KG. 2020. *A&A* 638:A58

Mucciarelli A, Bellazzini M, Ibata R, et al. 2012. *MNRAS* 426(4):2889–2900

Muthsam HJ, Kupka F, Löw-Baselli B, et al. 2010. *New A* 15(5):460–475

Nahar S. 2020. *Atoms* 8(4):68

Nahar SN, Pradhan AK. 2005. *A&A* 437(1):345–354

Nave G, Johansson S, Learner RCM, Thorne AP, Brault JW. 1994. *ApJS* 94:221

Nissen PE. 2015. *A&A* 579:A52

Nissen PE, Amarsi AM, Skúladóttir Á, Schuster WJ. 2023. *arXiv e-prints* :arXiv:2312.07768

Nissen PE, Asplund M, Hill V, D’Odorico S. 2000. *A&A* 357:L49–L52

Nissen PE, Chen YQ, Asplund M, Pettini M. 2004. *A&A* 415:993–1007

Nissen PE, Gustafsson B. 2018. *A&A Rev.* 26(1):6

Nissen PE, Primas F, Asplund M, Lambert DL. 2002. *A&A* 390:235–251

Nomoto K, Kobayashi C, Tominaga N. 2013. *ARA&A* 51(1):457–509

Nordlander T, Amarsi AM, Lind K, et al. 2017. *A&A* 597:A6

Nordlund A. 1982. *A&A* 107:1–10

Nordlund Å. 2019. In *Radiative Signatures from the Cosmos*, vol. 519 of *ASP Conf. Ser.*

Nordlund A, Dravins D. 1990. *A&A* 228:155–183

Nordlund Å, Galsgaard K. 1995. Tech. rep., Niels Bohr Institute, University of Copenhagen

Nordlund Å, Ramsey JP, Popovas A, Küffmeier M. 2018. *MNRAS* 477(1):624–638

Nordlund A, Spruit HC, Ludwig HG, Trampedach R. 1997. *A&A* 328:229–234

Nordlund Å, Stein RF. 1990. *Comput. Phys. Commun.* 59(1):119–125

Nordlund Å, Stein RF, Asplund M. 2009. *Living Reviews in Solar Physics* 6(1):2

Norris JE, Christlieb N, Bessell MS, et al. 2012. *ApJ* 753(2):150

Norris JE, Yong D. 2019. *ApJ* 879(1):37

Norris JE, Yong D, Frebel A, Ryan SG. 2023. *MNRAS* 522(1):1358–1376

Olson GL, Auer LH, Buchler JR. 1986. *J. Quant. Spectr. Rad. Transf.* 35:431–442

Osorio Y, Aguado DS, Allende Prieto C, Hubeny I, González Hernández JJ. 2022. *ApJ* 928(2):173

Osorio Y, Allende Prieto C, Hubeny I, Mészáros S, Shetrone M. 2020. *A&A* 637:A80

Osorio Y, Barklem PS. 2016. *A&A* 586:A120

Osorio Y, Barklem PS, Lind K, et al. 2015. *A&A* 579:A53

Ou X, Roederer IU, Sneden C, et al. 2020. *ApJ* 900(2):106

Palacios A, Gebran M, Josselin E, et al. 2010. *A&A* 516:A13

Paletou F, Anterrieu E. 2009. *A&A* 507(3):1815–1818

Pereira TMD, Asplund M, Collet R, et al. 2013. *A&A* 554:A118

Pereira TMD, Asplund M, Kiselman D. 2009a. *A&A* 508(3):1403–1416

Pereira TMD, Kiselman D, Asplund M. 2009b. *A&A* 507(1):417–432

Pereira TMD, Uitenbroek H. 2015. *A&A* 574:A3

Pietrow AGM, Hoppe R, Bergemann M, Calvo F. 2023. *A&A* 672:L6

Piskunov N, Valenti JA. 2017. *A&A* 597:A16

Placco VM, Beers TC, Reggiani H, Meléndez J. 2016. *ApJ* 829(2):L24

Popa SA, Hoppe R, Bergemann M, et al. 2023. *A&A* 670:A25

Pradhan A. 2023. *Atoms* 11(3):52

Prakapavičius D, Kučinskas A, Dobrovolskas V, et al. 2017. *A&A* 599:A128

Prantzos N, Abia C, Limongi M, Chieffi A, Cristallo S. 2018. *MNRAS* 476(3):3432–3459

Primas F, Asplund M, Nissen PE, Hill V. 2000. *A&A* 364:L42–L46

Ralchenko Y, Kramida A. 2020. *Atoms* 8(3):56

Ramírez I, Allende Prieto C, Koesterke L, Lambert DL, Asplund M. 2009. *A&A* 501(3):1087–1101

Randich S, Magrini L. 2021. *Frontiers in Astronomy and Space Sciences* 8:6

Reddy ABS. 2020. *MNRAS* 495(1):383–401

Reggiani H, Amarsi AM, Lind K, et al. 2019. *A&A* 627:A177

Reggiani H, Meléndez J, Kobayashi C, Karakas A, Placco V. 2017. *A&A* 608:A46

Reiners A, Yan F, Ellwarth M, Ludwig HG, Nortmann L. 2023. *A&A* 673:A71

Rempel M. 2014. *ApJ* 789(2):132

Rodríguez Díaz LF, Bigot L, Aguirre Børsen-Koch V, et al. 2022. *MNRAS* 514(2):1741–1756

Rodríguez Díaz LF, Lagae C, Amarsi AM, et al. 2023. *A&A* (submitted)

Romano D, Karakas AI, Tosi M, Matteucci F. 2010. *A&A* 522:A32

Ruchti GR, Bergemann M, Serenelli A, Casagrande L, Lind K. 2013. *MNRAS* 429(1):126–134

Rutten RJ. 2003. *Radiative Transfer in Stellar Atmospheres*. Lecture Notes Utrecht University

Ryabchikova T, Piskunov N, Kurucz RL, et al. 2015. *Phys. Scr* 90(5):054005

Rybicki GB, Hummer DG. 1992. *A&A* 262:209–215

Sauval AJ, Grevesse N, Zander R, Brault JW, Stokes GM. 1984. *ApJ* 282:330–338

Sbordone L, Bonifacio P, Caffau E, et al. 2010. *A&A* 522:A26

Sbordone L, Limongi M, Chieffi A, et al. 2009. *A&A* 503(1):121–127

Schmidt HT, Thomas RD, Gatchell M, et al. 2013. *Rev. Sci. Instrum.* 84(5):055115–055115–6

Schweitzer A, Hauschildt PH, Baron E. 2000. *ApJ* 541(2):1004–1015

Scott P, Asplund M, Grevesse N, Bergemann M, Sauval AJ. 2015a. *A&A* 573:A26

Scott P, Grevesse N, Asplund M, et al. 2015b. *A&A* 573:A25

Seaton MJ. 1962a. In *Atomic and Molecular Processes*, ed. DR Bates

Seaton MJ. 1962b. *Proceedings of the Physical Society* 79(6):1105–1117

Serenelli AM, Bergemann M, Ruchti G, Casagrande L. 2013. *MNRAS* 429(4):3645–3657

Shchukina N, Sukhorukov A, Trujillo Bueno J. 2016. *A&A* 586:A145

Shchukina N, Trujillo Bueno J. 2001. *ApJ* 550(2):970–990

Shchukina N, Trujillo Bueno J. 2015. *A&A* 579:A112

Shchukina NG, Trujillo Bueno J, Asplund M. 2005. *ApJ* 618(2):939–952

Siqueira Mello C, Hill V, Barbuy B, et al. 2014. *A&A* 565:A93

Siqueira Mello C, Spite M, Barbuy B, et al. 2013. *A&A* 550:A122

Sitnova T, Zhao G, Mashonkina L, et al. 2015. *ApJ* 808(2):148

Sitnova TM, Mashonkina LI, Ezzeddine R, Frebel A. 2019. *MNRAS* 485(3):3527–3543

Sitnova TM, Yakovleva SA, Belyaev AK, Mashonkina LI. 2022. *MNRAS* 515(1):1510–1523

Skartlien R. 2000. *ApJ* 536(1):465–480

Smyth RT, Ballance CP, Ramsbottom CA. 2019. *ApJ* 874(2):144

Snedden C, Boesgaard AM, Cowan JJ, et al. 2023. *ApJ* 953(1):31

Socas-Navarro H. 2015. *A&A* 577:A25

Socas-Navarro H, de la Cruz Rodríguez J, Asensio Ramos A, Trujillo Bueno J, Ruiz Cobo B. 2015. *A&A* 577:A7

Socas-Navarro H, Trujillo Bueno J. 1997. *ApJ* 490(1):383–392

Sonoi T, Ludwig HG, Dupret MA, et al. 2019. *A&A* 621:A84

Spite M, Andrievsky SM, Spite F, et al. 2012. *A&A* 541:A143

Spite M, Caffau E, Andrievsky SM, et al. 2011. *A&A* 528:A9

Spite M, Caffau E, Bonifacio P, et al. 2013. *A&A* 552:A107

Spite M, Cayrel R, Plez B, et al. 2005. *A&A* 430:655–668

Spite M, Peterson RC, Gallagher AJ, Barbuy B, Spite F. 2017. *A&A* 600:A26

Steenbock W, Holweger H. 1984. *A&A* 130(2):319–323

- Steffen M. 2017. *Mem. Soc. Astron. Italiana* 88:22
- Steffen M, Caffau E, Ludwig HG. 2013. *Mem. S.A.It. Suppl.* 24:37
- Steffen M, Gallagher AJ, Caffau E, Bonifacio P, Ludwig HG. 2017. *Proc. Int. Astron. Union.* 13(S334):364–365
- Steffen M, Prakašavičius D, Caffau E, et al. 2015. *A&A* 583:A57
- Stein RF, Nordlund Å. 1998. *ApJ* 499(2):914–933
- Stein RF, Nordlund Å. 2003. In *Stellar Atmosphere Modeling*, vol. 288 of *ASP Conf. Ser.*
- Stein RF, Nordlund Å, Collet R, Trampedach R. 2024. *MNRAS* (in prep.)
- Suárez-Andrés L, Israelian G, González Hernández JI, et al. 2018. *A&A* 614:A84
- Summers HP, O’Mullane MG. 2011. In *ICAMDATA-2010*, vol. 1344 of *AIP Conf. Proc.*
- Takeda Y. 2022. *Sol. Phys.* 297(1):4
- Takeda Y, Hashimoto O, Taguchi H, et al. 2005. *PASJ* 57:751–768
- Tanner JD, Basu S, Demarque P. 2013a. *ApJ* 778(2):117
- Tanner JD, Basu S, Demarque P. 2013b. *ApJ* 767(1):78
- Tayal SS, Zatsarinny O. 2022. *ApJS* 259(2):52
- Thompson RI. 1973. *ApJ* 181:1039–1054
- Thygesen AO, Kirby EN, Gallagher AJ, et al. 2017. *ApJ* 843(2):144
- Thygesen AO, Sbordone L, Ludwig HG, et al. 2016. *A&A* 588:A66
- Ting YS, Conroy C, Rix HW. 2016. *ApJ* 826(1):83
- Trampedach R, Asplund M, Collet R, Nordlund Å, Stein RF. 2013. *ApJ* 769(1):18
- Trampedach R, Stein RF, Christensen-Dalsgaard J, Nordlund Å, Asplund M. 2014. *MNRAS* 445(4):4366–4384
- Trujillo Bueno J, Fabiani Bendicho P. 1995. *ApJ* 455:646
- Uitenbroek H. 2000. *ApJ* 536(1):481–493
- Uitenbroek H, Bruls JHMJ. 1992. *A&A* 265(1):268–277
- Uitenbroek H, Criscuoli S. 2011. *ApJ* 736(1):69
- Umeda H, Nomoto K. 2002. *ApJ* 565(1):385–404
- van Eck MP, Fursa DV, Bray I, Zatsarinny O, Bartschat K. 2020. *J. Phys. B: At. Mol. Phys.* 53(1):015204
- van Regemorter H. 1962. *ApJ* 136:906
- Černiauskas A, Kučinskas A, Klevas J, et al. 2017. *A&A* 604:A35
- Černiauskas A, Kučinskas A, Klevas J, et al. 2018. *A&A* 615:A173
- Villante FL, Serenelli AM, Delahaye F, Pinsonneault MH. 2014. *ApJ* 787(1):13
- Vitas N, Khomenko E. 2015. *Annales Geophysicae* 33(6):703–709
- Vögler A, Shelyag S, Schüssler M, et al. 2005. *A&A* 429:335–351
- Voronov YV, Yakovleva SA, Belyaev AK. 2022. *ApJ* 926(2):173
- Štěpán J, Jaime Bestard J, Trujillo Bueno J. 2020. *A&A* 636:A24
- Štěpán J, Trujillo Bueno J. 2013. *A&A* 557:A143
- Wang EM, Nordlander T, Collaboration G. 2024. *MNRAS* (in prep.)
- Wang EX, Nordlander T, Asplund M, et al. 2021. *MNRAS* 500(2):2159–2176
- Wang EX, Nordlander T, Asplund M, et al. 2022. *MNRAS* 509(1):1521–1535
- Wedemeyer S, Freytag B, Steffen M, Ludwig HG, Holweger H. 2004. *A&A* 414:1121–1137
- Wedemeyer S, Kučinskas A, Klevas J, Ludwig HG. 2017. *A&A* 606:A26
- Wedemeyer-Böhm S, Rouppe van der Voort L. 2009. *A&A* 503(1):225–239
- Wende S, Reiners A, Ludwig HG. 2009. *A&A* 508(3):1429–1442
- Xu X, Shi J, Wang X. 2022. *ApJ* 936(1):4
- Yakovleva SA, Belyaev AK, Kraemer WP. 2019. *MNRAS* 483(4):5105–5109
- Yan F, Pallé E, Fosbury RAE, Petr-Gotzens MG, Henning T. 2017. *A&A* 603:A73
- Yan PG, Babb JF. 2023. *MNRAS* 522(1):1265–1269
- Yong D, Norris JE, Bessell MS, et al. 2013. *ApJ* 762(1):27
- Young PR. 2018. *ApJ* 855(1):15



Zatsarinny O, Bartschat K. 2013. *J. Phys. B: At. Mol. Phys.* 46(11):112001  
Zatsarinny O, Bartschat K, Fernandez-Menchero L, Tayal SS. 2019. *Phys. Rev. A* 99(2):023430  
Zhao G, Mashonkina L, Yan HL, et al. 2016. *ApJ* 833(2):225  
Zhou C, Shang X. 2023. *J. Quant. Spectr. Rad. Transf.* 298:108484  
Zhou Y, Amarsi AM, Aguirre Børsen-Koch V, et al. 2023. *A&A* 677:A98

**Table 1:** Refereed 3D LTE and NLTE studies of metal abundances and/or hydrogen line profiles for stars other than the Sun.

Reference	Species LTE <sup>a</sup>	Species NLTE <sup>b</sup>	Stars/models <sup>c</sup>
Asplund et al. (1999), Nissen et al. (2000)	Li I		HD84937, HD140283
Primas et al. (2000)	Be II		G64-12
Asplund & García Pérez (2001)	OH		#8 D $-3 < [\text{Fe}/\text{H}] < 0$
Allende Prieto et al. (2002)	Fe I, Fe II		Procyon
Nissen et al. (2002)	O I, Fe II		#7 D/SG $-2.5 < [\text{Fe}/\text{H}] < 0$
Asplund et al. (2003), Barklem et al. (2003)		Li I	HD84937, HD140283
Akerman et al. (2004)	C I, O I		#8 D $-3 < [\text{Fe}/\text{H}] < 0$
Nissen et al. (2004)	Si I, Fe II, Zn I		#8 D $-3 < [\text{Fe}/\text{H}] < 0$
Shchukina et al. (2005)		O I, Fe I, Fe II	HD140283
Collet et al. (2006), Frebel et al. (2006)	15 neutral, 7 singly ionized, 5 molecules		HE 0107-5240, HE 1327-2326
Asplund et al. (2006)	Li I		#10 D/SG $-3 < [\text{Fe}/\text{H}] < 0$
Cayrel et al. (2007)		Li I	HD74000
Collet et al. (2007)	Li I, O I, Na I, Mg I, Ca I, Fe I, Fe II, CH, NH, OH		#8 G $-3 < [\text{Fe}/\text{H}] < 0$
Korn et al. (2007)	Mg I, Ti II, Fe I, Fe II		#2 D/G $[\text{Fe}/\text{H}] = -2$
González Hernández et al. (2008)	Li I, OH		CS 22876-032
Frebel et al. (2008)	12 neutral, 8 singly ionized, 3 molecules		HE 1327-2326
Mishenina et al. (2009)	Na I, Mg I, Ba II		#1 G $[\text{Fe}/\text{H}] = -1$
Bonifacio et al. (2009)	Si I, Sc II, Ti II, Cr I, Mn I, Fe I, Co I, Zn I, CH		#3 D/G $[\text{Fe}/\text{H}] = -3$
Ramírez et al. (2009)	Fe I, Fe II		#1 D $[\text{Fe}/\text{H}] = 0$
Sbordone et al. (2009)	Si I		#4 D/SG $-1 < [\text{Fe}/\text{H}] < 0$
Collet et al. (2009)	Ba II		HD140283
González Hernández et al. (2009)		HI, Li I	#11 D/SG $[\text{Fe}/\text{H}] = -2$
Ludwig et al. (2009a)	HI		#6 D/SG $-3 < [\text{Fe}/\text{H}] < 0$
Wende et al. (2009)	FeH		#8 D $[\text{Fe}/\text{H}] = 0$
Behara et al. (2010)	C I, O I, CH, NH, OH, C <sub>2</sub>		#4 D $-3 < [\text{Fe}/\text{H}] < -2$
González Hernández et al. (2010)	Fe I, OH		#52 D/SG $-3 < [\text{Fe}/\text{H}] < 0$
Sbordone et al. (2010)		Li I	#17 D/SG $-3 < [\text{Fe}/\text{H}] < -2$

**Table 1:** continued.

Reference	Species LTE <sup>a</sup>	Species NLTE <sup>b</sup>	Stars/models <sup>c</sup>
<a href="#">Bonifacio et al. (2010)</a>	Cu I		#6 D/G $-2 < [\text{Fe}/\text{H}] < -1$
<a href="#">Caffau et al. (2010b)</a> , <a href="#">Spite et al. (2011)</a>	SI		#6 D/SG $-3 < [\text{Fe}/\text{H}] < -1$
<a href="#">Hayek et al. (2011)</a>	Fe I, Fe II, CH, NH, OH		#4 G $-3 < [\text{Fe}/\text{H}] < 0$
<a href="#">Jönsson et al. (2011)</a>	SI		#7 G $-3 < [\text{Fe}/\text{H}] < -1$
<a href="#">Caffau et al. (2011b)</a>	Mg I, Ca I, Ca II, Fe I		#1 D $[\text{Fe}/\text{H}] = -3$
<a href="#">Caffau et al. (2011a, 2012)<sup>c</sup></a>	Mg I, Ca I, Ca II, Si I, Ti II, Fe I, Ni I, Sr II, CH, NH		SDSS J102915.14+172927.9
<a href="#">Dobrovolskas et al. (2012)</a>	Ba II		#4 G $-3 < [\text{Fe}/\text{H}] < 0$
<a href="#">Spite et al. (2012)</a>	Ca I		#3 D/G $[\text{Fe}/\text{H}] = -3$
<a href="#">Norris et al. (2012)</a>	CH, OH		#1 G $[\text{Fe}/\text{H}] = -3$
<a href="#">Bonifacio et al. (2012)</a>	SI		HE 1327-2326
<a href="#">Kučinskas et al. (2013)</a>	17 neutral, 8 singly ionized, 6 molecules		#1 G $[\text{Fe}/\text{H}] = 0$
<a href="#">Siqueira Mello et al. (2013)</a>	Pb I		#1 G $[\text{Fe}/\text{H}] = -3$
<a href="#">Li et al. (2013)</a>	O I, HF		#4 G $[\text{Fe}/\text{H}] = -2$
<a href="#">Spite et al. (2013)</a>	CN, CH		#1 D $[\text{Fe}/\text{H}] = -3$
<a href="#">Lind et al. (2013)</a>		Li I, Na I, Ca I, Ca II	#4 D/SG $-3.5 < [\text{Fe}/\text{H}] < -2$
<a href="#">Dobrovolskas et al. (2013)</a>	12 neutral, 8 singly ionized, 6 molecules		#4 G $-3 < [\text{Fe}/\text{H}] < 0$
<a href="#">Monaco et al. (2014)</a>		Li I	#4 G $-1 < [\text{Fe}/\text{H}] < 0$
<a href="#">Siqueira Mello et al. (2014)</a>	Mg I, Al I, Si I, Sc II, V I, V II, Mn I		#2 G $-3 < [\text{Fe}/\text{H}] < -2$
<a href="#">Dobrovolskas et al. (2014)</a> , <a href="#">Kučinskas et al. (2014)</a>	Na I, O I	Li I	#4 D $-1 < [\text{Fe}/\text{H}] < 0$
<a href="#">Caffau et al. (2014)</a>	SI		#2 D $-2 < [\text{Fe}/\text{H}] < -1$
<a href="#">Dobrovolskas et al. (2015)</a>	OH, O I		#4 G $-3.5 < [\text{Fe}/\text{H}] < -2.5$
<a href="#">Bessell et al. (2015)</a>	CH, NH, OH		SMSS0313-6708
<a href="#">Gallagher et al. (2015)</a>	Ba II, Fe I, Fe II		HD140283
<a href="#">Amarsi et al. (2015, 2016a)</a>		O I	#60 D/SG $-3 < [\text{Fe}/\text{H}] < 0$
<a href="#">Klevas et al. (2016)</a>		Li I	#16 D/SG/G $-2 < [\text{Fe}/\text{H}] < 0$
<a href="#">Gallagher et al. (2016)</a> , <a href="#">Caffau et al. (2018)</a> , <a href="#">Bonifacio et al. (2018b)</a>	CH		#18 D $-3 < [\text{Fe}/\text{H}] < -1$

**Table 1:** continued.

Reference	Species LTE <sup>a</sup>	Species NLTE <sup>b</sup>	Stars/models <sup>c</sup>
<a href="#">Amarsi et al. (2016b)</a>		Fe I, Fe II	#4 D/SG/G $-3.5 < [\text{Fe}/\text{H}] < -2$
<a href="#">Thygesen et al. (2016, 2017)</a>	MgH		#22 D/G $-3 < [\text{Fe}/\text{H}] < -0.5$
<a href="#">Nordlander et al. (2017)</a>		Li I, Na I, Mg I, Al I Ca II, Si I, Fe I	SMSS0313-6708
<a href="#">Gallagher et al. (2017a)</a>	CH, OH		#1 D $[\text{Fe}/\text{H}] = -3$
<a href="#">Prakapavičius et al. (2017)</a>	OH		HD122563
<a href="#">Spite et al. (2017)</a>	C I, CH, OH		HD84937
<a href="#">Černiauskas et al. (2017)</a>	Na I, Mg I, K I		#1 G $[\text{Fe}/\text{H}] = -1$
<a href="#">Mott et al. (2017)</a>		Li I	HD 123351
<a href="#">Bergemann et al. (2017a)</a>		Mg I	#2 D/G $-2 < [\text{Fe}/\text{H}] < -0.5$
<a href="#">Wedemeyer et al. (2017)</a>		HI, Ca II	Aldebaran
<a href="#">Collet et al. (2018)</a>	CH, NH, OH, CN		HD122563
<a href="#">Amarsi et al. (2018b)</a>		HI	#169 D/SG/G $-4 < [\text{Fe}/\text{H}] < 0.5$
<a href="#">Černiauskas et al. (2018)</a>	Mg I, K I		#4 D $-1 < [\text{Fe}/\text{H}] < 0$
<a href="#">Harutyunyan et al. (2018)</a>		Li I	#24 D $-1 < [\text{Fe}/\text{H}] < 0.5$
<a href="#">Giribaldi et al. (2019)</a>	HI		#8 D $-0.5 < [\text{Fe}/\text{H}] < 0$
<a href="#">Reggiani et al. (2019)</a>		K I	Procyon
<a href="#">González Hernández et al. (2019)</a>		Li I	CS 22876-032
<a href="#">Amarsi et al. (2019b,c)</a>		C I, O I	#74 D/SG $-4 < [\text{Fe}/\text{H}] < 0.5$
<a href="#">Amarsi et al. (2019b,c)</a>	Fe II		#164 D/SG/G $-4 < [\text{Fe}/\text{H}] < 0.5$
<a href="#">Bergemann et al. (2019)</a>		Mn I	#8 D/SG/G $-2.5 < [\text{Fe}/\text{H}] < 0$
<a href="#">Hanke et al. (2020)</a>	Ti I, Ti II		#1 G $[\text{Fe}/\text{H}] = -2$
<a href="#">Mott et al. (2020)</a>		Li I	#70 D/SG $-3 < [\text{Fe}/\text{H}] < 0$
<a href="#">Wang et al. (2021, 2022)</a>		Li I	#195 D/SG/G $-4 < [\text{Fe}/\text{H}] < 0.5$
<a href="#">Barklem et al. (2021)</a>		Li I, Na I	#4 D/G $-3 < [\text{Fe}/\text{H}] < 0$
<a href="#">Masseron et al. (2021)</a>	Mg I, Si I, Ca I, Fe I		#9 G $-3 < [\text{Fe}/\text{H}] < 0$
<a href="#">Amarsi et al. (2022)</a>		Fe I, Fe II	#32 D/SG $-4 < [\text{Fe}/\text{H}] < 0.5$
<a href="#">Lagae et al. (2023)</a>	CH, NH, Ti II, Ni I	Li I, Na I, Mg I, Al I, Ca I, Ca II, Si I, Fe I	SDSS J102915.14+172927.9
<a href="#">Deshmukh &amp; Ludwig (2023)<sup>d</sup></a>	CO, OH, CH, CN, C <sub>2</sub>		#5 D $-3 < [\text{Fe}/\text{H}] < 0$

<sup>a</sup> includes 3D LTE + 1D (NLTE-LTE); <sup>b</sup> includes LTE and NLTE; <sup>c</sup> D=dwarf, SG=subgiant, G=red giant, # is the number of 3D models; <sup>d</sup> Non-equilibrium chemistry